nature cancer

Article

https://doi.org/10.1038/s43018-023-00557-4

The proteasome regulator PSME4 modulates proteasome activity and antigen diversity to abrogate antitumor immunity in NSCLC

Received: 30 May 2022

Accepted: 10 April 2023

Published online: 22 May 2023

Check for updates

Aaron Javitt[1,16], Merav D. Shmueli[1,16] ✉, Matthias P. Kramer[1], Aleksandra A. Kolodziejczyk[1], Ivan J. Cohen[1], Lihi Radomir[1], Daoud Sheban[1], Iris Kamer[2], Kevin Litchfield[3], Elizabeta Bab-Dinitz[2], Oranit Zadok[2], Vanessa Neiens[4,5], Adi Ulman[1], Hila Wolf-Levy[1], Avital Eisenberg-Lerner[1], Assaf Kacen[1], Michal Alon[6], Ana Toste Rêgo[7], Elvira Stacher-Priehse[8], Michael Lindner[8], Ina Koch[5,8], Jair Bar[2,9], Charles Swanton[3], Yardena Samuels[5], Yishai Levin[10], Paula C. A. da Fonseca[6,15], Eran Elinav[1,11], Nir Friedman[1], Silke Meiners[4,5,12,13,14] & Yifat Merbl[1] ✉

Immunotherapy revolutionized treatment options in cancer, yet the mechanisms underlying resistance in many patients remain poorly understood. Cellular proteasomes have been implicated in modulating antitumor immunity by regulating antigen processing, antigen presentation, inflammatory signaling and immune cell activation. However, whether and how proteasome complex heterogeneity may affect tumor progression and the response to immunotherapy has not been systematically examined. Here, we show that proteasome complex composition varies substantially across cancers and impacts tumor–immune interactions and the tumor microenvironment. Through profiling of the degradation landscape of patient-derived non-small-cell lung carcinoma samples, we find that the proteasome regulator PSME4 is upregulated in tumors, alters proteasome activity, attenuates presented antigenic diversity and associates with lack of response to immunotherapy. Collectively, our approach affords a paradigm by which proteasome composition heterogeneity and function should be examined across cancer types and targeted in the context of precision oncology.

Immune checkpoint inhibition (ICI) has revolutionized treatment options for patients with cancer, yet response rates vary between 10% and 50% in most types of solid tumors[1]. Additionally, many of the factors driving resistance to ICI have not yet been identified. Among other causes, the ubiquitin–proteasome system has been suggested to contribute to numerous aspects of antitumor immunity, such as activation of inflammation, antigen processing and presentation, and T cell differentiation[2,3]. Most of these are attributed to changes in the catalytic activity of the constitutive proteasome and immunoproteasome, which are induced by inflammatory signals[4–7]. Indeed, the immunoproteasome is suggested to enhance antigen presentation through altered peptide cleavage, which is responsible for generating more hydrophobic peptides that are thought to be preferential for binding the transporter associated with antigen processing (TAP) and for MHC class I presentation[2,8,9]. Further, immunoproteasome upregulation has been recently associated with response

A full list of affiliations appears at the end of the paper. ✉e-mail: merav.shmueli@weizmann.ac.il; Yifat.merbl@weizmann.ac.il

to ICI[10–12]. Yet, systematic examination of whether and how proteasome degradation in general, and proteasome complex heterogeneity in particular, are involved in resistance to therapy remains poorly understood.

Beyond the canonical classification of immunoproteasome and constitutive proteasome based on their catalytic cores, which catalyze protein cleavage into peptides, different regulatory subunits shape proteasomal functions. The 19S regulatory complex has been shown to be pivotal for binding of ubiquitinated species and substrate unfolding, while the other regulatory subunits are suggested to have more specialized roles, including mediating inflammatory responses, histone degradation and the response to DNA damage[3,13–16]. The different catalytic cores, together with the diverse range of regulatory subunits, introduce great potential diversity for generating hybrid proteasomes of the 20S core particle with different combinations of regulatory caps, which may, in turn, alter protein cleavage[17,18]. For example, it was previously shown that different regulatory subunits of the proteasome serve as 'gate openers' to increase flux through the proteasome[3].

Various studies described correlations between proteasome regulators and cancer phenotypes. Subunits of the 19S were suggested to induce altered cell states, and selective inhibition of the 19S or catalytic subunits induced the accumulation of proteins involved in degradation machineries and conferred resistance to proteasome inhibitors[19]. While this may be easy to perceive, as the 19S includes the ubiquitin receptors, several other examples describe the preferential degradation of specific substrates by PSME1-4 for which no substrate selection mechanisms are known[3,18,20,21]. Thus, despite seminal studies that investigated proteasome cleavage in purified systems[7,22,23], we still lack a fundamental understanding of how different proteasome regulators may affect peptide cleavage by the catalytic subunits and, in turn, shape the endogenous cellular proteome. Mostly, this is due to the varying systems and use of model substrates for investigation. For example, there are conflicting reports on whether the PSME1-2 regulator binds more strongly to the immunoproteasome or positively affects antigen presentation[24–27]. Therefore, better understanding of proteasome complex heterogeneity, and its influence on the degradation landscape in different cancer types and within and between patients, is of clinical importance, bearing great potential to offer means to target, selectively, specific cancer vulnerabilities and to sensitize the response to ICI.

Here, by systematic examination of proteasome complex heterogeneity and response to ICI across hundreds of patients with bladder, lung, melanoma and renal cancers, we found that proteasome composition is highly variable across cancers and between patients. Using our recently established approach for proteasome profiling[28,29], we mapped the degradation landscapes in clinical samples of resected lung tumors. We discovered a distinct signature of proteasome degradation that was associated with non-small-cell lung carcinoma (NSCLC). Notably, we found an upregulation of PSME4 in lung tumors, which was associated with resistance to ICI therapy, thereby defining a 'cold' tumor. Biochemical, immunological and cellular characterizations of the functional consequences of PSME4 upregulation reveal that it directly attenuates immunoproteasome activity, leading to restriction of the antigenic diversity and, in turn, prohibits antitumor immunity in vivo. Collectively, our findings uncover the degradation landscape of NSCLC and elucidate a causal role of tumor-intrinsic PSME4 in shaping the tumor microenvironment, underscoring a mechanism of immune evasion. Beyond insight into mechanisms of proteasome-mediated tumor immunogenicity, our work introduces a paradigm by which proteasome complex composition, beyond the constitutive and immunoproteasome catalytic subunits, should be examined in the context of precision oncology and the response to immunotherapy in NSCLC and other cancer types.

Results

Proteasome complex heterogeneity associates with response to immunotherapy

Recently, increased immunoproteasome expression in cancer was suggested to promote response to ICI[10–12]. However, systematic examination of proteasome complex compositions, including different combinations of both catalytic and regulatory subunits, and their influence on tumor immunogenicity and response to ICI was not examined to date. To address this question, we examined the expression of proteasome subunits (Fig. 1a) across a pan-cancer cohort assembled from RNA sequencing (RNA-seq) information in The Cancer Genome Atlas Genomic Data Commons Pan-Cancer (TCGA-GDC PANCAN, 32 cancer types, $n = 9{,}724$ patients) and various patient immunotherapy response datasets[30,31]. We first examined the distribution of expression of the different proteasome subunits across 32 different cancer types from TCGA data (Fig. 1b and Extended Data Fig. 1a). Notably, the regulatory caps PSME3 and PSME4 were among the subunits with the most variable expression across cancers. Next, we stratified patients across cancer types based on their proteasome composition, including both catalytic cores and regulatory subunits (Fig. 1c, top and bottom, respectively). Interestingly, the expression of different catalytic cores did not define the expression of the regulatory subunits. For example, in uveal melanoma cancers (UVM; $n = 80$), we find about 50% of tumors are enriched with constitutive proteasome and 50% are enriched with immunoproteasome. However, these same tumors predominantly express PSME3 or PSME4 and not the PSME1/2 regulatory subunits. On the other hand, other cancer types that exhibit a similar level of immunoproteasome expression such as lung adenocarcinoma (LUAD; $n = 524$) and skin cutaneous melanoma (SKCM; $n = 103$) exhibit completely different frequencies of regulatory subunits expression (for example, mixed populations versus PSME3-enriched).

As immunoproteasome expression was previously associated with response to ICI in melanoma, we hypothesized that the regulators of the proteasome may also be associated with the response to ICI. To assess this, we calculated the effect size of the association with ICI response across the cohorts (bladder, melanoma, kidney and lung cancer from refs. 30,31) for each proteasome core subunit, catalytic subunit and regulatory cap (Fig. 1d). To control for the potential bias of data pooling, we combined the individual effect sizes of each biomarker in each cohort (Extended Data Fig. 1b)[30]. As previously reported, the immunoproteasome (specifically the subunit PSMB10) was associated with response to ICI but to a lesser extent than tumor mutational burden (TMB), which was previously shown to be one of the strongest classifiers of responsiveness to ICI[30]. Surprisingly, among all of the proteasome subunits examined across different cancer types, the proteasome regulator PSME4 was the only subunit that was significantly associated with lack of response to ICI (PSME4, $P = 0.0015$; TMB, $P = 0.0154$). Importantly, a role for PSME4 in tumors has not been shown to date. Further, we found that PSME4 did not strongly correlate with other biomarkers from the cohort and that it had a significant contribution to a general linear regression model of responsiveness even when the other significant biomarkers, such as TMB, were included (Extended Data Fig. 1c). Notably, when we stratified patients who had been treated with ICI, based solely on their regulatory subunit expression, we found that patients who have tumors enriched with PSME4 feature significantly reduced survival compared with the other groups, particularly compared with tumors enriched with PSME1/2 regulatory subunits (Fig. 1e). This was in stark contrast to the results obtained by examining survival across the patients who were mostly not treated with immunotherapy (TCGA cohort, $n = 9{,}724$ patients), where we did not detect any difference in survival between the PSME4 and PSME1/2 groups (Extended Data Fig. 2a–d). Indeed, PSME4 levels were significantly higher in the tumors of patients who did not respond to therapy, and, in agreement, the response rate to ICI was significantly lower in patients with high levels of PSME4 (Fig. 1f,g). Together, these data suggest that PSME4 may be involved in resistance to ICI therapy.

https://doi.org/10.1038/s43018-023-00557-4

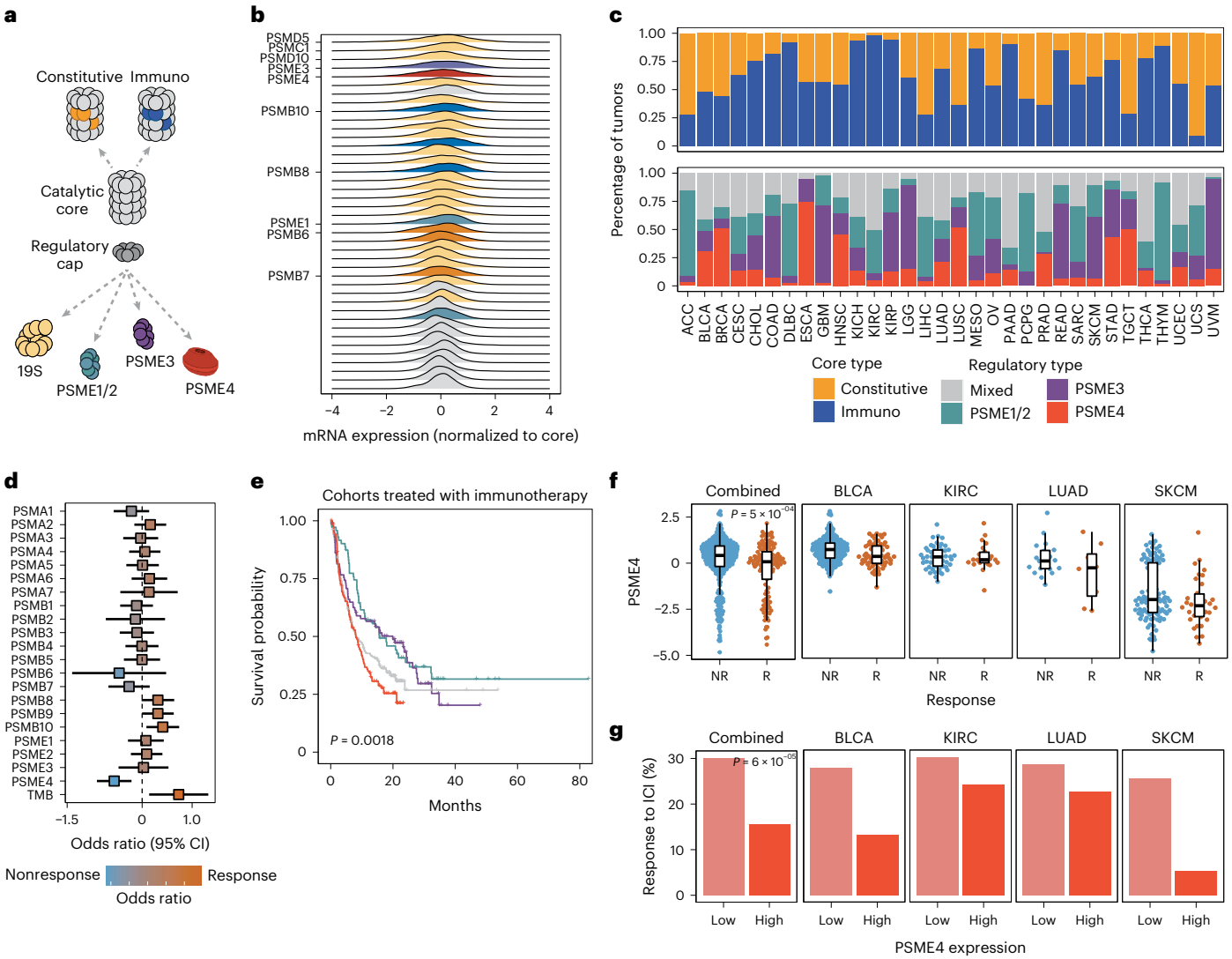

Fig. 1 | Proteasome composition heterogeneity is a factor in immunotherapy response. a, Schematic representation of proteasome complexes including the catalytic and regulatory subunits. **b**, The distribution of expression of each proteasome subunit across the cancer cohorts. Subunits are sorted by variance (n = 9,724 tumors). **c**, Tumors were clustered by the expression of either the catalytic (top) or regulatory subunits (bottom). The percentages of tumors in each cancer type that were assigned to each cluster are indicated (n = 9,724 tumors). Abbreviations for cancer types are according to TCGA. **d**, The effect size (calculated as the $\log_2$ odds ratio for response versus no response) and significance of the proteasome subunit biomarkers and TMB in meta-analysis across all cohorts incorporating the effect sizes and standard errors from each individual cohort (n = 331 BLCA, 134 SKCM, 72 KIRC, 27 LUAD tumors; center indicates odds ratio with bars at 95% confidence intervals (95% CIs)). **e**, Kaplan–Meier curve of patient survival stratified by the regulatory subunit clusters defined in **c** for the immunotherapy response cohorts (log-ranked P value = 0.0018; n = 331 BLCA, 128 SKCM, 27 LUAD tumors). **f**, The expression of PSME4 in the patients who responded to ICI (R) or did not respond (NR) from each of the ICI cohorts divided by cancer type (n = 331 BLCA, 134 SKCM, 72 KIRC, 27 LUAD tumors) or shown combined (Wilcoxon rank-sum test P value = 5×10^{-4}). Box plots span the first to third quartiles and whiskers show 1.5 × interquartile range. **g**, Patients were stratified by PSME4 expression in the ICI cohorts and the response rates for the PSME4-low and PSME4-high groups are shown (χ^2 $P = 6 \times 10^{-5}$; number of tumors as in **f**). BLCA, bladder urothelial carcinoma; KIRC, kidney renal clear cell carcinoma.

PSME4 is increased in NSCLC, corresponding to a cold tumor signature

Next, we sought to determine which cancer types, among those being treated with ICI, may be most likely impacted by increased levels of PSME4. Based on our analysis across the TCGA cohorts, we found that lung cancers had highly increased expression of PSME4 compared with adjacent or normal tissue (Fig. 2a). Using immunohistochemistry (IHC) staining of sections from human lung adenocarcinoma tumors, we confirmed that PSME4 is significantly increased in protein abundance in the tumor tissue (Fig. 2b) and that it is predominantly expressed in the nucleus of the cancer cells (Fig. 2b and Extended Data Fig. 2e,f; n = 8). We further corroborated that PSME4 is significantly upregulated in NSCLC tumors compared with the adjacent lung tissue by western blot analyses in two independent cohorts (Fig. 2c,d) and the Clinical Proteomic Tumor Analysis Consortium[32] (CPTAC) data (n = 110 samples; Fig. 2e) (Fig. 2c–e and Extended Data Fig. 2g,h). To ascertain a change in proteasome composition one needs to confirm binding to the proteasome complex as increased expression alone does not necessarily signify a change in proteasome complex assembly. We therefore examined whether PSME4 is indeed bound to cellular proteasomes in the cancerous tissues. To that end, we immunoprecipitated proteasomes from the tumor and adjacent tissue using an αPSMA1 antibody, which recognizes all proteasome subspecies. We found that among the regulatory subunits, PSME4 and PSME3 are significantly more incorporated into

https://doi.org/10.1038/s43018-023-00557-4

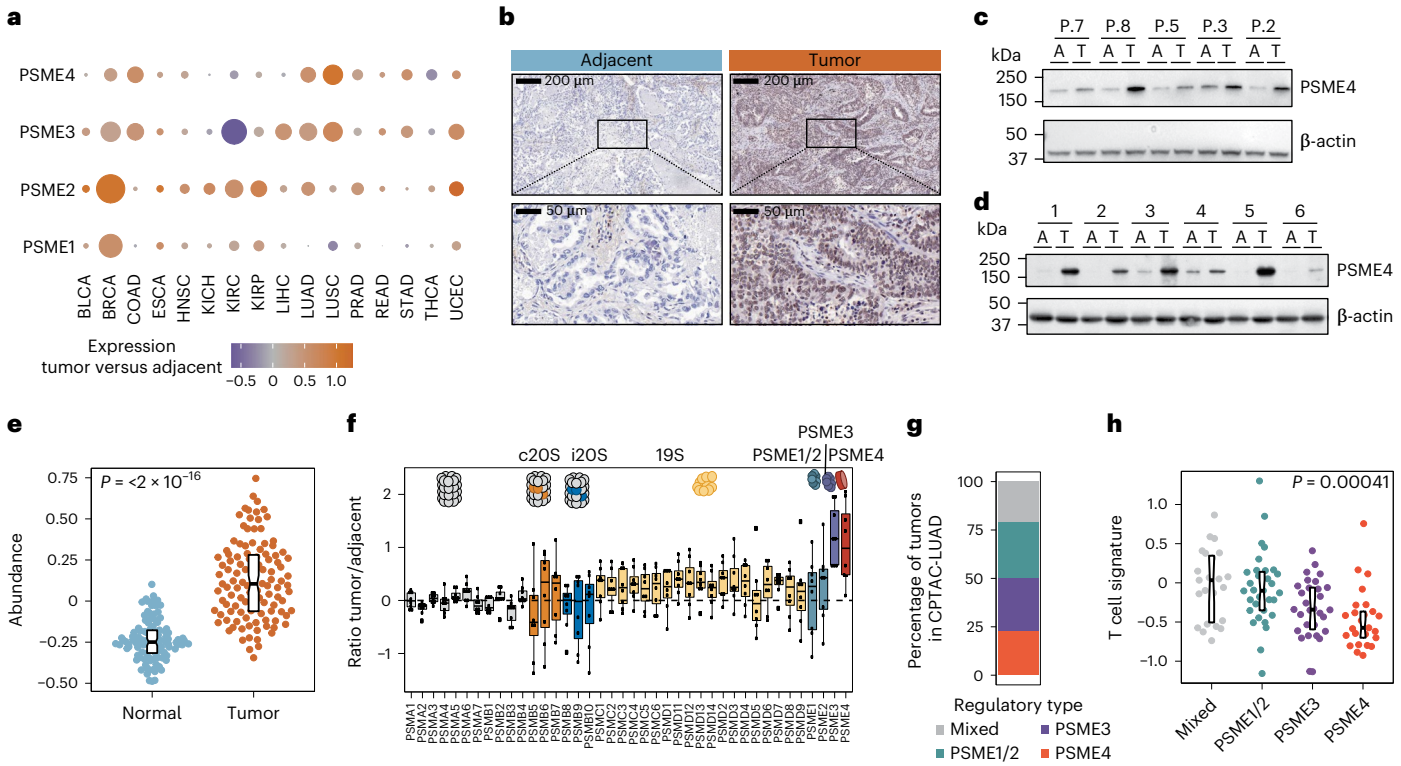

Fig. 2 | PSME4 is increased in lung adenocarcinoma and defines a reduced T cell signature. a, The ratio between tumor and adjacent expression for the indicated subunits in the indicated cancer type. Circle size indicates significance based on Wilcoxon rank-sum test (*P* values in the Source data) and color indicates the difference between mean expression in the tumor and adjacent tissue ($n = 9{,}724$ tumors). Abbreviations for cancer types are according to TCGA. **b**, IHC staining of PSME4 in the tumor and adjacent tissues. Blue color is negative stain and PSME4 is brown. Staining depicts PSME4 upregulation in the tumor tissue and its nuclear localization (scale bars, 200 µm in the upper panels and 50 µm in the lower panels, representative of $n = 9$ patients). **c**,**d**, Tumor (T) and adjacent (A) tissues from an Israeli (**c**) or German (**d**) cohort were immunoblotted for PSME4. β-Actin was used as a loading control (experiment was repeated twice with similar results). **e**, Abundance of PSME4 in tumor and adjacent tissues from the CTPAC-LUAD proteomics cohort (Wilcoxon rank-sum test $P < 2 \times 10^{-16}$; $n = 102$ adjacent, 111 tumors). Box plots span the first to third quartiles and whiskers show 1.5 × interquartile range. **f**, The ratio between subunit abundance in the proteasomes immunoprecipitated from tumor and adjacent tissues per patient ($n = 8$ tumors, 8 adjacent). Colors and diagrams indicate the identities of the proteasome subunits. Box plots span the first to third quartiles and whiskers show 1.5 × interquartile range. **g**,**h**, The CPTAC-LUAD cohort ($n = 111$ tumors) was stratified by regulatory subunit expression (**g**) and a T cell signature is shown for the tumor samples in each of the four clusters (**h**; Kruskal–Wallis $P = 0.00041$). Box plots span the first to third quartiles and whiskers show 1.5 × interquartile range.

proteasome complexes in the tumor tissue compared with the adjacent controls (Fig. 2f). While PSME4 is increased in NSCLC tumors, we did not detect any strong associations with LUAD grade, stage, site, driver mutation (for example, KRAS, EGFR) or clinical patient parameters either in the CPTAC proteomics cohort ($n = 110$; Extended Data Fig. 3a–d) or from histochemistry staining ($n = 50$; Extended Data Fig. 3e–i).

To examine the pathways that may be affected by the levels of PSME4, we stratified tumors in the CPTAC-LUAD proteomics cohort[32] ($n = 110$) by abundance of the different regulatory subunits (Fig. 2g). We found that T cell-related pathways are the most enriched in PSME4-low tumors using multiple different annotation sets (Extended Data Fig. 4a–c). Furthermore, we found that a 'T cell signature' defined by: GZMA, GZMB, PRF1, CXCL9, CXCL10, CD8A and CD4 is strongly reduced in the PSME4-enriched tumors compared with the other regulatory caps (Fig. 2h). Taken together, these results suggest that the observed upregulation of PSME4 in NSCLC may be associated with altered T cell-mediated antitumor immunity.

PSME4 modulates proteasome activity and alters the NSCLC degradome

As PSME4 was predominantly expressed in the cancer tissue and not the infiltrates (Fig. 2b), we set to examine whether it affects the transcriptional program and tumor inflammation in NSCLC. Notably, when we examined the effect of depleting PSME4 in A549 cells, we found only a mild impact on gene expression by RNA-seq. None of the genes with altered expression had known associations with tumor–immune interactions (Extended Data Fig. 4d–g), suggesting that the effect exerted by PSME4 on the response to ICI may be mediated through a posttranscriptional mechanism and directly by altering proteasome activity. We therefore sought to determine whether PSME4 alters proteasome function or degradation. To that end, we utilized our proteasome profiling approach, MAPP (mass spectrometry analysis of proteolytic peptides[28,29]), to analyze the 'active degradome' in NSCLC. Tissue samples and adjacent tissue controls (as determined by a pathologist) from the same lungs were processed in parallel ($n = 8$ per group). We then isolated proteasomes from tumor samples and analyzed the nascent peptides that were either 'trapped' inside or closely associated with the proteasomes to detect patterns of degradation in single-peptide resolution (Fig. 3a). Indeed, proteomic analysis of both protein abundance and degradation revealed that different tumors had shared patterns of degradation that were distinguished from those of the adjacent controls (Extended Data Fig. 5a–f). When comparing the substrates that are degraded in the cancer tissue, we found an increase in the degradation of nuclear proteins (Extended Data Fig. 5g–i), consistent with the increased levels of PSME4 in the nucleus that were observed above (Fig. 2b). We next examined whether PSME4 is found only in the nucleus of cells. By fractionating the cell, we found that the abundance of PSME4 is higher in the nucleus (Extended Data Fig. 6a,b). However, we

then immunoprecipitated the intact proteasome complexes using an αPSMA1 antibody to capture all proteasome species. We found that the levels of PSME4 incorporated into nuclear and cytosolic proteasomes were not significantly different, although slightly higher in the nucleus (Extended Data Fig. 6c–e). This suggests that while there is a strong increase in the abundance of PSME4 in the nucleus, there is not a striking difference in PSME4-capped complexes compared with the cytosol.

Since MAPP identified the endogenously cleaved peptides as they were degraded by the proteasome, we next wished to examine the cleavage patterns across identified peptides in the cancerous tissue and the controls. We found that the carboxy-terminal residue of the degraded peptides differed significantly between the tumor and adjacent samples (Fig. 3b). While PSME4 does not possess intrinsic catalytic activity, it has been previously shown to alter cleavage specificity of the constitutive proteasome by inducing a conformational shift[13,14,18]. We therefore assessed whether PSME4 level was associated with the shift in cleavage signature in the patient-derived tumor samples. Indeed, the abundance of PSME4 was positively correlated with the caspase- and chymotryptic-like cleavage activities of the proteasome and negatively correlated with tryptic-like cleavage (Fig. 3c,d and Extended Data Fig. 6f). These correlations could not be explained by a general shift in the amino acid composition across the degraded substrates (Fig. 3e), suggesting that proteasome cleavage itself was altered.

Proteolytic activities of the constitutive proteasome and immunoproteasome are different[4–7]. We therefore examined whether the change in activity was due to PSME4 modulating just the constitutive proteasome, as previously reported, or also the activity of the immunoproteasome. By biochemical examination, we found that PSME4 bound both constitutive proteasome and immunoproteasome in a human lung cancer cell line (Fig. 3f and Extended Data Fig. 6g–k), suggesting that PSME4 can independently affect their activity. We then assessed the effect of supplementing recombinant PSME4 on proteasome activity in a cell-free system[33] using model substrates for defined catalytic activities (Extended Data Fig. 7a–c). In this controlled system, the only change is the supplementation of PSME4, allowing us to decouple the direct effect on proteasome function from other indirect effects (for example, transcriptional) which have been previously described for PSME4 (refs. 13,16). In accordance with the correlation of specific activities that were observed in the clinical samples above, we found that the caspase-like (β1) activity of the constitutive proteasome increased (Fig. 3g and Extended Data Fig. 7d), whereas the tryptic-like (β2) activity decreased, upon PSME4 supplementation (Fig. 3h and Extended Data Fig. 7e). By contrast, when examining the effect of PSME4 on immunoproteasome-associated activities, we found that all were inhibited (β1i, β2i and β5i) (Fig. 3i,j and Extended Data Fig. 7f–h). To reverse inhibition of immunoproteasome-associated activity, we depleted PSME4 (knock-down (KD) by shRNA) from A549 cells which both reduced the caspase-like (β1) activity of the constitutive proteasome (Fig. 3k) and increased the chymotryptic-like activity of the immunoproteasome (β1i; Fig. 3l). Thus, PSME4, which enhances caspase-like activity that is associated only with the constitutive proteasome, is also attenuating the cleavage activities of the immunoproteasome. Notably, to our knowledge, to date there is no other description of a proteasome subunit that elicits asymmetric and opposing effects on the balance of immunoproteasome and constitutive proteasome activities.

PSME4 reduces the antigenic diversity of MHC I-presented peptides

As proteasomes are components of the antigen processing machinery[2] and many of the peptides presented on MHC I are proteasome-derived, we hypothesized that the changes induced by PSME4 on proteasome activity may also alter antigen processing and presentation. We first examined the total surface levels of human leukocyte antigen (HLA), finding that depleting PSME4 increases surface HLA, while overexpression (OE) of PSME4 reduces it beyond the levels of A549 with scrambled control (Fig. 4a and Supplementary Fig. 1a). Next, we used acid to strip the cell surface of HLA molecules. We found that cells depleted of PSME4 recover surface HLA faster than controls, while cells with overexpression of PSME4 have delayed recovery (Extended Data Fig. 7i,j and Supplementary Fig. 1b). To examine whether this is due to a defect in HLA expression or loading, we examined both extracellular surface HLA and intracellular immature HLA. While PSME4 overexpression mildly reduces surface HLA within 6 h of recovery from acid stripping, intracellular HLA is higher, suggesting that there is an accumulation of immature unloaded HLA molecules upon PSME4 overexpression (Extended Data Fig. 7k,l and Supplementary Fig. 1c). Whether the effect we observe is solely due to change in antigenic peptide generated or whether it may also be affected by the rate of maturation/loading of HLA remains to be elucidated. However, based on the change in HLA presentation, we hypothesized that the PSME4-driven restriction of proteasome activity reduces the pool of peptides that can be presented. To address this possibility, we performed HLA immunopeptidomics of A549 lung cancer cells with PSME4 knockdown (KD) by shRNA and controls (treated with control shRNA (denoted Ctrl)) (Fig. 4b and Extended Data Fig. 8a–c). As expected, we observed a significant increase in the abundance of peptides presented on the cell surface upon PSME4 KD, consistent with the increase in surface HLA molecules (Fig. 4c). This is despite the fact that we did not detect any PSME4-driven shift in

Fig. 3 | PSME4 restricts proteasome activity in lung adenocarcinoma. **a**, Schematic representation of the workflow. Analysis of lung adenocarcinoma and adjacent lung tissue was performed using standard whole-cell extract proteomics to assess protein abundance and MAPP to study the proteasome composition and degradome of the sample ($n = 8$ tumor and 8 adjacent sections). Bottom, exogenous PSME4 was used to interrogate the effect on immunoproteasome and constitutive proteasome cleavage activity. **b**, MAPP-identified peptides were divided based on their carboxy-terminal residue. The percentage of peptides with each terminus was calculated for each sample and normalized across patient samples. Amino acids are annotated with their matching proteasome cleavage activity; rows are clustered using Pearson distances. The bars represent the percentage change for each amino acid at the carboxy terminus, comparing tumors ($n = 8$) and adjacent ($n = 8$) tissues. Box plots span the first to third quartiles and whiskers show 1.5 × interquartile range. **c**,**d**, The carboxy-terminal residue of peptides was used to classify peptides based on the proteasome activity attributed to their cleavage. The abundance of PSME4 in the samples based on whole cell proteomics correlated with the caspase-like signature (**c**; Spearman $\rho = 0.69$) and was anticorrelated with the tryptic-like signature (**d**; Spearman $\rho = -0.46$). In **c**–**e**, a value is shown for each of $n = 8$ tumor and 8 adjacent samples. **e**, The average amino acid percentage composition for all the peptides identified by MAPP in the tumor samples (y axis) is plotted against the corresponding adjacent samples (x axis). **f**, Proteasome complexes were immunoprecipitated (IP) with αPSME4 antibody from A549 cells that were either treated with TNF-α and IFN-γ or left untreated and blotted for the indicated proteasome subunits. Experiments were repeated twice with similar results. **g**–**j**, Proteasome activity assays using the nLPnLD-AMC (**g**), RLR-AMC (**h**), PAL-AMC (**i**) or ANW-AMC (**j**) fluorogenic substrate to measure the activity of indicated subunits. Relative fluorescence units (RFU) of the substrate are shown across the 3.5 h of the experiment (left) or at the endpoint (right). A549 lysates were untreated (**g**), to measure the constitutive proteasome activity, or treated with TNF-α and IFN-γ (**h**–**j**), to measure the immunoproteasome activity. Recombinant PSME4 was added to the lysate where indicated (red, two-sided paired Student's t-test; **g**: $P = 0.0034$, **h**: $P < 0.0001$, **i**: $P = 0.0003$, **j**: $P = 0.0004$; box plots indicate median and quartiles, bars from min to max, $n = 4$ independent samples). **k**,**l**, Lysates were collected from PSME4-depleted A549 (KD) or control (Ctrl). Proteasome activity assays were performed using the nLPnLD-AMC (**k**) in unstimulated lysates or PAL-AMC (**l**) in lysates treated with TNF-α and IFN-γ. RFU of the substrate is shown across the 3.5 h of the experiment (left) or at the endpoint (right; two-sided paired Student's t-test; $^*P < 0.05$, $^{****}P < 0.0001$; box plots indicate median and quartiles, bars from min to max, $n = 4$ independent samples). AA, amino acid; Ctrl, control. Figure 3a created with BioRender.com.

https://doi.org/10.1038/s43018-023-00557-4

general protein abundance in the proteome (Extended Data Fig. 8d). Likewise, we did not observe that the increase in peptides is due to increased binding to any specific HLA haplotype (Extended Data Fig. 8e). Next, we examined the termini of the presented peptides as proteasome cleavage is thought to impact the carboxy termini whereas aminopeptidases (for example, ERAP1) are thought to cleave the N terminus. Therefore, we divided the peptides based on whether they had a caspase-, tryptic- or chymotryptic-like carboxy terminus. We observed that the chymotryptic- and tryptic-like peptides were increased upon PSME4 depletion, consistent with the effect we detected on proteasome activity (Fig. 4d). Furthermore, we found that peptides ending with the caspase-like glutamic acid (E) were significantly reduced by the depletion of PSME4, while peptides with the tryptic-like lysine (K) were the most significantly increased (Fig. 4e,f and Extended Data Fig. 8f).

Previous studies[34] have shown that peptides with caspase-like termini do not bind as well as peptides with tryptic- or chymotryptic-like termini to HLA molecules. In the immunopeptidome analysis,

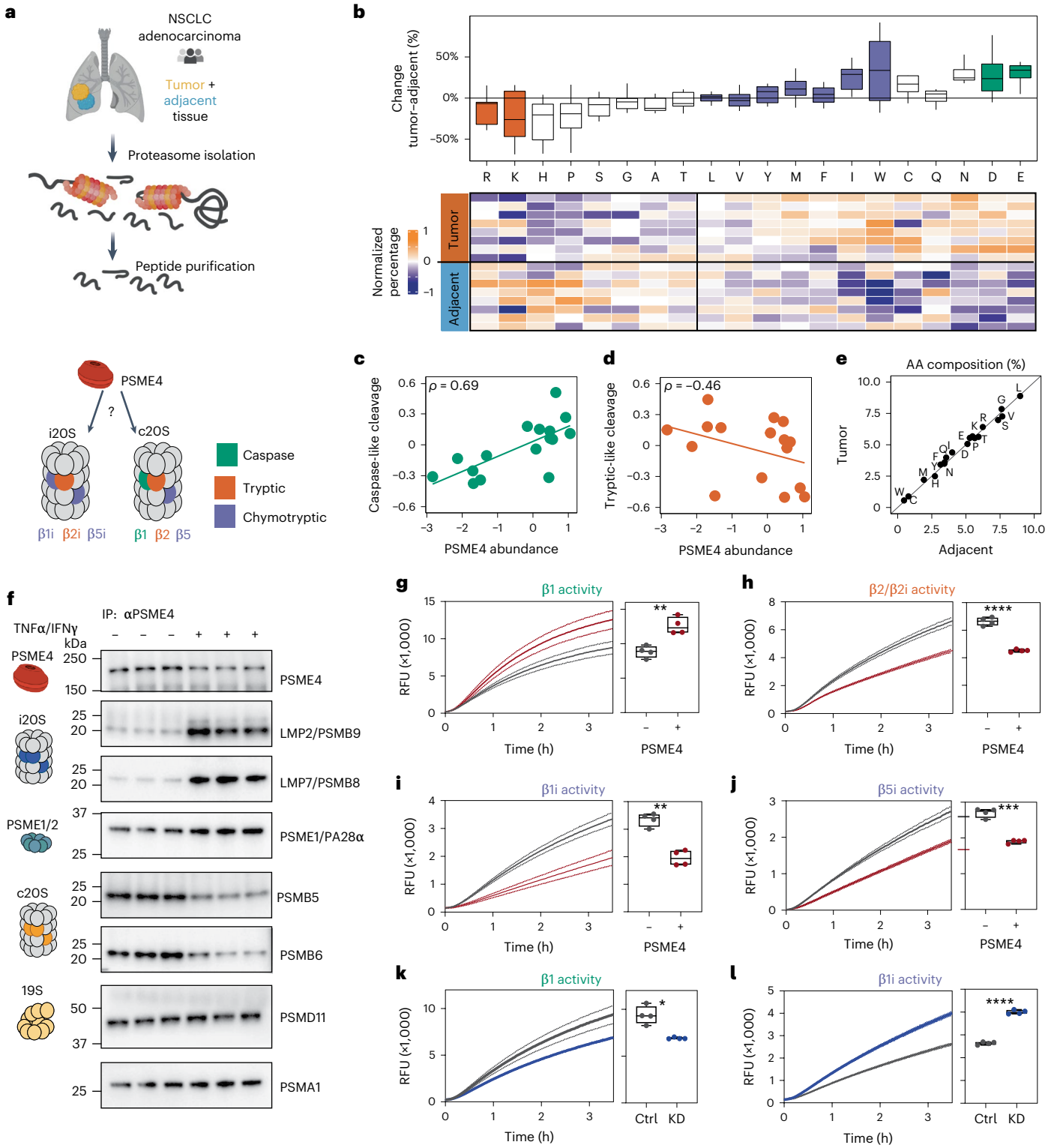

https://doi.org/10.1038/s43018-023-00557-4

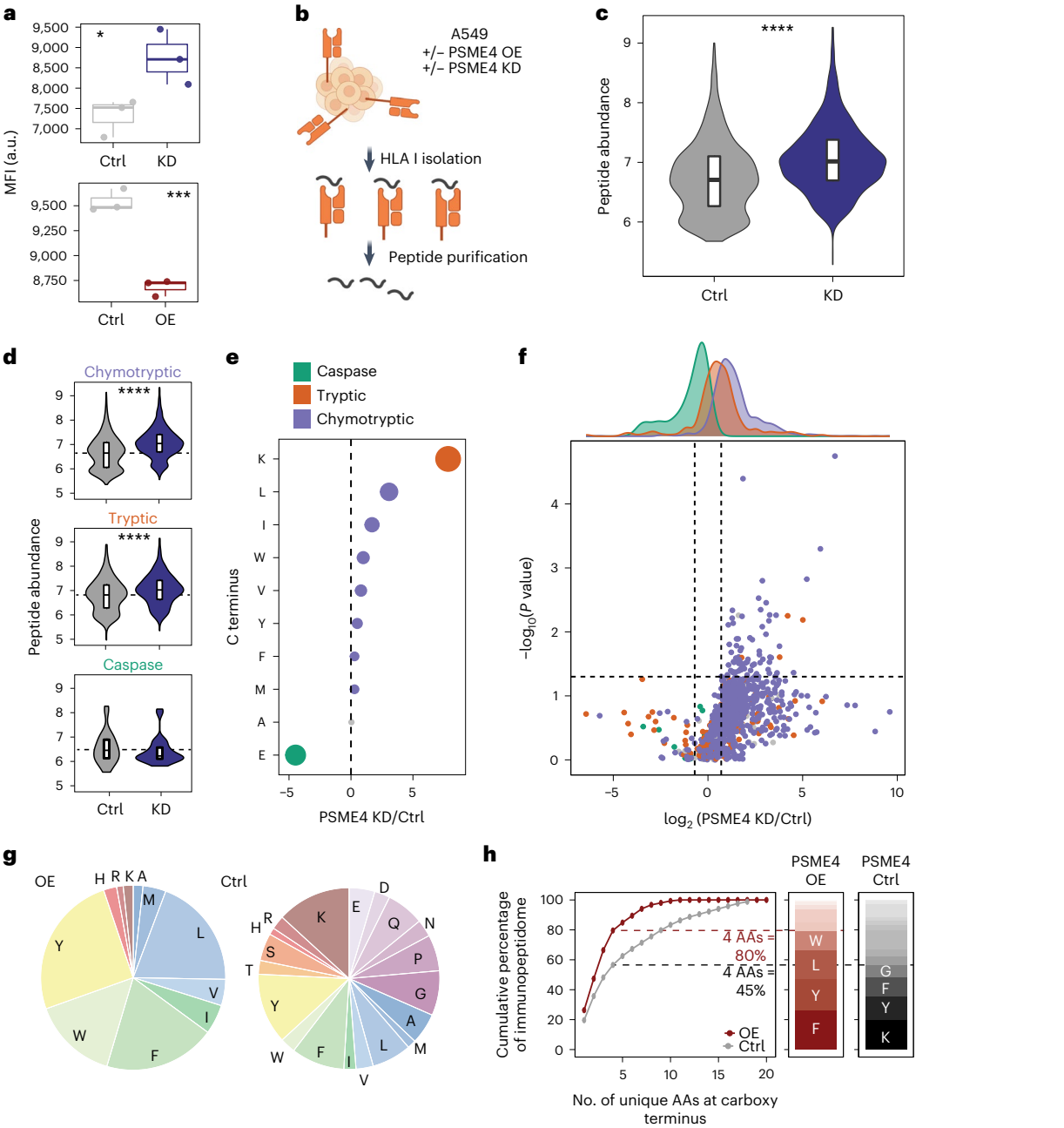

Fig. 4 | PSME4 restricts immunopeptidome diversity thereby reducing antigen presentation. a, Median fluorescence intensity (MFI) from flow cytometry analysis of HLA I expression using the W6/32 antibody on A549 cells with PSME4 KD and control (top; Welch's corrected two-sided *t*-test $^{*}P = 0.047$, $^{***}P = 0.0007$) or PSME4 OE and control (bottom; ***Welch's corrected two-sided *t*-test $P < 0.001$). Box plots span the first to third quartiles and whiskers show 1.5 × interquartile range, $n = 3$ independent samples. **b**, Immunopeptidomics workflow. **c**, Distribution of median peptide abundance of the immunopeptidome ($n = 3$ independent samples per condition) from the control (Ctrl) and PSME4 KD conditions (Wilcoxon rank-sum test $^{****}P < 2.2 \times 10^{-16}$; $n = 1{,}335$ peptides). Box plots span the first to third quartiles and whiskers show 1.5 × interquartile range. **d**, Peptides were divided by their carboxy-terminal motif and the abundance distributions of the caspase-, tryptic- and chymotryptic-like peptides in the PSME4 KD condition or shCtrl are shown (Wilcoxon rank-sum test chymotryptic $P < 2.2 \times 10^{-16}$, tryptic $P = 8.1 \times 10^{-10}$; $n = 1{,}335$ peptides). Box plots span the first to third quartiles and whiskers show 1.5 × interquartile range. **e**, Peptides are grouped by their carboxy termini. For each amino acid, the circle size indicates the significance of the fold change between PSME4 KD and Ctrl compared with the background (Student's *t*-test). The *x*-axis score is the negative $\log_{10}$-transformed *P* value multiplied by the sign of the fold change. **f**, Volcano plot of the peptides with the fold change and significance between the PSME4 KD and Ctrl conditions. Peptides are colored by carboxy-terminal motif. **g**, The percentage of each amino acid in the carboxy termini of the peptides differentially presented on MHC molecules in the A549 cells overexpressing PSME4 (OE) versus empty vector control (Ctrl). **h**, The cumulative percentage of peptides explained by the number of different amino acids (from 1 to all 20) at the carboxy termini (end position) in the control (Ctrl, gray) and PSME4 OE (OE, red) immunopeptidomes. Figure 4b created with BioRender.com.

we also observed fewer caspase-like peptides compared with the other types (Fig. 4f) and they had lower predicted binding to MHC using the netMHC prediction software. We therefore hypothesized that overexpressing PSME4 will further reduce the pool of antigens that can be presented. We examined this by repeating the immunopeptidomics, with and without overexpressing PSME4, to mimic the PSME4 upregulation observed in NSCLC (Extended Data Fig. 8g–j). Of the peptides identified, 463 peptides (~10%) were significantly changed

https://doi.org/10.1038/s43018-023-00557-4

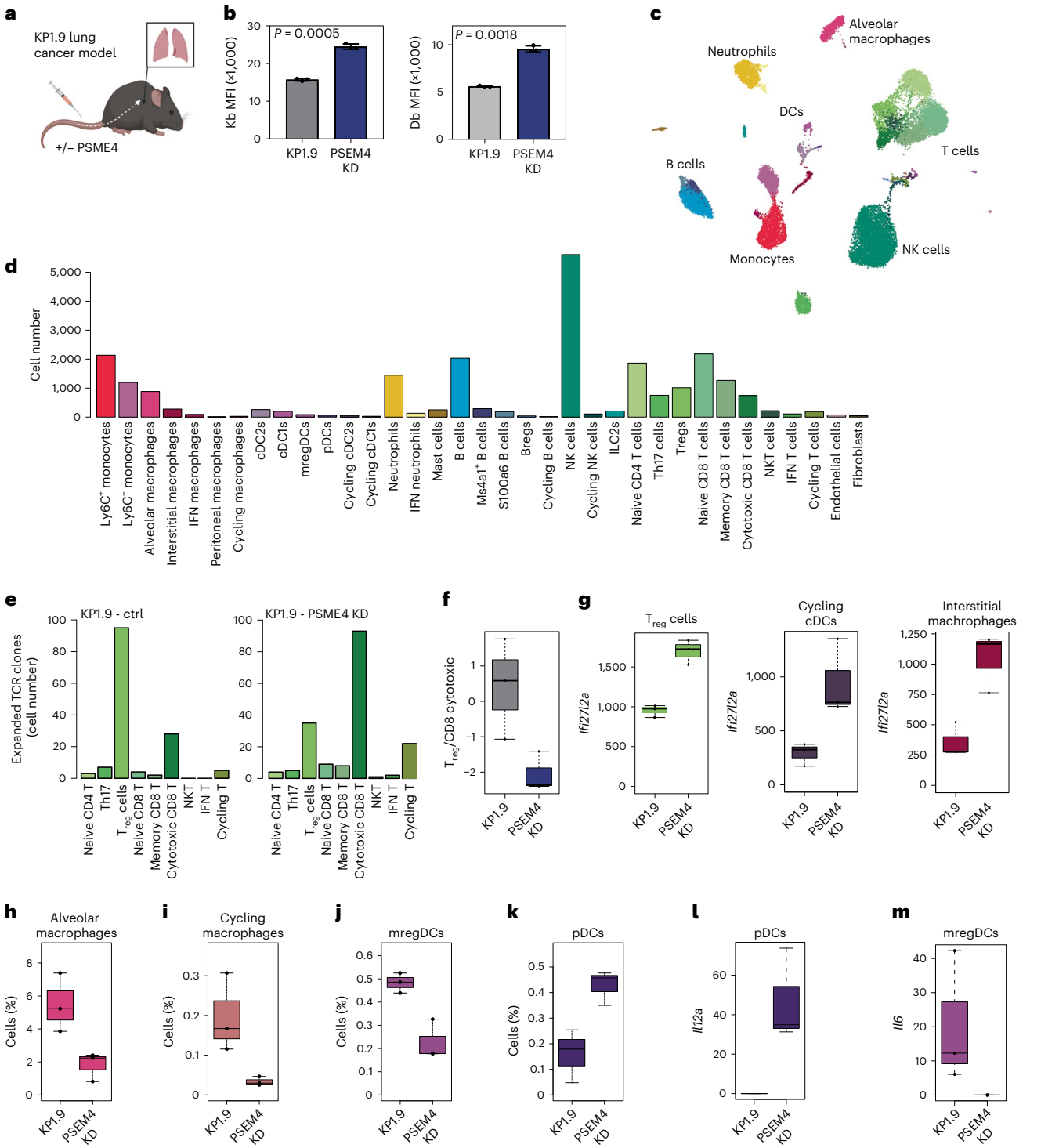

Fig. 5 | PSME4 reduces CD8⁺ T cell infiltration into tumors and promotes an immunosuppressive environment. a, Schematic of orthotopic lung tumor models by tail vein injection of KP1.9 cells or KP1.9$^{PSME4\ KD}$ to C57/B6 mice. **b**, MFI from flow cytometry analysis of MHC I expression using a Kb or Db antibody on KP1.9 or KP1.9$^{PSME4\ KD}$ cells ($n = 3$ mice per group; bars indicate mean ± s.d.; two-sided Student's *t*-test). **c**, Uniform manifold approximation and projection (UMAP) visualization showing 35 cell populations across the three replicates from mice bearing KP1.9 (Ctrl) or KP1.9$^{PSME4\ KD}$ tumors. **d**, Bar graph showing total number of cells per cell type identified across the three replicates from mice bearing KP1.9 (Ctrl) or KP1.9$^{PSME4\ KD}$ tumors. **e**, Bar plot showing numbers of TCR clones that were expanded (at least two cells sharing the same TCR clone) in the different T cell populations in a representative sample from mice injected with KP1.9 or KP1.9$^{PSME4\ KD}$ cells. **f**, Ratio of number of expanded (that is, having nonunique TCR) T_{reg} cells to cytotoxic CD8 cells in each sample ($n = 3$ KP1.9 and 3 KP1.9$^{PSME4\ KD}$). Box plots span the first to third quartiles and whiskers show 1.5 × interquartile range. **g**, Box plots showing pseudo-bulk tpm expression of *Ifi27l2a* in cycling cDCs, interstitial macrophages and T_{reg} cells in the lungs of mice ($n = 3$ mice per group) injected with KP1.9 or KP1.9$^{PSME4\ KD}$ cells. Box plots span the first to third quartiles and whiskers show 1.5 × interquartile range. **h**–**k**, Box plots showing relative abundances of alveolar macrophages (**h**), cycling macrophages (**i**), mature DCs enriched in immune-regulatory molecules (mregDCs) (**j**) and pDCs (**k**) in the lungs of mice injected with KP1.9 ($n = 3$ mice) or KP1.9$^{PSME4\ KD}$ cells ($n = 3$ mice). Box plots span the first to third quartiles and whiskers show 1.5 × interquartile range. **l**,**m**, Box plots showing pseudo-bulk tpm expression of *Il12a* in pDCs (**l**) or *Il6* in mregDCs (**m**) in the lungs of mice injected with KP1.9 ($n = 3$) or KP1.9$^{PSME4\ KD}$ cells ($n = 3$ mice). Box plots span the first to third quartiles and whiskers show 1.5 × interquartile range. cDC, classical dendritic cells; NK, natural killer; tpm, transcripts per million.

in abundance upon PSME4 overexpression compared with the controls (Extended Data Fig. 8k). Further, we found a change in the carboxy termini (Extended Data Fig. 8l) of the presented peptides, specifically observing a reduction in positively charged residues (R and K), akin to their increase in the PSME4-depleted setting. When examining the distribution of amino acids across the differentially presented peptides, we found that the peptides presented in the PSME4-overexpresing cells were less diverse than those in the control cells (Fig. 4g). Notably, only four residues in the overexpressing cells, compared with nine residues in the controls, made up 80% of the carboxy termini of the peptides associated with MHC binding, indicating that PSME4 overexpression substantially restricts the diversity of presented antigens (Fig. 4h). Beyond the biochemical properties of the peptides, by examination of the protein source of the presented peptides, we found an enrichment of nuclear proteins in the immunopeptidome following PSME4 overexpression (Extended Data Fig. 8m), concordant with the observed increase in degradation of nuclear proteins mentioned above (Extended Data Fig. 5h). Taken together, these data indicate that PSME4 shifts the presented peptide repertoire, reducing the diversity of the anchoring residues in the presented antigens, and that its upregulation, in the context of lung cancer, may have deleterious effects on antitumor immunity.

PSME4 abrogates antitumor immunity in NSCLC

As PSME4 was associated with a reduced T cell signature (Fig. 2h) and directly affected antigen presentation through modulating proteasome activity, we hypothesized that it might affect the interaction between tumor cells and cytotoxic T cells. To examine this, we utilized the KP1.9 cells derived from a *Kras*^{G12D}; *Trp53*$^{-/-}$ murine lung adenocarcinoma in an orthotopic murine model. We established KP1.9 isogenic cell lines with PSME4 KD (KP1.9$^{PSME4\ KD}$; Fig. 5a and Extended Data Fig. 9a–f). Depletion of PSME4 reduced its levels to be comparable to those of normal lung epithelial cells (Extended Data Fig. 9b,c). As we observed that PSME4 alters proteasome activity and reduces antigenic diversity, we first examined the effect on antigen presentation in the mouse model. Indeed, depletion of PSME4 increased the level of surface MHC I by about 50% in KP1.9 (Fig. 5b, Extended Data Fig. 9g and Supplementary Fig. 2). We hypothesized that this may drive changes in the interaction between tumor and immune infiltrates. To address this question, we analyzed the changes in the immune milieu by performing single-cell RNA-seq (scRNA-seq) of CD45$^+$ cells 3 weeks after the injection of parental KP1.9 or KP1.9$^{PSME4\ KD}$ tumor cells (Fig. 5c,d and Supplementary Fig. 3). This allowed an examination of the effect of PSME4 on the early immune response to the tumor, while avoiding bias due to differences in tumor burden. The overall distribution of cell types was similar among groups (Supplementary Figs. 4–12). To examine if there was a skew towards particular cell fates in the T cell compartment, we characterized the T cell populations and T cell receptors (TCRs). We reasoned that TCR clones that were not unique were the result of expansion (Fig. 5e and Supplementary Figs. 13 and 14). We found that cytotoxic T cell and regulatory T cell (T_{reg}) populations had considerably expanded such that there were more cytotoxic CD8 T cells in the KP1.9$^{PSME4\ KD}$ milieu whereas T_{reg} cells expanded in the KP1.9-bearing mice. Further, a difference in the T_{reg}/CD8 T cell ratio between the two groups was observed (Fig. 5f and Supplementary Figs. 15 and 16). Interestingly, we noted an increase in inflammatory responses through the expression of interferon (IFN) response gene *Ifi272a* in several cell types, including T_{reg} cells (Fig. 5g). The differences in T cell populations were accompanied by additional changes in other populations of the immune milieu, which promoted a pro-inflammatory environment in PSME4-depleted tumors. Specifically, the relative sizes of the alveolar and cycling macrophage clusters as well as *Ccr*$^+$ regulatory dendritic cells (DCs), which have been previously shown to play an immunosuppressive role in NSCLC[35,36], were smaller in the lungs of mice bearing KP1.9$^{PSME4\ KD}$ tumors than in the lungs of mice bearing KP1.9 tumors (Fig. 5h–j). Further, we observed an increase in plasmacytoid DCs (pDCs)[37] in the mice bearing KP1.9$^{PSME4\ KD}$ tumors, which exhibited a pro-inflammatory signature with the expression of *Il12a* and an enrichment for pathways related to antigen presentation and processing (Fig. 5k,l, Extended Data Fig. 9h and Supplementary Fig. 17). This is in contrast to the mature DCs enriched in immune-regulatory molecules, which are decreased in KP1.9$^{PSME4\ KD}$ and express higher levels of *Il6* (Fig. 5m and Extended Data Fig. 9i). Together, our results suggest that upregulation of PSME4 may drive immune evasion by reducing cytotoxic T cell activity and may play an active role in tumorigenesis by promoting an immune-suppressed microenvironment.

PSME4-high NSCLC tumors escape immune-mediated killing

To assess the effects of PSME4 on tumor progression, we tracked mice bearing KP1.9$^{PSME4\ KD}$ or parental KP1.9 tumors. As the lungs of KP1.9$^{PSME4\ KD}$-bearing mice did not have any detectible lesions even 7 weeks after injection, we included KP1.9 cells with overexpression (KP1.9$^{PSME4\ OE}$) as an additional comparison to unravel possible effects of PSME4 on tumor–immune interactions. KP1.9$^{PSME4\ OE}$ mice developed a marked weight loss starting a month from tumor cell injection (33 d), as compared with mice bearing KP1.9 tumors (Extended Data Fig. 10a). Lungs of mice bearing KP1.9$^{PSME4\ OE}$ tumors were significantly larger and contained numerous lesions, whereas lungs of mice bearing KP1.9$^{PSME4\ KD}$ did not show any detectable lesions (Fig. 6a,b and Extended Data Fig. 10b). These effects were not driven by a change in the proliferation rate of tumor cells (Extended Data Fig. 10c,d). To determine whether the effect on tumor progression (Extended Data Fig. 10e,f) was immune-mediated, we assessed the tumor infiltrating lymphocytes in lungs of tumor-bearing mice 7 weeks after tumor injection (Fig. 6c and Extended Data Fig. 10g–j). We found that KP1.9$^{PSME4\ OE}$ tumors exhibited a decrease in the CD8$^+$ T cell/T_{reg} cell ratio (Fig. 6c,d), coupled with a significant increase in exhausted PD1$^+$ CD8$^+$ T cells (Fig. 6e and Supplementary Fig. 18) and a decrease in IFN-γ in tumor

Fig. 6 | PSME4 abrogates antitumor immunity. a, The lung weights of mice bearing parental ($n = 7$), PSME4-overexpressing (KP1.9$^{PSME4\ OE}$; $n = 7$) or PSME4-depleted (KP1.9$^{PSME4\ KD}$; $n = 8$) tumors (two-sided Student's *t*-test $^{**}P = 0.0020$; bars indicate mean ± s.d.). **b**, Photograph of representative lungs from mice not injected with tumor cells (Non-inj) 41 d after the injection of parental, KP1.9$^{PSME4\ OE}$ or KP1.9$^{PSME4\ KD}$ cells. **c**, Hematoxylin and eosin staining of lungs from mice bearing KP1.9, KP1.9$^{PSME4\ OE}$ or KP1.9$^{PSME4\ KD}$ tumors (top) and immunofluorescence staining of the tumor sections with indicated antibodies (bottom). **d**, The ratio of CD8 T cells to T_{reg} cells in the spleens of mice bearing KP1.9$^{PSME4\ OE}$ ($n = 7$) or KP1.9 tumors ($n = 6$; two-sided Student's *t*-test $^{****}P < 0.0001$; bars indicate mean ± s.d.). **e**, The percentage of PD1-positive CD8 T cells in the lungs of the mice bearing KP1.9$^{PSME4\ OE}$ ($n = 5$) or KP1.9 tumors ($n = 6$; two-sided Student's *t*-test $^{*}P = 0.0440$; bars indicate mean ± s.d.). **f**, A histogram of IFN-γ-stained CD8 T cells of mice bearing KP1.9 (gray) or KP1.9$^{PSME4\ OE}$ (red) tumors. **g**, The MFI of IFN-γ-stained CD8 T cells in the lungs of mice bearing KP1.9$^{PSME4\ OE}$ ($n = 5$) or KP1.9 tumors ($n = 6$; two-sided Student's *t*-test $^{**}P = 0.0017$; bars indicate mean ± s.d.). **h**, The percentages of different subsets of CD8-positive lymphocytes (naive, early activated, effector memory (EM) or central memory (CM)) from a mouse bearing KP1.9 or KP1.9$^{PSME4\ OE}$ tumor. **i**, The percentage of naive CD8-positive lymphoytes, which are CD62L postitive and CD44 negative, in the lungs of mice bearing KP1.9$^{PSME4\ OE}$ ($n = 5$) or KP1.9 tumors ($n = 6$; two-way analysis of variance (ANOVA) with post hoc Tukey $^{**}P = 0.004$; bars indicate mean ± s.d.). **j**,**k**, KP1.9 cells were cocultured with splenic lymphocytes from mice bearing KP1.9 ($n = 7$), KP1.9$^{PSME4\ OE}$ ($n = 7$) or KP1.9$^{PSME4\ KD}$ ($n = 8$) tumors and the tumor cell death was assessed (**j**). **k**, The percentage of tumor cells from each coculture that is dead (two-sided Student's *t*-test $^{****}P < 0.0001$, $^{***}P = 0.0021$; bars indicate mean ± s.d.). **l**,**m**, Kaplan–Meier curves of survival of mice bearing KP1.9 or KP1.9$^{PSME4\ KD}$ tumors in a C57Bl/6J (**l**) or immune-deficient Rag1−/− (**m**) background. Figure 6j created with BioRender.com.

https://doi.org/10.1038/s43018-023-00557-4

infiltrating lymphocytes in KP1.9$^{PSME4\ OE}$ tumor-bearing mice (Fig. 6f,g), suggesting decreased tumor inflammation in these mice. Furthermore, we observed a decrease in naive CD8$^+$ T cells as observed by CD62L$^+$, CD44$^-$ (Fig. 6h,i and Extended Data Fig. 10k), suggesting that mice bearing KP1.9$^{PSME4\ OE}$ tumors exhibit reduced inflammation and T cell activation. These data suggest that an increase of

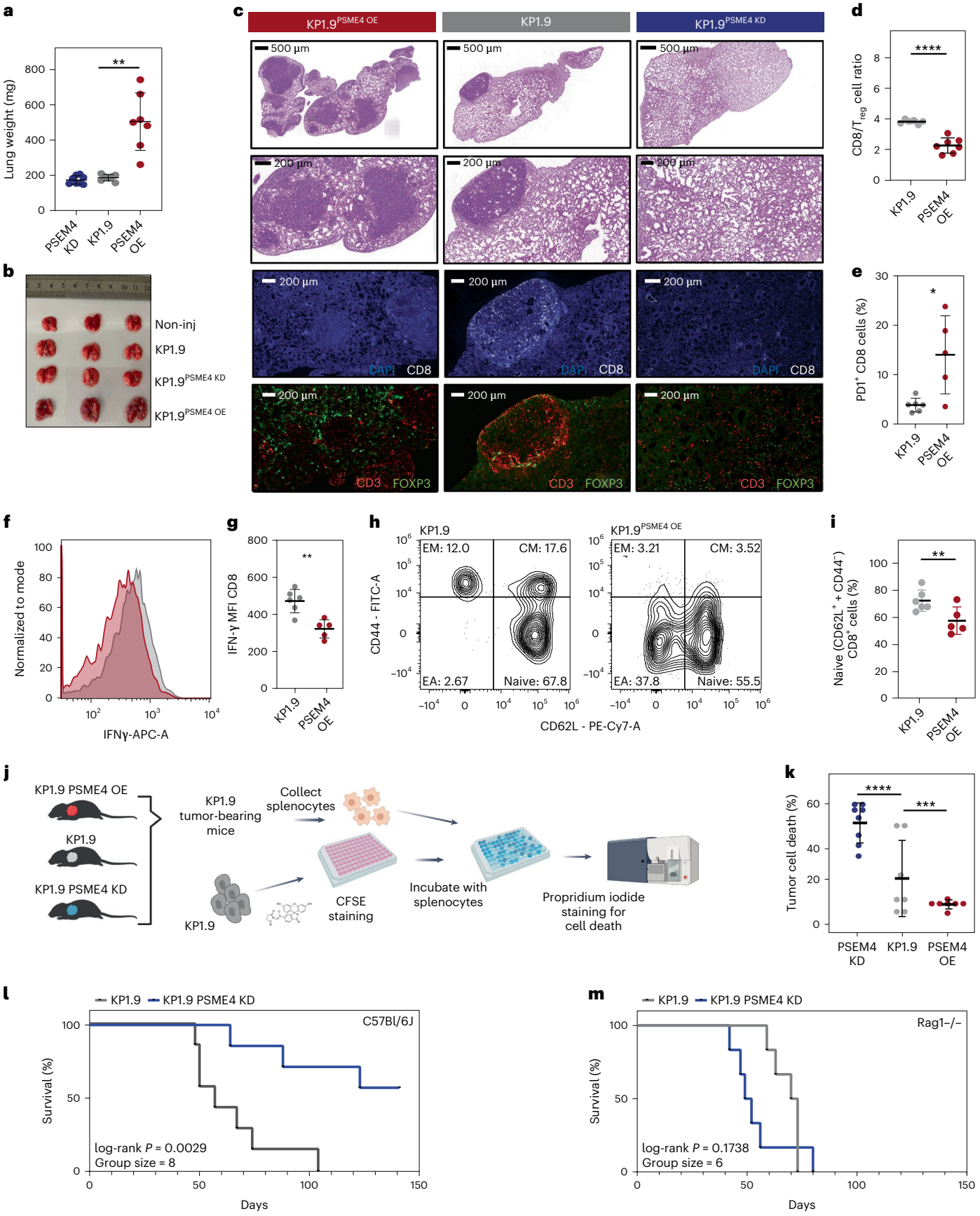

https://doi.org/10.1038/s43018-023-00557-4

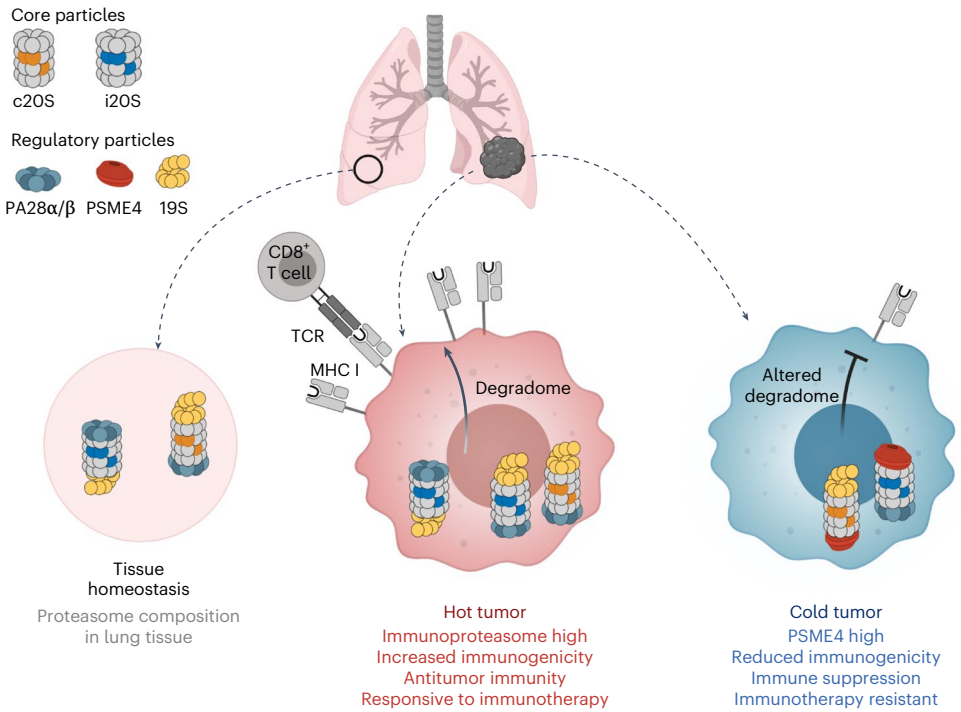

Fig. 7 | PSME4 attenuates immunogenicity in cold NSCLC tumors. In healthy lung tissue there is a homeostatic balance between the various proteasome complexes. In the case of NSCLC, however, there is a disruption of homeostasis, thereby altering tumor proteostasis. We find that cold NSCLC tumors, characterized by low inflammation and reduced lymphocyte infiltration, have higher expression of PSME4. This PSME4 upregulation leads to altered protein degradation, thereby reducing presentation of peptides on MHC I. By contrast, hot tumors are enriched in immunoproteasomes and depleted of PSME4-capped proteasomes. This in turn drives increased antigenic diversity for MHC I presentation and enhanced T cell-mediated antitumor immunity. Created with BioRender.com.

PSME4 levels in the tumor promotes an immunosuppressed tumor microenvironment.

Finally, to show a causal link between intratumoral levels of PSME4 and T cell-mediated killing, we tested the ability of splenic lymphocytes isolated from tumor-bearing mice to kill tumor cells (Fig. 6j). Importantly, the only perturbation in this in vivo system was the altered PSME4 level in the injected tumor cells. We found that splenic lymphocytes from mice bearing KP1.9$^{PSME4\ OE}$ tumors exhibited reduced propensity to kill KP1.9 cells (Fig. 6k). By contrast, splenic lymphocytes from mice bearing KP1.9$^{PSME4\ KD}$ tumors demonstrated enhanced killing compared with cells obtained from mice bearing KP1.9 tumors (Fig. 6k). These results indicate that the antitumor activity we observed indeed depended on loss of PSME4 in the KP1.9 tumor cells. This is notable because the KP1.9 tumor line has been shown to be highly non-immunogenic, yet with the depletion of PSME4 we were able to promote high levels of tumor killing. To further confirm that the PSME4-induced effect on tumor growth was mediated through adaptive immunity, we conducted survival experiments using RAG1-deficient mice, which lack an adaptive immune arm. In this model, no differences were observed in weight loss or survival in PSME4-deficient or PSME4-overexpressing tumors (Fig. 6l,m and Extended Data Fig. 10l), further corroborating that the PSME4-driven changes in tumor progression were mediated by an in vivo adaptive immune response.

Discussion

In this work, we highlight intrapatient heterogeneity in proteasome regulatory function as an important factor governing tumor immunogenicity and response to immunotherapy. We further exemplify that altered proteasome composition and function causally shape tumor–host interactions by demonstrating in NSCLC that PSME4-capped proteasomes play an anti-inflammatory role in cancer by attenuating immunoproteasome activity. The altered proteasome activity leads, in turn, to reduced antigenicity by restricting immunopeptidome diversity and altering surface HLA presentation (Fig. 7). This then abrogates antitumor immunity in murine models, which can be restored by depleting PSME4 in a KP1.9 lung adenocarcinoma model.

Our results feature several important implications. First, while label-free quantitative mass spectrometry (LFQ-MS) analysis of cell lines suggested that <5% of 20S proteasomes bear PSME4 regulators[17,38], our results suggest that this frequency is increased in many cancer types. As PSME4 is associated with histone organization and DNA damage sensing and repair[39–41], and NSCLC has been shown to be sensitive to proteotoxic stress[42], we speculate that PSME4 may be upregulated to offer a protective mechanism. Further, as PSME4 is known to play a nuclear role and was suggested to modulate transcription[43], it will be intriguing to comprehensively examine the potential effect its upregulation has on the transcriptional landscape. Although our analysis did not reveal global transcriptional changes in immune-related genes, it may be cancer- or condition-specific. Nevertheless, the dominant effect PSME4 has on the degradation landscape, and the altered catalytic activity of the immunoproteasome in cell-free systems, strongly suggest that PSME4 exerts its effect by directly modulating proteasome activity, posttranslationally.

Second, we found PSME4 to be a regulator that differentially modulates the activities of the constitutive proteasome and immunoproteasome. PSME4 has been shown to alter the conformation of constitutive 20S proteasomes[18], which we and others have found to increase the β1 caspase-like activity[14], although other reports show an increase of tryptic activity[18]. These discrepancies may stem from differences driven by yet unidentified cofactors which may differentially modulate the effect of PSME4 on proteasome activity. Interestingly, however, we show that PSME4 binds to the immunoproteasome and

attenuates all immunoproteasome-associated activities. In fact, PSME4 exerts opposite effects on the constitutive proteasome β1 and immunoproteasome β1i activities. We also observed that some of the PSMB10 protein bound to PSME4 is in the un-matured form. Intriguingly, blm10 in yeast, the homolog of PSME4, promotes proteasome maturation by preferentially binding the mature 20S (refs. 44,45). It remains to be seen whether and how PSME4 may be involved in promoting maturation of different proteasome species.

Third, we demonstrate that the PSME4-restricted proteasome activity also reduces the diversity of the MHC I-presented antigen landscape. PSME4 also drove increased degradation and presentation of nuclear antigens which have previously been shown to reduce tumor immunogenicity[46]. The increase in nuclear antigens might be another mechanism by which PSME4 modulates tumor–immune interactions. While the altered proteasome composition in NSCLC plays a detrimental role in reshaping the tumor microenvironment, as PSME4 does not have a known ubiquitin recognition domain similar to the 19S regulatory complex, it remains to be studied if the effect we see is ubiquitin-dependent or independent[47]. Indeed, previous studies provided mixed evidence as to which fractions of the peptides presented on MHC I are ubiquitin-dependent or even proteasome-restricted[48–53]. As such, PSME4 and other regulatory subunits of the proteasome (for example, PSME1-3) may represent an additional ubiquitin-independent route of degradation that modulates the presented peptidome. Furthermore, numerous studies have shown that there is no direct linear relationship between the abundance of proteins in the proteome and their degradation and subsequent presentation. For example, defective ribosomal products (DRiPs) were shown to be preferentially presented in many conditions[54] and peptides derived from the immunoproteasome were shown to be favorable for presentation[2,8,9,55]. Another example, presented in this study, is the enrichment of peptides from nuclear-associated proteins, which we hypothesize is the outcome of the upregulation of PSME4 which is known to be more abundant in the nucleus. Thus, proteasome complex heterogeneity may influence substrate degradation in different conditions and, in turn, shape the immunopeptidome landscape via the MHC I pathway. Further study is necessary to decipher the roles different components of the proteasome network may have in the processing and presentation of antigens and also as determinants of antigen selection[56,57], especially in a temporal and condition-specific manner.

Finally, our data suggest that PSME4 expression designates 'cold tumors' and limits response to immunotherapy. Importantly, PSME4 is one of the few markers of resistance to ICI, unlike other markers that indicate responsiveness, such as the immunoproteasome[10,11,58], TMB, infiltrate signatures and others. It is notable that we find that PSME4 plays a specific role in NSCLC, as previous studies have found NSCLC to be immunoproteasome-deficient[11,59], and it will be intriguing to determine whether these two hallmarks are connected. Due to the nonimmunogenic nature of the KP1.9 model, and the strong effect that depleting PSME4 has on tumor progression alone, further work will be required to define the potential of targeting PSME4, either by reducing its levels or by prohibiting its binding to proteasomes, for sensitization to immunotherapy. Additionally, the different responses of different NSCLC models and the wide range of potential therapies will have to be calibrated in preclinical studies. Because PSME4 and the immunoproteasome levels are tumor-type-specific, such approaches are expected to differ between cancer types. However, even with the heterogeneity of ICI responses in patients, we saw a strong relationship between PSME4 levels and ICI response across multiple cancer types. Collectively, our findings highlight a potential therapeutic targeting of PSME4 or its binding to proteasomes as an approach in treating NSCLC and in sensitizing response to ICI through combination therapy[60]. Further, it underscores the relevance and importance of considering the heterogeneity of the proteasome complex and its regulatory subunits in the context of precision immuno-oncology.

Methods

Statistics and reproducibility

All experiments were performed in three individual replicates unless otherwise mentioned. For each experiment, all compared conditions were analyzed by MS at the same time. For the NSCLC degradome analysis, nine samples from tumors and adjacent tissue were analyzed, and one was excluded for poor technical quality. The samples were processed independently and analyzed by MS at the same time to maintain comparability across samples and decrease batch effects. When representative images are shown, at least two independent experiments were performed with similar results. No statistical methods were used to predetermine sample sizes, but these were similar to previously published work with similar systems[30,61]. Data distribution was assumed to be normal, but this was not formally tested. No data were excluded from the analyses; the experiments were not randomized; and the investigators were not blinded to allocation during experiments and outcome assessment.

Purification of proteasome complexes

Lung adenocarcinoma tumors and adjacent tissues were mechanically disrupted and passed through a 70-µm cell strainer 93070 (SPL). Cells were lysed with 25 mM HEPES, pH 7.4, 10% glycerol, 5 mM $MgCl_2$, 1 mM ATP and 1:400 protease-inhibitor mixture (Calbiochem), then homogenized through freeze–thaw cycles and passed through a needle. The lysates were cleared by 30 min of centrifugation at 21,130*g* at 4 °C. Lysates were treated with 2 mM 1,10-phenanthroline (Sigma), crosslinked with 0.5 mM dithiobis succinimidyl propionate (Thermo Fisher Scientific) for 30 min at room temperature and quenched in 100 mM Tris-HCl, pH 8, and 5 mM L-cysteine for 10 min at room temperature. For immunoprecipitation, the lysates were then incubated with Protein G-Sepharose beads (Santa Cruz) with antibodies to PSMA1 and eluted with 100 mM Tris-HCl, pH 8, 8 M urea and 50 mM dithiothreitol for 30 min at 37 °C. Subsequently, 1% trifluoroacetic acid (TFA) was added. Aliquots of each elution fraction were analyzed by SDS–PAGE to evaluate yield and purity.

Purification and concentration of proteasome peptides

A critical step in our procedure is the separation of peptides from the proteins eluted in the proteasome pulldown. MAPP analyzes endogenously cleaved peptides, whereas the proteasome complex and associated proteins are physically excluded. Immunoprecipitated proteasomes and their encompassed peptides were loaded on C18 cartridges (Waters) which were prewashed with 80% acetonitrile in 0.1% TFA, then washed with 0.1% TFA only. After loading, the cartridges were washed with 0.1% TFA. Peptides were eluted with 30% acetonitrile in 0.1% TFA. Protein fractions were eluted with 80% acetonitrile in 0.1% TFA.

MS sample processing

Protein fraction after proteasome purification: Proteins were denatured by 8 M urea for 30 min at room temperature, reduced with 5 mM dithiothreitol (Sigma) for 1 h at room temperature and alkylated with 10 mM iodoacetamide (Sigma) in the dark for 45 min at room temperature. Samples were diluted to 2 M urea with 50 mM ammonium bicarbonate. Proteins were then subjected to digestion with trypsin (Promega) overnight at 37 °C at 50:1 protein to trypsin ratio, followed by a second trypsin digestion for 4 h. The digestions were stopped by addition of TFA (1% final concentration). Following digestion, peptides were desalted using Oasis HLB, µElution format (Waters). The samples were vacuum-dried and stored at −80 °C until further analysis.

Total proteomics: Lysates in 5% SDS in 50 mM Tris-HCl were incubated at 96 °C for 5 min, followed by six cycles of 30 s of sonication (Bioruptor Pico, Diagenode). Proteins were reduced with 5 mM dithiothreitol and alkylated with 10 mM iodoacetamide in the dark. Each sample was loaded onto S-Trap microcolumns (Protifi) according

to the manufacturer's instructions. In brief, after loading, samples were washed with 90%/10% methanol/50 mM ammonium bicarbonate. Samples were then digested with trypsin for 1.5 h at 47 °C. The digested peptides were eluted using 50 mM ammonium bicarbonate; trypsin was added to this fraction and incubated overnight at 37 °C. Two more elutions were made using 0.2% formic acid and 0.2% formic acid in 50% acetonitrile. The three elutions were pooled together and vacuum-centrifuged to dry. Samples were kept at −80 °C until analysis.

HLA immunopeptidomics was performed based on ref. 12. Cell-line pellets were collected in triplicate from 2×10^8 cells. For PSME4, OE cells were transfected 48 h before treatment and treated for 24 h with TNF-α/IFN-γ as described below. For PSME4, KD experiment cells were acid-stripped and treated for 6 h with TNF-α/IFN-γ as described below. PSME4 KD experiments were performed at the Smoler Proteomics Unit (Technion). Cell pellets were lysed on ice with a lysis buffer containing 0.25% sodium deoxycholate, 0.2 mM iodoacetamide, 1 mM EDTA, 1:200 Protease Inhibitor Cocktail (Sigma Aldrich), 1 mM PMSF and 1% octyl-b-D glucopyranoside in PBS. Samples were then incubated with rotation at 4 °C for 1 h. The lysates were cleared by centrifugation at 48,000*g* for 60 min at 4 °C and then passed through a preclearing column containing ProteinA Sepharose beads. HLA-I molecules were immunoaffinity purified from cleared lysate with the panHLA-I antibody (W6/32 antibody purified from HB95 hybridoma cells). Affinity columns were washed first with 400 mM NaCl, 20 mM Tris-HCl and then with 20 mM Tris-HCl pH 8.0. The HLA–peptide complexes were then eluted with 1% TFA followed by separation of the peptides from the proteins by binding the eluted fraction to Sep-Pak (Waters). Elution of the peptides was done with 28% acetonitrile in 0.1% TFA. The peptides were dried by vacuum centrifugation.

Liquid chromatography MS

Peptide fraction: ultra liquid chromatography–mass spectrometry grade solvents were used for all chromatographic steps. Each sample was loaded using split-less nano-Ultra Performance Liquid Chromatography (10 kpsi nanoAcquity; Waters). The mobile phase was: (1) H_2O + 0.1% formic acid, and (2) acetonitrile + 0.1% formic acid. Desalting of the samples was performed online using a reversed-phase Symmetry C18 trapping column (180-µm internal diameter, 20-mm length, 5-µm particle size; Waters). The peptides were then separated using a T3 HSS nano-column (75-µm internal diameter, 250-mm length, 1.8-µm particle size; Waters) at 0.35 µl min^{-1}. Peptides were eluted from the column into the mass spectrometer using the following gradient: 4% to 35% B in 120 min, 35% to 90% B in 5 min, maintained at 90% for 5 min and then back to initial conditions.

The nano ultra-performance liquid chromatography was coupled online through a nano electrospray ionization emitter (10-µm tip; New Objective) to a quadrupole orbitrap mass spectrometer (Q Exactive Plus, Thermo Scientific) using a FlexIon nanospray apparatus (Proxeon).

Data were acquired in data-dependent acquisition mode, using a Top10 method. MS1 resolution was set to 70,000 (at 400 *m/z*), mass range of 375–1,650 *m/z*, automatic gain control of 3×10^6 and maximum injection time was set to 100 ms. MS2 resolution was set to 17,500, quadrupole isolation 1.7 *m/z*, automatic gain control of 1×10^5, dynamic exclusion of 40 s and maximum injection time of 150 ms.

MS data analysis

Raw data were analyzed using MaxQuant software (v.1.6.0.16) with the default parameters for the analysis of the proteasomal peptides, except for the following: unspecific enzyme, label-free quantification minimum ratio count of 1, minimum peptide length for unspecific search of 6, maximum peptide length for unspecific search of 40 and match between runs enabled. A stringent false discovery rate (FDR) of 1% was applied for peptide identification. For the analysis of tryptic digests, the default parameters were set, apart from a minimum peptide length of 6. Masses were searched against the human proteome database from UniprotKB (last update September 2018).

Proteomics processing and label-free quantification

Peptides resulting from MaxQuant were initially filtered to remove reverse sequences and known MS contaminants. For the MAPP peptide fraction we removed antibody and proteasome peptides as contaminants. To decrease ambiguity, we allowed peptides that had at least two valid label-free quantification intensities out of the sample replicates, and we included razor peptides, which belong to a unique MaxQuant 'protein group'. MAPP protein intensities were inferred with MaxQuant. For graphical representation intensities were log-transformed, and in Python v.3.6, zero intensity was imputed to a random value chosen from a normal distribution of 0.3 s.d. and downshifted 1.8 s.d. For clinical cohorts, zero intensity was imputed to half the minimum. The presence of missing values reflects both technical and biological variation in the samples. In cases of matched samples, ratios were calculated per pair and paired *t*-tests were used. Otherwise, ratios were calculated based on the median of each group and a nonpaired Student's *t*-test was used. The protein fraction of the MAPP analysis was normalized to the mean of the core proteasome subunits (PSMA1-7 and PSMB1-4) to control for efficiency. For comparison of whole cell proteomics and MAPP data, proteins were ranked by their signed *P* value: the sign of the fold change between conditions multiplied by the negative $\log_{10}$-transformed *P* value. Proteins that had positive (tumor-increased) values were binned into ten groups of equal size. Any proteins that were detected in MAPP but not detected or defined as adjacent-associated in whole cell proteomics were termed not-detected. The proteins in MAPP or whole cell proteomics with the top 50 signed *P* values are presented in heatmaps in Fig. 1. For the PSME4 OE immunopeptidomics, which were collected and processed in pairs, values from a peptide that was not detected in a treatment pair were not included in the analysis. For the PSME4 KD immunopeptidomics, samples that did not meet quality control standards were removed from the analysis, leaving biological triplicates for both conditions. The binding of peptides was predicted by netMHC based on A549 haplotypes[9]. Any peptide with a binding rank greater than 5 was considered as a contaminant for analysis of the differentially presented peptides.

TCGA, CPTAC and immune checkpoint inhibitor data curation

TCGA data were mined using the xenaPython package in Python 3.6. The results shown in this analysis are in whole or part based upon data generated by the TCGA Research Network: http://cancergenome.nih.gov/. For the cross-cancer proteasome ratio the GDC pan-cancer dataset was used. Only cancer types with ten or more normal controls were used. Ratios presented are the differences between the means of the normal and tumor groups. Data used in this publication were generated by CPTAC (National Cancer Institute/National Institutes of Health). The CPTAC-LUAD cohort ($n = 110$ tumors with matched adjacents) was used. In cases where ratios between the adjacent and tumor samples are presented, only those samples with matching controls are used. Otherwise, all the tumor and normal (adjacent control) samples were utilized. Data reprocessing of six cohorts of ICI-treated patients across three cancer types was performed[10,30,62–66]. The signatures were confirmed in an independent cohort of NSCLC[31]. Proteasome subunit expression was normalized to the core proteasome subunits (PSMA1-7 and PSMB1-4) for each sample.

Proteasome complex heterogeneity clustering

The TCGA and ICI cohorts listed were combined by normalizing and scaling the expression values for each cohort set (PANCAN, ICI1000+ and NSCLC cohorts) and then normalizing to the core proteasome. For the clustering, either the catalytic core expression (PSMB5-10) or the regulatory cap expression (PSME1-4) was used. The data were clustered using *K*-means (catalytic core) or Partitioning Around Medoids (PAM;

regulatory caps) using the defaults in R. Clusters were then defined by the dominant proteasome type expressed in the cluster.

Immune checkpoint inhibitor response analysis

To avoid data pooling, a meta-statistics approach was adapted from ref. 30 and patients were stratified by the expression of different subunits (50% highest and lowest expressers across the cohorts) and then correlated with ICI response. Likewise, to confirm the independence of different biomarkers a general linear regression model was used. The model was first generated for 35 biomarkers and then iteratively reduced to only the markers that significantly contributed to the classification. For the survival analysis in Fig. 1, only the cohorts that included patient survival information (melanoma and bladder) were utilized.

Signatures and data visualization

Statistical analyses were performed in R v.3.6.2 and GraphPad Prism v.7.04. In R, data were visualized using the complexheatmap[67] and ggplot[68] packages. Defaults were used unless otherwise noted. Protein annotation and gene ontology analysis were performed with the gene-set enrichment analysis[69] using the annotation sets indicated in the figures. The T cell inflammation signature was based on Trujillo et al.[70] and Spranger et al.[71]. Protein subcellular localization was extracted from the Human Protein Atlas[72–74] with 'uncertain' or 'approved' localization reliabilities excluded.

Reagents

A549 cells were originally obtained from ATCC (CCl-185), grown in DMEM and used as model systems for cell biology studies including western blot, biochemistry and imaging. KP1.9 cells, kindly provided by Alfred Zippelius, were grown in Iscove's MDM. Cells were routinely tested for mycoplasma contamination. Media were supplemented with 10% FBS, 1% penicillin/streptomycin and L-glutamine (2 mmol l^{-1}) (Biological industries), unless otherwise indicated, at 37 °C with 5% CO_2.

For TNF-α/IFN-γ activation, cells were allowed to seed overnight and were subsequently treated with TNF-α (PeproTech, human; 300-01A or mouse; 315-01A) and IFN-γ (PeproTech, human; 300-02 or mouse; 315-05) at 20 ng ml^{-1} and 10 ng ml^{-1}, respectively, for 24 h.

Cell death assessment was done by trypan blue staining, with cell counting by a Countess II automated cell counter (Thermo Fisher) and by Cell titerGlo assay (Promega). Proliferation of mammalian cells was measured by KIT8 assay (Sigma).

MISSION short hairpin RNAs targeting mouse or human PSME4 or RFP were obtained from Sigma (TRCN0000176569, TRCN0000178428, TRCN0000158223, TRCN0000157073).

pcDNA3.1_PSME4 (ref. 75) was transfected into A549/KP1.9 cells with Lipofectamine 2000 (Thermo Fisher).

Antibodies used are listed in Supplementary Table 1.

Proteasome cleavage reporter assay

Cells were lysed with 25 mM HEPES, pH 7.4, 10% glycerol, 5 mM $MgCl_2$, 1 mM ATP and 1:400 protease-inhibitor mixture (Calbiochem), then homogenized through freeze–thaw cycles and passed through a needle. The lysates were cleared by 30 min of centrifugation at 21,130*g* at 4 °C to remove cell debris. Protein concentration of the supernatant was determined by a NanoDrop spectrophotometer (Thermo Fisher Scientific) by measuring the absorbance at 280 nm.

Proteasomal activity in cell fractions was determined by cleavage of the fluorogenic precursor substrates Suc-Leu-Leu-Val-Tyr-AMC (Suc-LLVY-AMC), Ac-Pro-Ala-Leu-AMC (Ac-PAL-AMC), Z-Leu-Leu-Glu-AMC (Z-LLE-AMC), Ac-Arg-Leu-Arg-AMC (Ac-RLR-AMC), Ac-Ala-Asn-Trp-AMC (Ac-ANW-AMC) (Boston Biochem), Z-Leu-Leu-Glu-βNA (Z-LLE-βNA) and Ac-Nle-Pro-Nle-Asp-AMC (Ac-nLPnLD-AMC) (Bachem). Substrate (10 μM) was added to 10 μg of total protein per well, and incubated in a reaction buffer (50 mM HEPES, pH 7.5, 1 mM dithiothreitol, 5 mM $MgCl_2$ and 2 mM ATP). When using recombinant PSME4 (purified according to ref. 18), 1 nM was added to a 100-μl final reaction. Fluorescence increase resulting from degradation of peptide-AMC at 37 °C was monitored over time by means of a fluorometer (Synergy H1 Hybrid Multi-Mode Microplate Reader, BioTek) at 340-nm excitation and at 460-nm emission, using the proteasome inhibitor MG132 (Calbiochem) as background. Resulting product curves were followed for up to 3.5 h. Each value of fluorescence intensity represents a mean value obtained from three independent experiments.

Immunoblotting

Cells were lysed in STET buffer (50 mM Tris-HCl, pH 7.5, 150 mM NaCl, 2 mM EDTA 1% Triton-X and 1:400 protease-inhibitor mixture (Calbiochem)). Protein concentration was assessed using a BC Assay Protein Quantitation Kit (Interchim). First, 20 μg of total protein was separated by SDS–PAGE on a 4–20% gradient ExpressPlus PAGE gel (M42015, https://www.ncbi.nlm.nih.gov/nuccore/M42015 GenScript) and transferred onto PVDF membranes using an iBlot 2 Gel Transfer Device (Thermo Fisher Scientific). The membranes were blocked in 5% milk prepared in TBS–0.1% Tween and incubated in primary antibodies overnight at 4 °C, followed by washing and incubation with secondary antibody. Blots were developed using the ChemiDoc XRS+ Imaging System (Bio-Rad) and band intensities were quantified with ImageJ analyzer software.

Immunoprecipitation

Cells were lysed in 25 mM HEPES, pH 7.4, 10% glycerol, 5 mM $MgCl_2$, 1 mM ATP and 1:400 protease-inhibitor mixture (Calbiochem), then homogenized through freeze–thaw cycles and passed through a needle. The lysates were cleared by 30 min of centrifugation at 21,130*g* at 4 °C to remove cell debris. Precleared cell lysates were prepared by incubating with ProteinA/G-conjugated agarose beads for 30 min at 4 °C with slow rotation. Then, 1 mg of precleared cell lysates were added to 20 μl of fresh ProteinA/G-conjugated agarose beads along with 4 μg of antibodies. The mixture was incubated overnight at 4 °C with slow rotation followed by three 1-ml washes with chilled PBS buffer. The target conjugates were then eluted from beads by mixing protein loading dye (with reducing agents) and heating for 5 min at 95 °C followed by denaturing western blot.

Nucleus and cytoplasm fractionation

All preparations were performed on ice. Cells were lysed in 20 mM HEPES, pH 7.4, 10 mM KCl, 5 mM $MgCl_2$, 1 mM ATP and 1:400 protease-inhibitor mixture (Calbiochem), then passed through a needle. The solution was centrifuged to pellet nuclei (700*g* 5 min). Supernatant (cytoplasmic fraction) was re-centrifuged (15,000*g*, 3 min) to pellet debris. The nuclei fraction was washed three times with cell lysis buffer. Nuclei were lysed and protein concentrations of each fraction were assessed using BC Assay Protein Quantitation Kit (Interchim).

Gel filtration

Gel filtration experiments were performed using a Superose 6 Increase 10/300 GL size exclusion column (GE Healthcare) ÄKTA pure protein purification system (Cytiva). The running buffer used was 25 mM HEPES, pH 7.4, 10% glycerol, 5 mM $MgCl_2$ and 1 mM ATP. The column was calibrated using a gel filtration molecular weight standard (Bio-Rad). The following standards were used for calibration: thyroglobulin (670 kDa, stokes radius (Rs) = 8.6 nm), γ-globulin (158 kDa, Rs = 5.1 nm), ovalbumin (44 kDa, Rs = 2.8 nm), myoglobin (17 kDa, Rs = 1.9 nm), vitamin B12 (1.35 kDa) and dextran blue (2 MDa).

A 0.1-ml protein sample at a final concentration of 0.4 mg ml^{-1} was filtered and chromatographically analyzed using a flow rate of 0.5 ml min^{-1}. Absorbance was monitored at 280 nm, and elution volumes were determined from ultraviolet chromatogram. The partition coefficient, K_{av}, was calculated from the elution volume of the sample, V_e, and total bed volume, V_t, using the expression:

$K_{av} = (V_e - V_0)/(V_t - V_0)$. Calibration curves and equations were established.

Peptide stripping by acid wash

To remove HLA-bound peptides from the cell surface, cells were washed twice with PBS and then incubated for 1 min with citrate phosphate buffer (260 mM citric acid and 123 mM disodium phosphate (pH 3)) at room temperature. Afterwards, cells were washed twice with their relevant medium, supplemented with 10% FBS, 2 mM glutamine and 1 mM sodium pyruvate. Subsequently, cells were resuspended in fresh medium and plated in six-well plates.

Surface HLA staining in flow cytometry

A549 and KP1.9 cells, after acid strip, were treated with hTNF-α/hIFN-γ (as described above) or mTNF-α/mIFN-γ (as described above), respectively, for 24 h or as indicated. Cells were collected and stained with Live/Dead Aqua staining kit from BioLegend as per the manufacturer's protocol. Approximately 1×10^6 cells were washed, blocked with 2% FCS for 5 min and stained with anti-HLA-A/B/C-PE (A549) or anti-MHCI-Kb-PE/MHCI-Db-FITC (KP1.9) in 100 µl for 30 min. Cells were then washed and acquired.

Intracellular HLA staining

Cells were collected and stained with Live/Dead Aqua staining kit from BioLegend as per the manufacturer's protocol. Approximately 1×10^6 cells were washed, fixed in ice-cold 3.7% PFA in PBS for 10 min, blocked with 2% FCS for 5 min and stained with anti-HLA-A/B/C-PE.

Tissue fixation, processing and embedding

Tissues were fixed in 4% paraformaldehyde for 1 week. Dehydration of the tissue was done by serial immersion in increasing concentrations of alcohol (70% to 100%) and removal of the dehydrant with xylene. The tissue was embedded in paraffin, sectioned at 4 µm and mounted on microscope slides. The slides were placed in an oven for 1 h at 60 °C or overnight at 37 °C before immunohistochemical staining.

IHC and immunofluorescence staining

Hematoxylin and eosin stains were performed on an automated device according to the manufacturer's instructions. IHC stains were performed on a Benchmark XT staining module (Ventana Medical Systems) using iVIEW DAB Detection Kit (760-091, Ventana Medical Systems) or Ultra VIEW Universal DAB Detection Kit (760-500, Ventana Medical Systems). Antibody details are described above. Following immunostaining, sections were counterstained with hematoxylin (Ventana Medical Systems), rinsed in distilled water and dehydrated manually in graded ethanols. Finally, the sections were cleared in xylene and mounted with Entellan (Surgipath Medical Industries) on glass slides.

The immunofluorescence staining was performed at the Molecular Cytology Core Facility of Memorial Sloan Kettering Cancer Center using a Discovery XT processor (Ventana Medical Systems). Sections were stained with antibodies for CD31 (endothelial cell marker), CD3 (T cells), CD8 (T cells) and FoxP3 (Tregs). Scanning of slides was done by PANNORAMIC SCAN II (3DHISTECH).

IHC staining of PSME4

Paraffin-embedded mouse and human tissues were cut in 3-µm-thick sections using the Hyrax M55 microtome (Zeiss). Tissue sections were incubated for 1 h at 60 °C to melt paraffin, deparaffinized by incubating twice in xylene for 5 min and rehydrated in a descending alcohol series (100%, 90%, 80% and 70% (v/v)) for 1 min. To block endogenous protease activity and to permeabilize sections for nuclear staining, they were incubated in a methanol/hydrogen peroxide (80%/1.8% (v/v)) solution for 20 min. Tissue sections were rinsed in Milli-Q water and heat-induced antigen retrieval was performed in citrate buffer pH 6 using a decloaking chamber (Biocare Medical). After washing with Tris-buffered saline with 0.1% Tween 20 (TBST), unspecific binding sites were blocked for 30 min with Rodent Block M (Biocare Medical). The slides were washed again in TBST and incubated with anti-PSME4 antibody (sc-135512, Santa Cruz) diluted in Antibody Diluent (DAKO) for 1 h at room temperature. After extensive washing in TBST, sections were incubated with MACH 2 Rabbit AP-Polymer (Biocare Medical) for 30 min at room temperature. Sections were rinsed again in TBST and incubated in Vulcan Fast Red AP substrate solution (Biocare Medical) for 10 min. Tissue sections were washed in TBST and Milli-Q water and hematoxylin counterstaining (Carl Roth) was performed to visualize nuclei. After repeated washing in TBST, sections were dehydrated in ethanol and xylene and mounted using Entellan mounting medium (Merck Millipore). Slides were imaged using the MIRAX scanning system (Zeiss).

Stainings were analyzed by an expert clinical pathologist blinded to the sample identity. Tumor staging was done based on the criteria from Klotz et al.[76]. Semiquantitative scores for PSME4 expression were obtained by defining the percentage of PSME4-positively stained tumor areas multiplied by the intensity of staining as graded between 1 (weak) and 3 (strong). Scores were dichotomized into high- (>80) and low- (<80) expressing tumors with the score 80 representing the median of all samples.

Quantitative PCR analysis

RNA was extracted using Direct-zol RNA MiniPrep R2051 (ZYMO research). Messenger RNA levels were ascertained by RT using High-Capacity cDNA Reverse Transcription Kit (Thermo Fisher), real-time quantitative PCR using Sybr-green (Kapa Biosystems) and the StepOnePlus Real-Time PCR Systems (Life Technologies), using primers listed in Supplementary Table 2.

All values were normalized to the mRNA abundance of housekeeping genes (RPS18 or GAPDH in human; GAPDH in mouse). Each primer pair was calibrated using the Absolute Quantification program with increasing concentrations of complementary DNA.

Orthotopic lung cancer model

Mouse experiments were conducted according to approved experimental procedures (approval numbers 04400520-2 and 04990620-1). Male C57Bl/6J mice (Envigo) or RAG1−/− mice (Jackson Laboratory) at the age of 8–10 weeks were injected intravenously with 2×10^5 cells in 200 µl of PBS (Biological Industries). Mice were observed for adverse effects and weights noted twice a week. Peripheral blood was collected from the tail vein. At the end of the experiment, mice were killed by CO_2 asphyxiation and tissues collected to cold PBS. Mice were housed in individually ventilated cages, with up to five animals per cage, with 12 h dark/12 h light cycle, with an average room temperature of 21 °C and humidity around 50%. Only male mice were used in our in vivo studies, as the KP1.9 cells were initially isolated from a male C57BL/6 KrasLSL-G12D/WT;p53Flox/Flox mouse. Female mice rejected engraftment.

Tissue processing and flow cytometry staining

Peripheral blood was washed and red blood cells removed by ACK lysis buffer (150 mM NH_4Cl, 10 mM $KHCO_3$, 0.1 mM EDTA in 0.1 × PBS−/−) and washed in flow cytometry buffer (PBS−/−, 0.5% BSA, 2 mM EDTA).

Spleens and lungs were weighed before further processing. The left lung lobe was used for histological analysis of tumor development (hematoxylin and eosin) after fixation in 4% formaldehyde (Biolabs). Right lung lobes were minced and digested with 5 ml of digestion buffer: collagenase 4 (200 U ml^{-1}, Worthington Biochemicals), DNase I (100 µg ml^{-1}, Sigma Aldrich) in PBS++ supplemented with 2 mM $CaCl_2$, for 20 min at 37 °C with shaking. Single-cell suspensions of spleen and lungs were obtained by straining cells through 100-µm strainers and washing in cold flow cytometry buffer. Red blood cells were removed by ACK lysis buffer, washed with flow cytometry buffer and strained again.

For intracellular cytokine and transcription factor stainings, cells were incubated for 4 h with Brefeldin A (Biolegend) and Monensin (Sigma Aldrich). First, viability staining was done with Zombie Aqua (Biolegend) according to the protocols. Cell surface staining was performed in flow cytometry buffer in 100 µl at appropriate dilutions. When needed, cells were fixed and permeabilized with the FoxP3 transcription factor kit from eBioscience (Thermo Fisher Scientific) and stained for FoxP3 and IFNg according to the manufacturer's protocol. Samples were acquired on an Attune Nxt with Autosampler and analyzed in FlowJo (v.10.7.1, Becton Dickinson). Exemplary gating strategies are provided in Supplementary Information.

Cytotoxicity assay

In total, 10,000 KP1.9 wild-type (WT) cells were stained with CFSE (5 µM; BioLegend; at a cell concentration of 1×10^6 per ml), plated onto a 96-well plate and allowed to attach overnight. The following day, splenocytes were isolated from naive mice, or from mice bearing KP1.9-WT, -PSME4 KD or -PSME4 OE tumors. Red blood cells were lysed using ACK buffer, cells were washed in PBS and 100,000 splenocytes were plated on top of the tumor cells in RPMI medium + beta-mercaptoethanol (50 µM). Coculture was maintained for 7 days. On day 7, cell supernatants were collected onto a new 96-well plate, and the attached tumor cells were detached with trypsin containing propidium iodide. After cell detachment, the supernatant was used to resuspend the detached cells, and the entire sample was acquired.

Bulk RNA-seq library preparation and analysis

Total RNA was extracted from A549 cells using Trizol (Ambion) and chloroform, followed by washes with isopropanol and 70% ethanol. Next, 1 µg of extracted RNA was used as an input for mRNA isolation using polyA beads (Lexogen's SENSETM mRNA-Seq Kit V2). Then, libraries were prepared using the same kit, according to the manufacturer's instructions. The libraries were sequenced using the Illumina Next Generation Sequencing platform.

Analysis of RNA-seq data was carried out in User-friendly Transcriptome Analysis Pipeline (UTAP) v.1.10 (ref. 77). In short, reads were trimmed using the Cutadapt function. Reads were then mapped to the mouse genome hg38 using the Spliced Transcripts Alignment to a Reference (STAR) method, followed by quantification with RefSeq annotated genes. Counting was performed using STAR. Subsequently, the analysis was carried out for genes that had at least five reads in at least one sample. Normalization of the counts was done using DESeq2 with the parameters: betaPrior = True, cooksCutoff = FALSE, independentFiltering = FALSE. Raw *P* values were adjusted for multiple testing using the Benjamini and Hochberg method. The adjusted *P* values were corrected with FDR tools with the normal null model used for statistics. This pipeline was built using Snakemake.

scRNA-seq of CD45$^+$ cells from lung tissues

CD45$^+$ cell isolation from lung tissues. C57Bl/6J mice were injected with KP1.9 shCtrl or shPSME4 cells (0.25×10^6 cells, intravenously). After 21 days, lungs were perfused manually with 3 ml of cold PBS without Mg/Ca through the right ventricle of the heart and collected (4 × shCtrl, 4 × shPSME4) into cold PBS. The lung tissue was cut into pieces and processed using a GentleMACS Octo Dissociator (program 37C_m_LDK_1, Miltenyi Biotec) with the mouse lung dissociation kit (130-095-927, Miltenyi Biotec) according to the manufacturer's protocol. After the run, cells were strained through a 70-µm mesh and washed with FACS buffer (0.5% BSA, 2 mM EDTA in PBS without Mg/Ca). Red blood cells were lysed with ACK buffer for 4 min, and the reaction stopped by addition of cold FACS buffer. Finally, cells were resuspended in FACS buffer with FC block (anti-CD16/CD32, 1:500, Biolegend 101330) and incubated for 5 min. Lung cells from shCtrl or shPSME4 were stained with four differently labeled CD45 antibodies (APC, PE/Cy7, FITC, violetFluor 450) for 30 min at 4 °C. Cells were washed with FACS buffer twice, and the shCtrl or shPSME4 samples unified for parallel sorting of the four lung populations. Propidium iodide was added fresh (1 µg ml^{-1}) to exclude dead cells, and cells were sorted on BD FACSAria III and BD SORP FACSAria II sorters running on BD FACSDiva software (v.8.0.1) using a 85-µm nozzle. A gating strategy is provided in Supplementary Fig. 19. Finally, cells were washed twice (PBS without Mg/Ca, 0.04% BSA) and counted on a Neubauer chamber with trypan blue, and three samples from each condition were chosen (high cell count and viability >90%) for further processing.

scRNA-seq using Chromium 10x genomics platform. scRNA-seq libraries were prepared at the Crown Genomics Institute of the Nancy and Stephen Grand Israel National Center for Personalized Medicine, Weizmann Institute of Science. Cells were counted and diluted to a final concentration of approximately 1,000 cells per µl in PBS supplemented with 0.04% BSA. The cellular suspension was loaded onto a Next GEM Chip K targeting 6,000 cells and then run on a Chromium Controller instrument to generate a GEM emulsion (10x Genomics). Single-cell gene expression libraries as well as single-cell V(D)J libraries were generated according to the manufacturer's protocol using the Chromium Next GEM Single Cell 5′ Reagent Kits v2 (Dual Index) workflow. Final libraries were quantified using NEBNext Library Quant Kit for Illumina (NEB) and high-sensitivity D1000 TapeStation (Agilent). Libraries were pooled according to targeted cell number, aiming for at least 5,000 reads per cell for V(D)J libraries and 20,000 reads per cell for gene expression libraries. Pooled libraries were sequenced on a NovaSeq 6000 instrument using an SP 200 cycles reagent kit (Illumina).

Raw reads processing. Raw sequencing bcl files were converted to fastq files and aligned to the GRCm38 mouse genome, and unique molecular identifiers were quantified using Cell Ranger suite (v.6.0.0). V(D)J libraries were mapped to the GRCm38 VDJ reference provided by 10x Genomics (v.5.0.0), and clones were identified, counted and summarized with Cell Ranger suite (v.6.0.0). Filtered count matrices were imported into R for further processing.

Clustering and cell-type identification. In gene expression libraries, low-quality cells with more than 10% of reads mapping to the mitochondrial genome were removed. The Seurat R package (v.4.0.3) was used to normalize and scale expression values for total unique molecular identifier counts per cell[78]. Due to complexity and variability in the immune cell population we performed stepwise clustering[79]. A detailed clustering strategy is shown in the supplementary single-cell documentation. First, 2,000 highly variable genes were identified using the vst method. Dimensionality reduction was done with principal component analysis, with the first 30 principal components used for nearest neighbor graph construction and clustering. For each cluster, based on marker expression, we identified whether it belonged to one of the groups: nonimmune, B cells, T cells, innate lymphoid cells, macrophages and DCs, cycling cells and other. Subsequently, we performed clustering within each group individually as described above; for each cluster we identified markers (Seurat FindMarkers function) and we removed clusters containing doublets, that is, clusters that did not have any uniquely expressed genes and contained markers specific for at least two abundant clusters. For example, clusters with high expression of Ncr1 (NK cell marker) and Cd79b (B cell marker) were considered doublets.

Finally, for each cluster we identified markers (Seurat FindMarkers function) and annotated them through comparison with markers in the literature and ImmGen database[80,81]

Functional analysis of cell populations. Gene ontology analysis was performed using g:Profiler2 (ref. 82) with default settings, and multiple hypothesis testing adjustment using all mouse genes as background control. The $\log_{10}$ FDR-adjusted *P* values were plotted as bar plots.

Differential expression analysis. To compare gene expression of each cell-type cluster between conditions, we calculated pseudo-bulk by adding reads from all cells within each cluster in a sample. We then used DESeq2 with default parameters to determine differential expression[83].

Ethics statement

Human lung tissues obtained from patients surgically treated for lung cancer were provided by the Asklepios Biobank for Lung Disease, Gauting, Germany or obtained from the Israel National Biobank for Research. Samples were obtained under the approval of the Ministry of Health Institutional Review Board, the Israel National Biobank for Research, protocol no. 118-2018, or the ethics committee of the Ludwig-Maximilians University Munich, according to national and international guidelines (project number 333-10). As tumors were in the lung and not subcutaneous, tumor burden was monitored through proxies of weight loss and breathing. Early withdrawal criteria for mouse experiments were either weight loss of more than 20% body weight or laborious/heavy breathing due to lung tumor expansion. Mice were removed from the study by reaching either criterion.

Reporting summary

Further information on research design is available in the Nature Portfolio Reporting Summary linked to this article.

Data availability

RNA-seq data that support the findings of this study have been deposited in the Gene Expression Omnibus (GEO) under accession code GSE201460. scRNA-seq data have been deposited to the ArrayExpress database at EMBL-EBI (www.ebi.ac.uk/arrayexpress) under accession code E-MTAB-10745. Mass spectrometry data (list in Supplementary Table 3) have been deposited to the ProteomeXchange Consortium via the PRIDE[84] partner repository with the primary accession codes PXD019573, PXD028364 and PXD037365 (https://www.ebi.ac.uk/pride/). Previously published data from ICB-treated cohorts that were re-analyzed here are available under accession codes EGAS00001002556, EGAS00001002928, GSE78220 and GSE91061. Human PANCAN transcriptomics data were derived from the TCGA Research Network: http://cancergenome.nih.gov/, and CPTAC: https://proteomics.cancer.gov/data-portal. Source data are provided with this paper. All other data supporting the findings of this study are available from the corresponding authors on reasonable request.

Code availability

Custom code used in this manuscript is available at https://github.com/merbllab/PSME4_NatCancer.

References

1. Johnson, D. B., Nebhan, C. A., Moslehi, J. J. & Balko, J. M. Immune-checkpoint inhibitors: long-term implications of toxicity. *Nat. Rev. Clin. Oncol.* **19**, 254–267 (2022).
2. Rock, K. L., Reits, E. & Neefjes, J. Present yourself! By MHC class I and MHC class II molecules. *Trends Immunol.* **37**, 724–737 (2016).
3. Rousseau, A. & Bertolotti, A. Regulation of proteasome assembly and activity in health and disease. *Nat. Rev. Mol. Cell Biol.* **19**, 697–712 (2018).
4. Salzmann, U. et al. Mutational analysis of subunit iβ2 (MECL-1) demonstrates conservation of cleavage specificity between yeast and mammalian proteasomes. *FEBS Lett.* **454**, 11–15 (1999).
5. Driscoll, J., Brown, M. G., Finley, D. & Monaco, J. J. MHC-linked LMP gene products specifically alter peptidase activities of the proteasome. *Nature* **365**, 262–264 (1993).
6. Gaczynska, M., Rock, K. L. & Goldberg, A. L. γ-Interferon and expression of MHC genes regulate peptide hydrolysis by proteasomes. *Nature* **365**, 264–267 (1993).
7. Winter, M. B. et al. Immunoproteasome functions explained by divergence in cleavage specificity and regulation. *eLife* **6**, e27364 (2017).
8. Chong, C. et al. High-throughput and sensitive immunopeptidomics platform reveals profound interferonγ-mediated remodeling of the human leukocyte antigen (HLA) ligandome. *Mol. Cell. Proteomics* **17**, 533–548 (2018).
9. Javitt, A. et al. Pro-inflammatory cytokines alter the immunopeptidome landscape by modulation of HLA-B expression. *Front. Immunol.* **10**, 141 (2019).
10. Riaz, N. et al. Tumor and microenvironment evolution during immunotherapy with nivolumab. *Cell* **171**, 934–949.e16 (2017).
11. Tripathi, S. C. et al. Immunoproteasome deficiency is a feature of non-small cell lung cancer with a mesenchymal phenotype and is associated with a poor outcome. *Proc. Natl Acad. Sci. USA* **113**, E1555–E1564 (2016).
12. Kalaora, S. et al. Immunoproteasome expression is associated with better prognosis and response to checkpoint therapies in melanoma. *Nat. Commun.* **11**, 896 (2020).
13. Blickwedehl, J. et al. The proteasome activator PA200 regulates tumor cell responsiveness to glutamine and resistance to ionizing radiation. *Mol. Cancer Res.* **10**, 937–944 (2012).
14. Ustrell, V., Hoffman, L., Pratt, G. & Rechsteiner, M. Pa200, a nuclear proteasome activator involved in DNA repair. *EMBO J.* **21**, 3516–3525 (2002).
15. Welk, V. et al. Inhibition of proteasome activity induces formation of alternative proteasome complexes. *J. Biol. Chem.* **291**, 13147–13159 (2016).
16. Qian, M.-X. et al. Acetylation-mediated proteasomal degradation of core histones during DNA repair and spermatogenesis. *Cell* **153**, 1012–1024 (2013).
17. Fabre, B. et al. Label-free quantitative proteomics reveals the dynamics of proteasome complexes composition and stoichiometry in a wide range of human cell lines. *J. Proteome Res.* **13**, 3027–3037 (2014).
18. Toste Rêgo, A. & da Fonseca, P. C. A. Characterization of fully recombinant human 20S and 20S-PA200 proteasome complexes. *Mol. Cell* **76**, 138–147.e5 (2019).
19. Tsvetkov, P. et al. Suppression of 19S proteasome subunits marks emergence of an altered cell state in diverse cancers. *Proc. Natl Acad. Sci. USA* **114**, 382–387 (2017).
20. Tanahashi, N. et al. Molecular properties of the proteasome activator PA28 family proteins and γ-interferon regulation. *Genes Cells* **2**, 195–211 (1997).
21. Sánchez-Martín, D. et al. Proteasome activator complex PA28 identified as an accessible target in prostate cancer by in vivo selection of human antibodies. *Proc. Natl Acad. Sci. USA* **110**, 13791–13796 (2013).
22. Kisselev, A. F. F., Akopian, T. N. N., Woo, K. M. M. & Goldberg, A. L. L. The sizes of peptides generated from protein by mammalian 26 and 20 S proteasomes. Implications for understanding the degradative mechanism and antigen presentation. *J. Biol. Chem.* **274**, 3363–3371 (1999).
23. Ruschak, A. M. & Kay, L. E. Proteasome allostery as a population shift between interchanging conformers. *Proc. Natl Acad. Sci. USA* **109**, E3454–E3462 (2012).
24. Yamano, T. et al. Allele-selective effect of PA28 in MHC class I antigen processing. *J. Immunol.* **181**, 1655–1664 (2008).
25. de Graaf, N. et al. PA28 and the proteasome immunosubunits play a central and independent role in the production of MHC class I-binding peptides in vivo. *Eur. J. Immunol.* **41**, 926–935 (2011).
26. Murata, S., Takahama, Y., Kasahara, M. & Tanaka, K. The immunoproteasome and thymoproteasome: functions, evolution and human disease. *Nat. Immunol.* **19**, 923–931 (2018).

27. Dick, T. P. et al. Coordinated dual cleavages induced by the proteasome regulator PA28 lead to dominant MHC ligands. *Cell* **86**, 253–262 (1996).
28. Wolf-Levy, H. et al. Revealing the cellular degradome by mass spectrometry analysis of proteasome-cleaved peptides. *Nat. Biotechnol.* **36**, 1110–1116 (2018).
29. Javitt, A. & Merbl, Y. Global views of proteasome-mediated degradation by mass spectrometry. *Expert Rev. Proteomics* https://doi.org/10.1080/14789450.2019.1651979 (2019).
30. Litchfield, K. et al. Meta-analysis of tumor- and T cell-intrinsic mechanisms of sensitization to checkpoint inhibition. *Cell* **184**, 596–614.e14 (2021).
31. Kim, J. Y., Choi, J. K. & Jung, H. Genome-wide methylation patterns predict clinical benefit of immunotherapy in lung cancer. *Clin. Epigenetics* **12**, 1–10 (2020).
32. Gillette, M. A. et al. Proteogenomic characterization reveals therapeutic vulnerabilities in lung adenocarcinoma. *Cell* **182**, 200–225.e35 (2020).
33. Kahana, C. & Reiss, Y. Cell-free assay for ubiquitin-independent proteasomal protein degradation. *Methods Mol. Biol.* **301**, 83–96 (2005).
34. Pishesha, N., Harmand, T. J. & Ploegh, H. L. A guide to antigen processing and presentation. *Nat. Rev. Immunol.* **22**, 751–764 (2022).
35. Lavin, Y., Kobayashi, S., Leader, A. & Rahman, A. Innate immune landscape in early lung adenocarcinoma by paired single-cell analyses. *Cell* **169**, 750–757.e15 (2017).
36. Maier, B. et al. A conserved dendritic-cell regulatory program limits antitumour immunity. *Nature* **580**, 257–262 (2020).
37. Li, S., Wu, J., Zhu, S., Liu, Y. J. & Chen, J. Disease-associated plasmacytoid dendritic cells. *Front. Immunol.* https://doi.org/10.3389/fimmu.2017.01268 (2017).
38. Morozov, A. V. & Karpov, V. L. Proteasomes and several aspects of their heterogeneity relevant to cancer. *Front. Oncol.* **9**, 761 (2019).
39. Cantin, A. M. & Richter, M. V. Cigarette smoke-induced proteostasis imbalance in obstructive lung diseases. *Curr. Mol. Med.* **12**, 836–849 (2012).
40. Kammerl, I. E. et al. Dissecting the molecular effects of cigarette smoke on proteasome function. *J. Proteomics* **193**, 1–9 (2019).
41. Srinivas, U. S., Tan, B. W. Q., Vellayappan, B. A. & Jeyasekharan, A. D. ROS and the DNA damage response in cancer. *Redox Biol.* https://doi.org/10.1016/j.redox.2018.101084 (2019).
42. Young, J. H. et al. Computational discovery of pathway-level genetic vulnerabilities in non-small-cell lung cancer. *Bioinformatics* **32**, 1373–1379 (2016).
43. Jiang, T.-X. et al. Proteasome activator PA200 maintains stability of histone marks during transcription and aging. *Theranostics* **11**, 1458 (2021).
44. Wani, P. S., Rowland, M. A., Ondracek, A., Deeds, E. J. & Roelofs, J. Maturation of the proteasome core particle induces an affinity switch that controls regulatory particle association. *Nat. Commun.* **6**, 6384 (2015).
45. Marques, A. J., Glanemann, C., Ramos, P. C. & Dohmen, R. J. The C-terminal extension of the β7 subunit and activator complexes stabilize nascent 20 S proteasomes and promote their maturation. *J. Biol. Chem.* **282**, 34869–34876 (2007).
46. Boulpicante, M. et al. Tumors escape immunosurveillance by overexpressing the proteasome activator PSME3. *Oncoimmunology* **9**, 1761205 (2020).
47. Sahu, I. & Glickman, M. H. Structural insights into substrate recognition and processing by the 20S proteasome. *Biomolecules* **11**, 1–15 (2021).
48. Huang, L., Marvin, J. M., Tatsis, N. & Eisenlohr, L. C. Cutting edge: selective role of ubiquitin in MHC class I antigen presentation. *J. Immunol.* **186**, 1904–1908 (2011).
49. Wei, J. et al. Varied role of ubiquitylation in generating MHC class I peptide ligands. *J. Immunol.* **198**, 3835 (2017).
50. Abi Habib, J., Lesenfants, J., Vigneron, N. & Van den Eynde, B. J. Functional differences between proteasome subtypes. *Cells* **11**, 421 (2022).
51. van Endert, P. Intracellular recycling and cross-presentation by MHC class I molecules. *Immunol. Rev.* **272**, 80–96 (2016).
52. Buneeva, O. A. & Medvedev, A. E. Ubiquitin-independent degradation of proteins in proteasomes. *Biochem. (Mosc.) Suppl. B Biomed. Chem.* **12**, 203–219 (2018).
53. Mamrosh, J. L. et al. A systematic interrogation of MHC class I peptide presentation identifies constitutive and compensatory protein degradation pathways. Preprint at *bioRxiv* https://doi.org/10.1101/2021.10.07.463289 (2022).
54. Yewdell, J. W., Dersh, D. & Fåhraeus, R. Peptide channeling: the key to MHC class I immunosurveillance? *Trends Cell Biol.* **29**, 929–939 (2019).
55. Blum, J. S., Wearsch, P. A. & Cresswell, P. Pathways of antigen processing. *Annu. Rev. Immunol.* **31**, 443–473 (2013).
56. Lev, A. et al. Compartmentalized MHC class I antigen processing enhances immunosurveillance by circumventing the law of mass action. *Proc. Natl Acad. Sci. USA* **107**, 6964–6969 (2010).
57. Yewdell, J. W., Norbury, C. C. & Bennink, J. R. Mechanisms of exogenous antigen presentation by MHC class I molecules in vitro and in vivo: implications for generating $CD8^+$ T cell responses to infectious agents, tumors, transplants, and vaccines. *Adv. Immunol.* **73**, 1–77 (1999).
58. Harel, M. et al. Proteomics of melanoma response to immunotherapy reveals mitochondrial dependence. *Cell* **179**, 236–250. e18 (2019).
59. Spits, M. & Neefjes, J. Immunoproteasomes and immunotherapy—a smoking gun for lung cancer? *J. Thorac. Dis.* **8**, E558–E563 (2016).
60. Boshuizen, J. & Peeper, D. S. Rational cancer treatment combinations: an urgent clinical need. *Mol. Cell* **78**, 1002–1018 (2020).
61. Pfirschke, C. et al. Immunogenic chemotherapy sensitizes tumors to checkpoint blockade therapy. *Immunity* **44**, 343–354 (2016).
62. Mariathasan, S. et al. TGFβ attenuates tumour response to PD-L1 blockade by contributing to exclusion of T cells. *Nature* **554**, 544–548 (2018).
63. McDermott, D. F. et al. Clinical activity and molecular correlates of response to atezolizumab alone or in combination with bevacizumab versus sunitinib in renal cell carcinoma. *Nat. Med.* **24**, 749–757 (2018).
64. Snyder, A. et al. Genetic basis for clinical response to CTLA-4 blockade in melanoma. *New Engl. J. Med.* **371**, 2189–2199 (2014).
65. Hugo, W. et al. Genomic and transcriptomic features of response to anti-PD-1 therapy in metastatic melanoma. *Cell* **165**, 35–44 (2016).
66. Van Allen, E. M. et al. Genomic correlates of response to CTLA-4 blockade in metastatic melanoma. *Science* **350**, 207–211 (2015).
67. Gu, Z., Eils, R. & Schlesner, M. Complex heatmaps reveal patterns and correlations in multidimensional genomic data. *Bioinformatics* **32**, 2847–2849 (2016).
68. Wickam, H. *ggplot2: Elegant Graphics for Data Analysis* (Springer-Verlag New York, 2016).
69. Subramanian, A. et al. Gene set enrichment analysis: a knowledge-based approach for interpreting genome-wide expression profiles. *Proc. Natl Acad. Sci. USA* **102**, 15545–15550 (2005).
70. Trujillo, J. A., Sweis, R. F., Bao, R. & Luke, J. J. T cell-inflamed versus non-T cell-inflamed tumors: a conceptual framework for cancer immunotherapy drug development and combination therapy selection. *Cancer Immunol. Res.* **6**, 990–1000 (2018).

71. Spranger, S., Bao, R. & Gajewski, T. F. Melanoma-intrinsic β-catenin signalling prevents anti-tumour immunity. *Nature* **523**, 231–235 (2015).
72. Uhlen, M. et al. A pathology atlas of the human cancer transcriptome. *Science* **357**, eaan2507 (2017).
73. Thul, P. J. et al. A subcellular map of the human proteome. *Science* **356**, 6340 (2017).
74. Uhlén, M. et al. Tissue-based map of the human proteome. *Science* **347**, 6220 (2015).
75. Welk, V. et al. Proteasome activator PA200 regulates myofibroblast differentiation. *Sci. Rep.* **9**, 1–11 (2019).
76. Klotz, L. et al. Comprehensive clinical profiling of the Gauting locoregional lung adenocarcinoma donors. *Cancer Med.* **8**, 1486–1499 (2019).
77. Kohen, R. et al. UTAP: User-friendly Transcriptome Analysis Pipeline. *BMC Bioinf.* **20**, 1–7 (2019).
78. Stuart, T. et al. Comprehensive integration of single-cell data. *Cell* **177**, 1888–1902.e21 (2019).
79. Grün, D. et al. Single-cell messenger RNA sequencing reveals rare intestinal cell types. *Nature* **525**, 251–255 (2015).
80. Maier, B. et al. A conserved dendritic-cell regulatory program limits antitumour immunity. *Nature* **580**, 257–262 (2020).
81. Heng, T. S. P. et al. The immunological genome project: networks of gene expression in immune cells. *Nat. Immunol.* **9**, 1091–1094 (2008).
82. Raudvere, U. et al. G:Profiler: a web server for functional enrichment analysis and conversions of gene lists (2019 update). *Nucleic Acids Res.* **47**, W191–W198 (2019).
83. Love, M. I., Huber, W. & Anders, S. Moderated estimation of fold change and dispersion for RNA-seq data with DESeq2. *Genome Biol.* **15**, 550 (2014).
84. Vizcaíno, J. A. et al. 2016 update of the PRIDE database and its related tools. *Nucleic Acids Res.* **44**, D447–D456 (2016).

Acknowledgements

We thank the members of the Merbl lab as well as B. Dassa and A. Erez for discussion and critical reading of the manuscript. We thank A. Zippelius for KP1.9 cells. Y.M. is supported by the European Research Council (ERC; grant agreement no. 677748 (StG) and no. 101045613 (CoG)) under the European Union's Horizon 2020 research and innovation program; the I-CORE Program of the Planning and Budgeting Committee and the Israel Science Foundation (grant no. 1775/12); the Cancer Research Institute/Israel Cancer Research Fund CLIP Grant (no. CRI4351); the Melanoma Research Alliance award (https://doi.org/10.48050/pc.gr.143730; Pilot Award program, grant agreement 826874); and the Abisch—Frenkel Foundation for the Promotion of Life Sciences (grant no. 18/WIS3). M.D.S. is supported by a Marie Sklodowska-Curie Individual Fellowship (Horizon 2020 grant no. GAP-845066).

Author contributions

A.J., M.D.S. and Y.M. conceived, designed and interpreted experiments and wrote the manuscript. A.E.-L. and S.M. provided feedback on the manuscript. M.D.S., A.U., H.W.-L. and A.E.-L. performed proteomics preparation and M.D.S. performed the in vitro work. M.P.K., I.J.C. and L.R. performed the in vivo and immunofluorescence experiments. A.A.K., M.P.K. and A.J. performed and analyzed the scRNA-seq experiments. M.D.S. and D.S. performed the bulk RNA-seq experiments. A.J. and K.L. analyzed the ICI cohort. I. Kramer, E.B.-D. and O.Z. conducted the immunohistochemistry experiments. V.N., E.S.-P., M.L. and I. Koch analyzed the German patient cohort. A.K. managed the NSCLC Israeli cohort. M.A. and M.D.S. performed immunopeptidomics and A.J. analyzed the data. Y.L. performed mass spectrometry. A.T.R. and P.C.A.D.F. purified recombinant PSME4. M.D.S. performed all other cellular and biochemical assays. A.J. performed all other bioinformatics. J.B., Y.S., E.E., N.F., C.S., S.M. and Y.M. funded and supervised the work of respective group members and Y.M. supervised the study. A.J. and M.D.S. contributed equally to the manuscript.

Competing interests

The authors declare no competing interests.

Additional information

Extended data is available for this paper at https://doi.org/10.1038/s43018-023-00557-4.

Supplementary information The online version contains supplementary material available at https://doi.org/10.1038/s43018-023-00557-4.

Correspondence and requests for materials should be addressed to Merav D. Shmueli or Yifat Merbl.

Peer review information *Nature Cancer* thanks the anonymous reviewers for their contribution to the peer review of this work.

Reprints and permissions information is available at www.nature.com/reprints.

Publisher's note Springer Nature remains neutral with regard to jurisdictional claims in published maps and institutional affiliations.

[1]Department of Systems Immunology, Weizmann Institute of Science, Rehovot, Israel. [2]Institute of Oncology, Sheba Medical Center, Ramat Gan, Israel. [3]UCL Cancer Institute, CRUK Lung Cancer Centre of Excellence, Cancer Evolution and Genome Instability Laboratory, The Francis Crick Institute, London, UK. [4]Comprehensive Pneumology Center (CPC), University Hospital, Ludwig-Maximilians University, Helmholtz Zentrum Muenchen, Munich, Germany. [5]Member of the German Center for Lung Research (DZL), Munich, Germany. [6]Department of Molecular and Cell Biology, Weizmann Institute of Science, Rehovot, Israel. [7]MRC Laboratory of Molecular Biology, Cambridge, UK. [8]Asklepios Lung Clinic Munich-Gauting, Gauting, Germany. [9]Faculty of Medicine, Tel Aviv University, Tel Aviv, Israel. [10]de Botton Institute for Protein Profiling, The Nancy and Stephen Grand Israel National Center for Personalized Medicine, Weizmann Institute of Science, Rehovot, Israel. [11]Division of Cancer-Microbiome Research, DKFZ, Heidelberg, Germany. [12]Research Center Borstel, Borstel, Germany. [13]Airway Research Center North (ARCN), Member of the German Center for Lung Research (DZL), Borstel, Germany. [14]Institute of Experimental Medicine, Christian-Albrechts University Kiel, Kiel, Germany. [15]Present address: School of Molecular Biosciences, University of Glasgow, Glasgow, UK. [16]These authors contributed equally: Aaron Javitt, Merav D. Shmueli. ✉e-mail: merav.shmueli@weizmann.ac.il; Yifat.merbl@weizmann.ac.il

https://doi.org/10.1038/s43018-023-00557-4

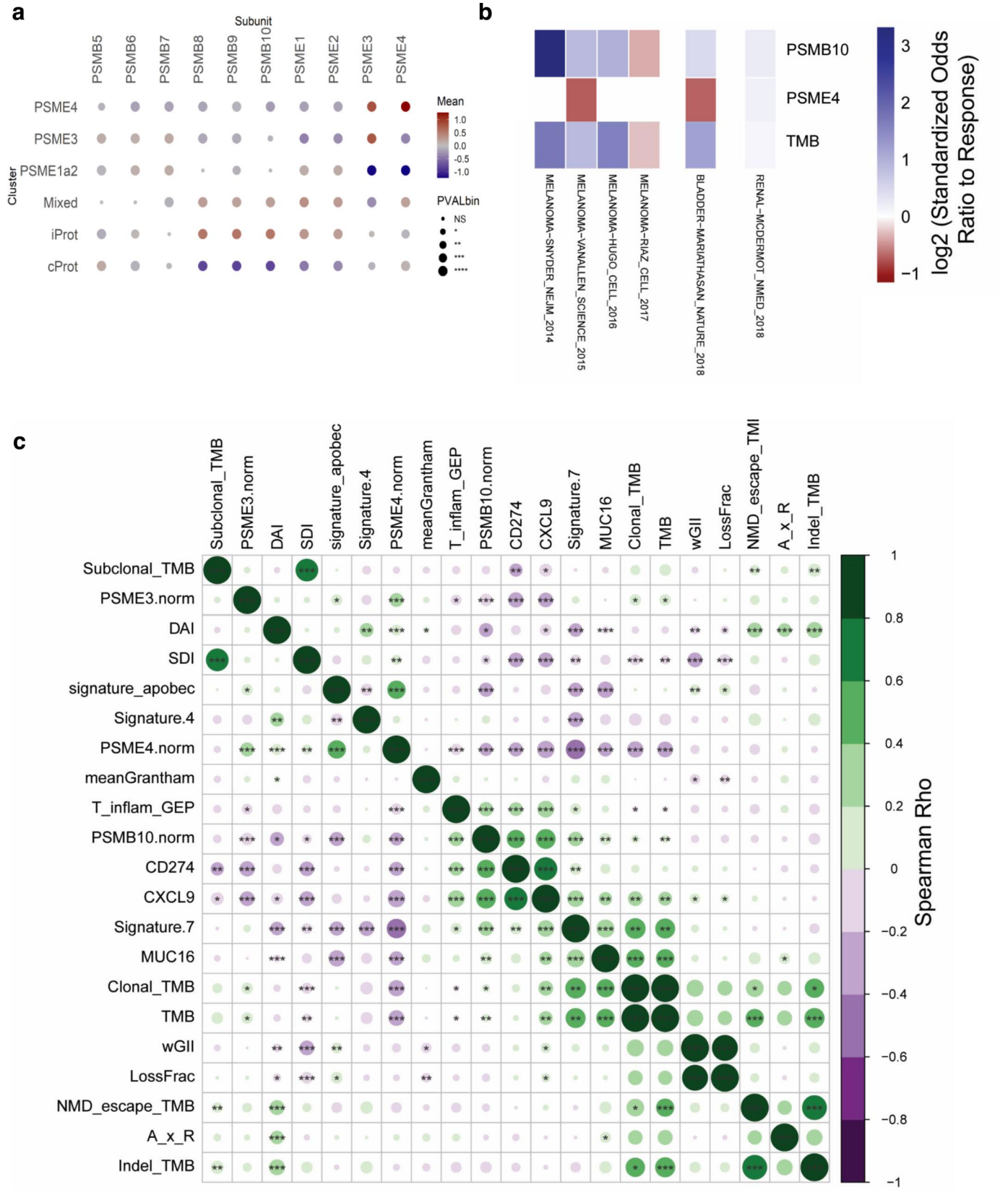

Extended Data Fig. 1 | See next page for caption.

https://doi.org/10.1038/s43018-023-00557-4

Extended Data Fig. 1 | Proteasome expression differs across tumor types. **a**, Tumors were clustered by the expression of either the catalytic (PSMB5, PSMB6, PSMB7, PSMB8, PSMB9, PSMB10) or regulatory subunits (PSME1, PSME2, PSME3 and PSME4). We defined two clusters based on the catalytic cores that we defined as cProt – constitutitve proteasome and iProt – immunoproteasome based on the proteasome expression. Likewise, we defined 4 clusters based on the regulatory subunits that we defined as PSME4, PSME3, PSME1and2 and mixed based on the expression patterns. The graph shows the difference in the mean expression of each subunit for each cluster compared to the full dataset (color) as well as the significance of the difference between the mean and the background (circle size). **b**, The odds ratio of association with survival for the biomarker indicated for each of the cohorts used for the immunotherapy metaanalysis (n = 331 BLCA, 134 SKCM, 72 KIRC tumors). **c**, The spearman correlation between different biomarkers from the ICI1000 + study (n = 331 BLCA, 134 SKCM, 72 KIRC tumors). Circle size shows absolute correlation coefficient and asterisks indicate correlation significance. Precise p values are presented in source data.

https://doi.org/10.1038/s43018-023-00557-4

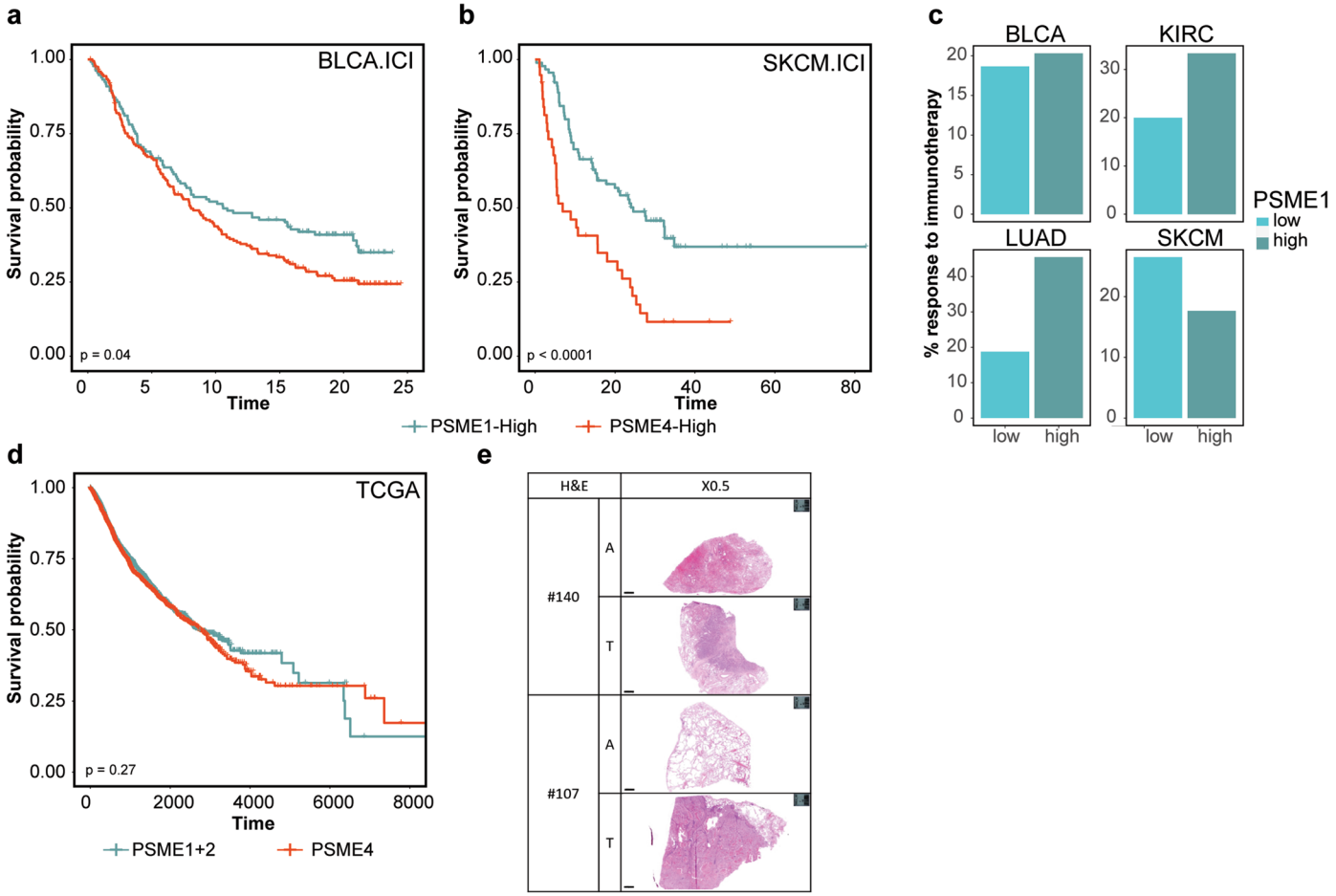

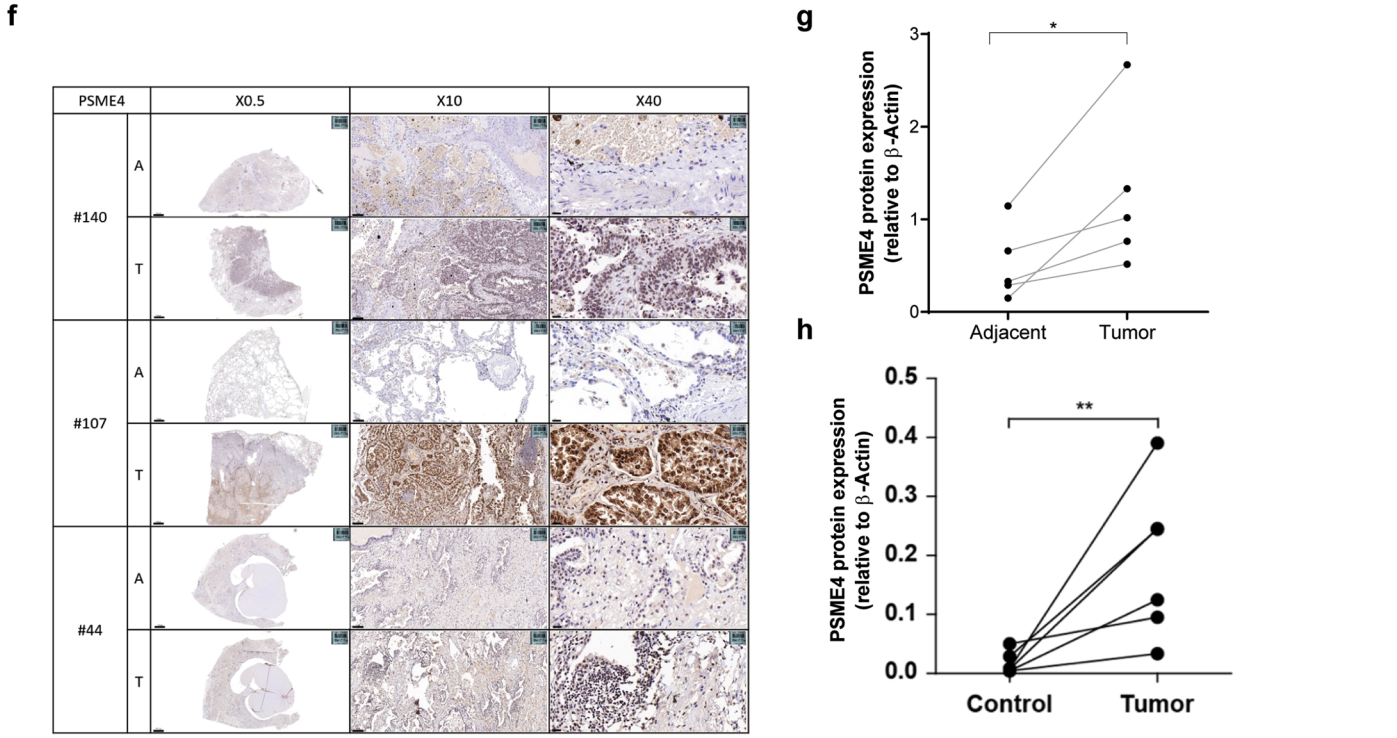

Extended Data Fig. 2 | See next page for caption.

https://doi.org/10.1038/s43018-023-00557-4

Extended Data Fig. 2 | PSME4 is increased in NSCLC and stratifies response. a,**b**, Kaplan-Meier curves of patient survival stratified by the ratio in expression between PSME4 and PSME1 for the melanoma cohorts treated with immunotherapy (SKCM ICI, **a**) or bladder cancer (BLCA ICI, **b**). Significance determined from Log-ranked test. **c**, Patients were stratified by PSME1 expression in the ICI cohorts and the response rate for the PSME1-low and PSME1-high groups are shown. PSME1 alone does not consistently categorize a response status among the cancer types analyzed. **d**, Kaplan-Meier curves of patient survival stratified by the regulatory subunit clusters defined in 'Fig. 1c' for the TCGA cohorts. Significance determined from Log-ranked test (n = 9724 tumors). **e**, H&E staining of tumor or adjacent tissue from 2 representative patients (Scale bar represent 2000 μm.). **f**, Immunohistochemistry staining for PSME4 of tumor or adjacent tissue from 3 representative patients (Scale bar represent 2000 μm (X0.5), 100 μm (X10) and 20 μm (X40)). **g**, Immunoblotting band intensity across tumor or adjacent tissues were quantified for PSME4 and normalized to actin as a loading control (two-sided paired student's t-test *P = 0.0437, n = 5 patients). **h**, Immunoblotting band intensity across tumor or adjacent lung tissues from an independent cohort were quantified for PSME4 and normalized to actin as a loading control (two-sided paired student's t-test **P = 0.01, n = 6 patients).

https://doi.org/10.1038/s43018-023-00557-4

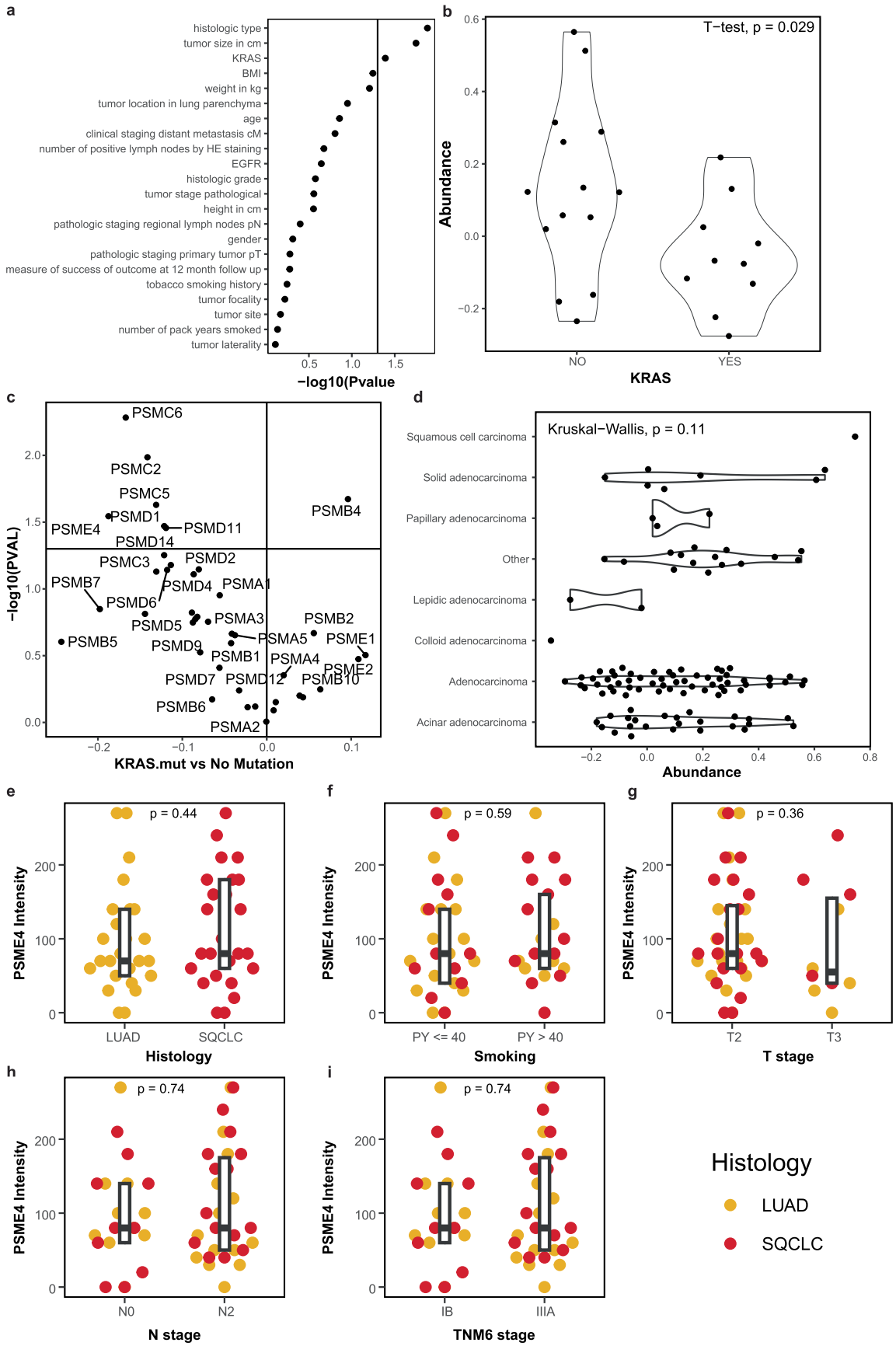

Extended Data Fig. 3 | See next page for caption.

https://doi.org/10.1038/s43018-023-00557-4

Extended Data Fig. 3 | PSME4 is not strongly associated with other factors in Lung Adenocarcinoma. a – **d**, Using the protein abundance of PSME4 normalized to the mean abundance of the core proteasome from the CPTAC LUAD cohort compared to patient data, we examined the association to other factors. (**a**) The significance of the association between each of the factors listed and the abundance of PSME4 across the samples. For discreet factors, the mean abundance between the different groups was compared with a one-way ANOVA. For continuous factors, the significance of the spearman correlation between the protein abundance and factor is displayed. (**b**) Slight increase in PSME4 abundance in tumors that do not have a KRAS mutation (two-sided student's t test, n = 111 tumors). (**c**) Change in abundance of all the proteasome subunits between KRAS mutant and wild type KRAS tumors. As most proteasome subunits are decreased in abundance in KRAS mutant cancers, we conclude that the change we observe in PSME4 is not due specifically to PSME4 level or function. Significance determined from two-sided student's T test, n = 111 tumors. (**d**) The abundance of PSME4 normalized to the core in each of the histological subtypes of PSME4 (n = 111 tumors). Variation between the subtypes only occurs in rare groups that cannot clearly be distinguished due to sample size. **e-i**, Quantification of PSME4 in NSCLC subtypes lung adenocarcinoma (LUAD) and squamous cell lung carcinoma (SQCLC) measured by immunohistochemistry staining. Samples are stratified by subtype (**e**), smoking level (**f**), T stage (**g**), N stage (**h**) or TNM stage (**i**). Dots are colored by subtype (LUAD – yellow, SQCLC - red). 50 independent patient samples were assessed. Box plots span the first to third quartiles. Significance determined by Wilcoxon rank sum test.

https://doi.org/10.1038/s43018-023-00557-4

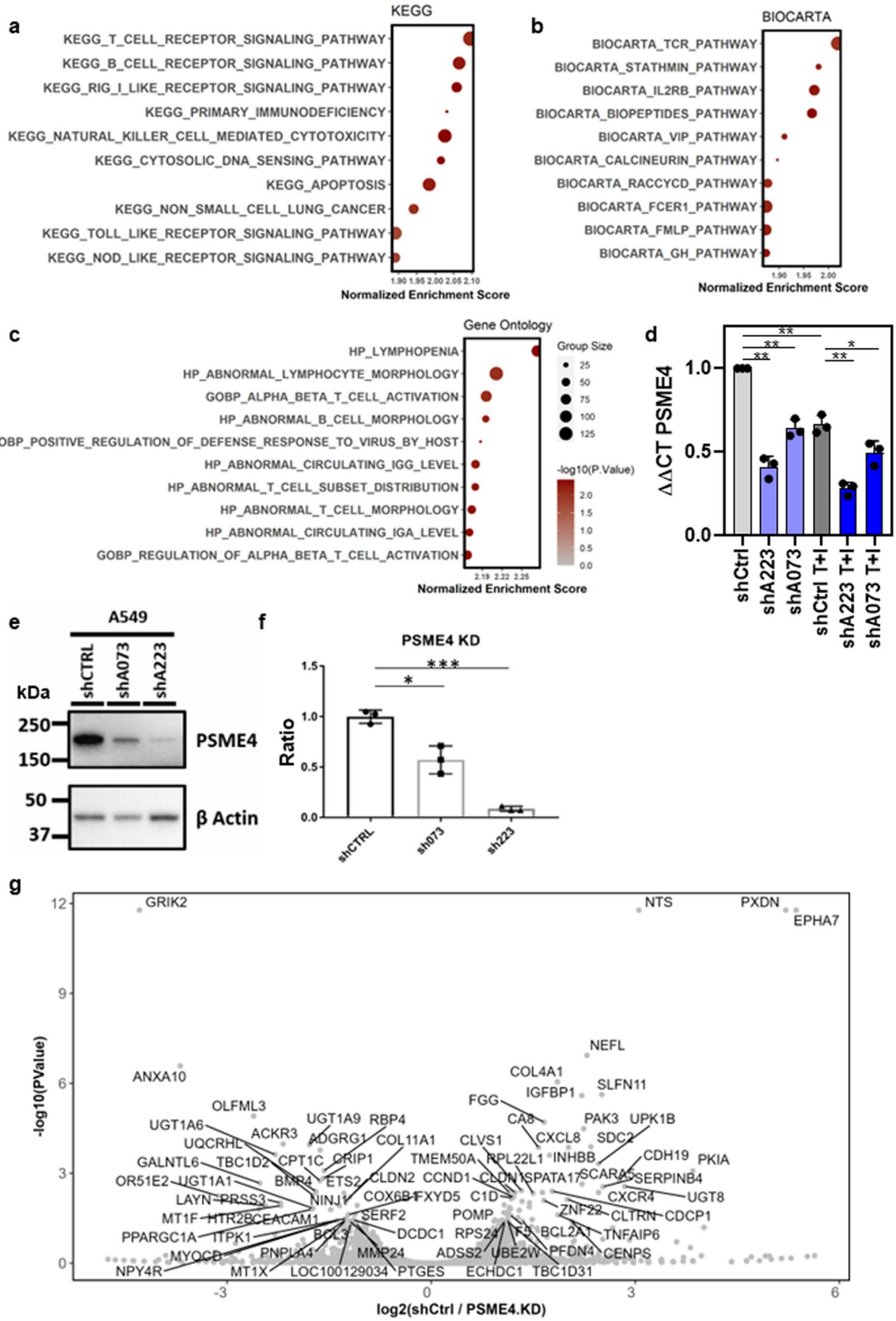

Extended Data Fig. 4 | See next page for caption.

https://doi.org/10.1038/s43018-023-00557-4

Extended Data Fig. 4 | PSME4 low tumors are enriched in T cell pathways with proteomics but not transcriptomics. a – **c**, Pathway enrichment analysis was performed for the tumors in the CPTAC-LUAD cohort that are defined as PSME4 enriched (based on Fig. 1) using the (**a**) KEGG (**b**) BIOCARTA or (**c**) Gene Ontology datasets. The Normalized Enrichment score (for the PSME4-low tumors compared to the PSME4-high tumors) is plotted with the circle size indicated pathway size and the color indicating the significance of the enrichment determined by FDR corrected q-value (n = 111 tumors). **d**, qPCR of PSME4 in A549 cell line following depletion of PSME4 with shA223 or shA073 compared to shCtrl with and without stimulation with TNFα and IFNγ (T + I) (two-sided paired student's T test, P values in source data.; n = 3 independent biological experiments; bars indicate mean ± s.d.). **e**, Lysates of A549 cells with PSME4 knockdown (shA223 and shA073) or control (shCtrl) were blotted for PSME4 and β-Actin as a loading control. The experiment was repeated twice with similar results. **f**, Quantification of PSME4 band intensity in A549 cell line with PSME4 KD (A223 or A073) or shCtrl (Ctrl) across three independent samples normalized to actin as a loading control and to shCtrl (Welch's corrected two-sided student's T-test *P = 0.0186; ***P = 0.0005; bars indicate mean ± s.d.). **g**, The fold change in gene expression between the A549 cell line following depletion of PSME4 with shA223 compared to shCtrl is plotted against the significance of the change. Genes which passed the FDR adjusted P value cutoff of 0.05 are presented. Significance is determined by Wald test with BH correction.

https://doi.org/10.1038/s43018-023-00557-4

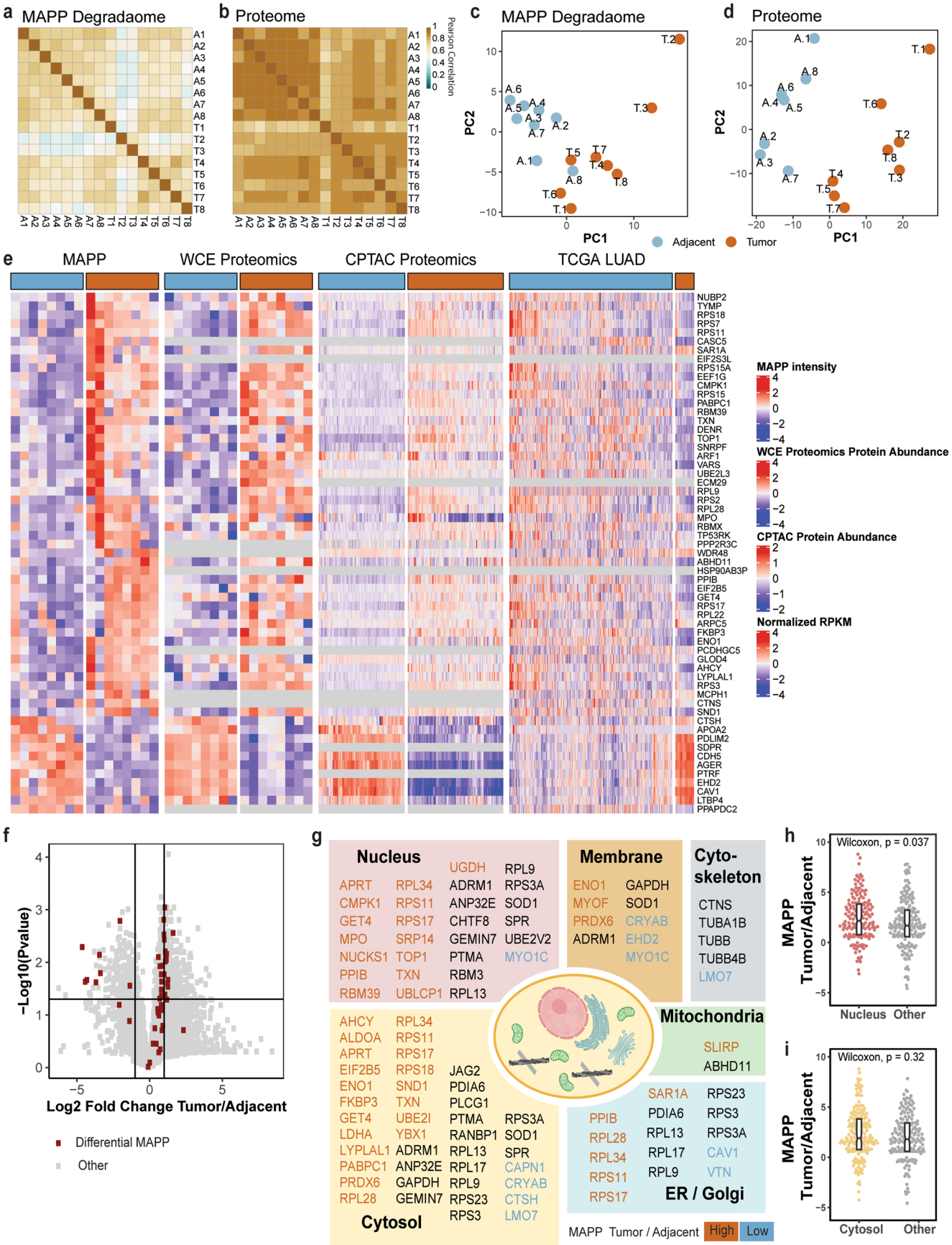

Extended Data Fig. 5 | See next page for caption.

https://doi.org/10.1038/s43018-023-00557-4

Extended Data Fig. 5 | Proteome and Degradome landscapes classify tumor and adjacent tissues across patients. a,**b**, Pairwise Pearson correlation between the proteins identified in each sample by MAPP (**a**) or the whole cell proteome (**b**; n = 8 adjacent and 8 tumor samples). **c**,**d**, Principal component analysis based on the identities and abundances of the proteins identified by MAPP (**c**) or whole cell proteome (**d**). Tumor (T) and adjacent (A) samples are annotated and plotted with principal component PC1 against PC2 (n = 8 adjacent and 8 tumor samples). **e**, The abundance of proteins that were different between tumor and adjacent lung tissues as determined by MAPP are shown in four datasets: MAPP (n = 16 samples), whole cell Proteomics (n = 16 samples), CPTAC proteomics (n = 215 samples) and TCGA LUAD (c = 573 samples). Proteins not identified in a dataset are shown as grey, otherwise the normalized abundance / expression is shown as a red to blue scale. **f**, The fold change in abundance for each protein between the tumor and adjacent tissue in the whole cell proteome is plotted against the significance of their difference (negative log10 transformed P value) in grey. The proteins identified as differential in MAPP (listed in table S2) are annotated in red. **g**, Proteins identified in MAPP organized by their annotated cellular localization (Human Protein Atlas). Proteins are colored based on the mean of degradation ratios between tumor and adjacent tissues across patients (orange: above median degradation ratio, blue: degradation ratio below 0, black: ratio between median and 0). Proteins that are annotated to localize at more than one organelle appear more than once. **h**,**i**, The mean ratio of degradation (MAPP) between the tumor and adjacent tissues for proteins annotated to the nucleus (**h**) or cytosol (**i**) versus other proteins. The nuclear proteins on average had significantly higher ratio compared to the background proteins (Wilcoxon rank sum test p = 0.037; n = 337 proteins identified across 8 tumor and 8 adjacent tumor samples). Box plots span the first to third quartiles and whiskers show 1.5× interquartile range.

https://doi.org/10.1038/s43018-023-00557-4

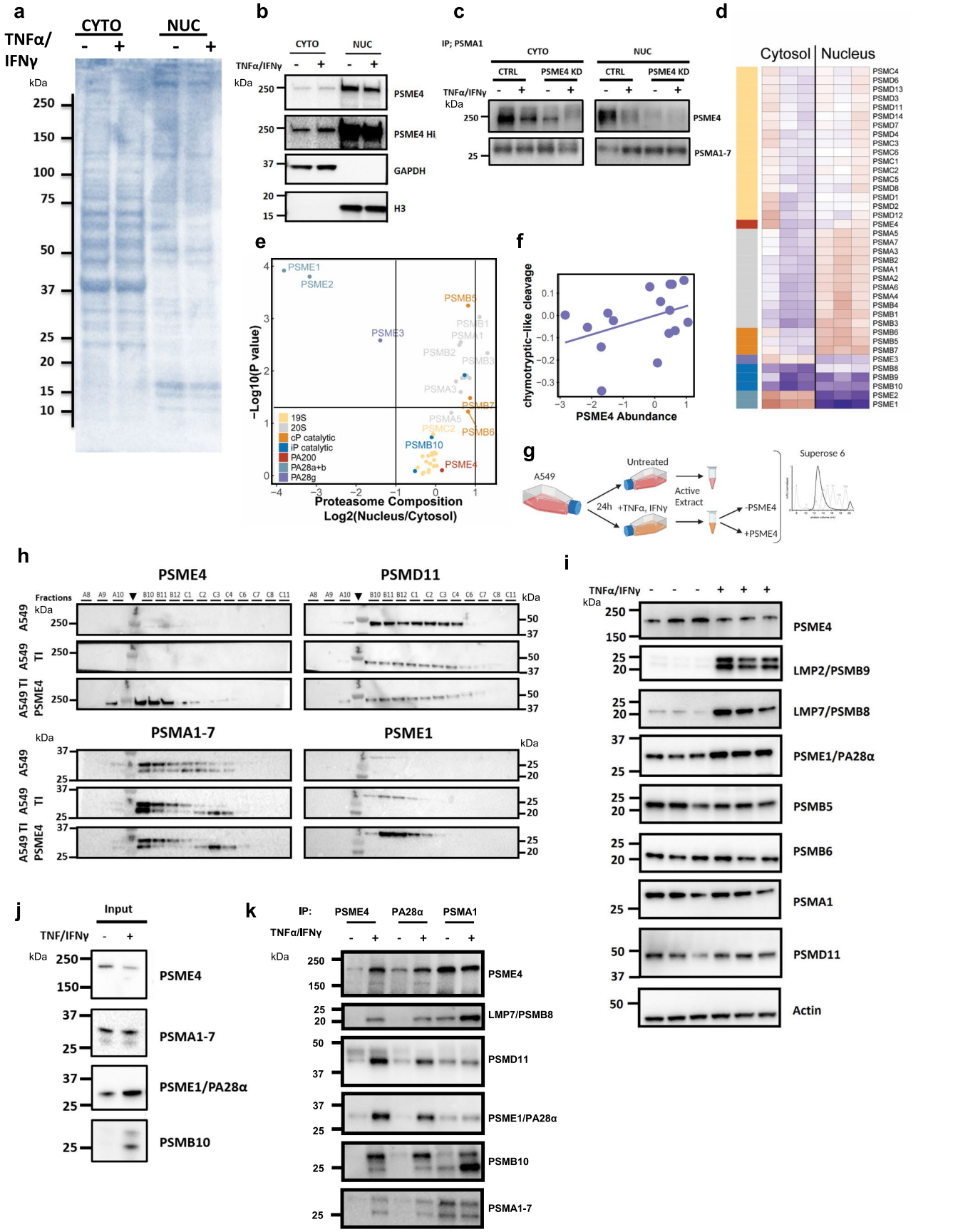

Extended Data Fig. 6 | See next page for caption.

https://doi.org/10.1038/s43018-023-00557-4

Extended Data Fig. 6 | PSME4 is incorporated into multiple species of proteasome complex in multiple localizations. a,**b**, Cytosolic and nuclear cellular fractions of A549 were stained with Coomassie (**a**) and immunoblotted for PSME4 (**b**). GAPDH and Histone H3 were used as cytosolic and nuclear markers respectively. **c**, Proteasome complexes were immunoprecipitated (IP) with PSMA1 from A549 cells (with PSME4 depletion or control) that were either treated with TNFα and IFNγ or left untreated and blotted for the indicated proteasome subunits. This experiment was repeated twice with similar results. **d**,**e**, Abundance of the proteasome subunits following mass spectrometry analysis of the αPSMA1 immunoprecipitate from nuclear and cytosolic fractions. A heatmap of abundances where values are scaled by row (**d**). A volcano plot showing the log2 transformed fold change between median abundance of each subunit in the nuclear and cytosolic proteasomes is plotted against the significance of the difference (two-sided student's T.test; **e**). Colors indicate the identity of the proteasome subunits. **f**, The carboxy terminal residue of peptides was used to classify these peptides based on the proteasome activity attributed to their cleavage. The abundance of PSME4 in the samples based on whole cell proteomics correlated with the chymotryptic-like signature (spearman rho = 0.33, n = 8 tumor and 8 adjacent samples). **g**, Workflow of the size exclusion separation. A549 cells were treated with TNFα and IFNγ (TI) for 24 hours or left untreated, lysed and then recombinant PSME4 was added to the TI treated A549 lysates. **h**, Lysates were separated by size using Superose6 gel filtration column and blotted against different proteasome subunits as indicated. **i**, Input lysates of A549 cells treated with TNFα and IFNγ (TI) or untreated used for immunoprecipitation shown in Fig. 3f blotted with the indicated antibody. **j**,**k**, Input lysates of A549 cells treated with TNFα and IFNγ (TI) or untreated (**j**) and the immunoprecipitation with the indicated antibody (**k**) blotted for the indicated proteasome subunit. Experiments in **h**-**k** were repeated twice with similar results.

https://doi.org/10.1038/s43018-023-00557-4

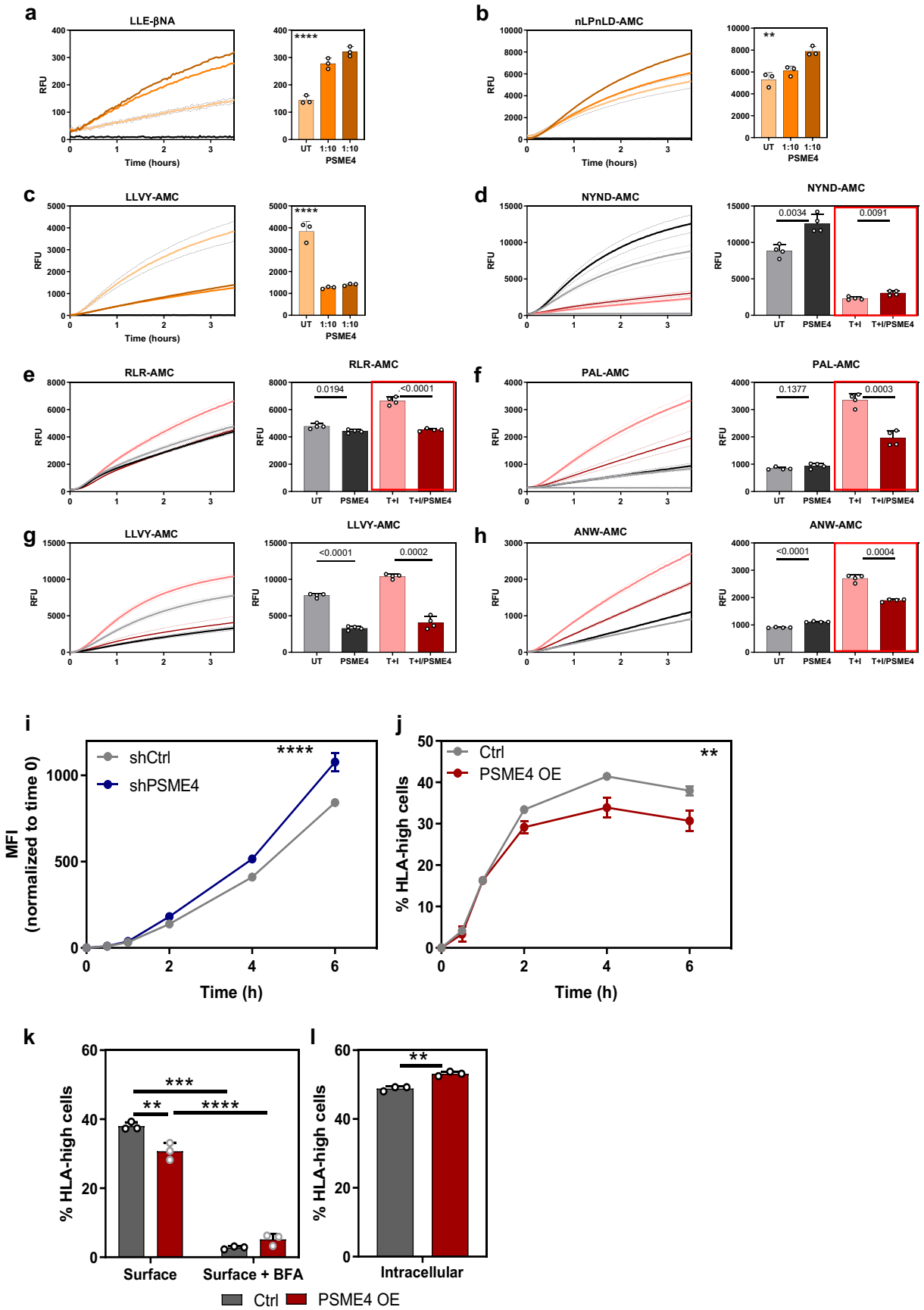

Extended Data Fig. 7 | See next page for caption.

https://doi.org/10.1038/s43018-023-00557-4

Extended Data Fig. 7 | PSME4 modulates proteasome activity and HLA maturation. a-c, Proteasome activity assays using fluorogenic substrates LLE-bNA (caspase, β1;**a**), nLPnLD-AMC (caspase, β1;**b**), or LLVY-AMC (chymotryptic, β5;c) for 3.5 hours. Relative fluorescence unit (RFU) of the substrate is shown across the 3.5 hours of the experiment (left) or at the endpoint (right). Recombinant PSME4 in different ratios, as indicated, was added to A549 lysates (one-way ANOVA; **P = 0.0022, **** P < 0.0001; bars indicate mean ± s.d.; n = 3 independent samples). **d-h**, Proteasome activity assays using the nLPnLD-AMC (caspase, β1; **d**), RLR-AMC (tryptic, β2/ β2i; **e**), PAL-AMC (chymotryptic, β1i; **f**), LLVY-AMC (chymotryptic, β5/ β5i; **g**) or ANW-AMC (chymotryptic, β5i; **h**) substrates. Relative fluorescence unit (RFU) of the substrate is shown across the 3.5 hours of the experiment (left) or at the endpoint (right). A549 lysates were treated with TNFα and IFNγ (T + I; red) or untreated (UT; black) and recombinant PSME4 was added to the lysate where indicated (two-sided paired student's T-test) Red squares indicate the portion of the Figure reproduced in Fig. 3 (n = 4 independent samples; bars indicate mean ± s.d.). **i**, The MFI of HLA on the cell surface was monitored using flow cytometry following acid stripping. PSME4 depletion (shPSME4) increases levels of HLA on the cell surface starting from 2 hours after stripping (2-way-ANOVA ****P ≤ 0.0001, n = 3 independent samples; bars indicate mean ± s.d.). **j**, The percentage of HLA-high cells was monitored using flow cytometry following acid stripping. PSME4 overexpression (PSME4 OE) decreases levels of HLA on the cell surface starting from 4 hours after stripping. (2-way-ANOVA **P = 0.0033, n = 3 independent samples; bars indicate mean ± s.d.). **k**,**l**, The percent of cells with high levels of HLA on the surface is significantly decreased following PSME4 overexpression (**k**; n = 3 independent samples per condition). By contrast, the intracellular levels of HLA are significantly increased upon PSME4 overexpression (**l**; bars indicate mean ± s.d.).

https://doi.org/10.1038/s43018-023-00557-4

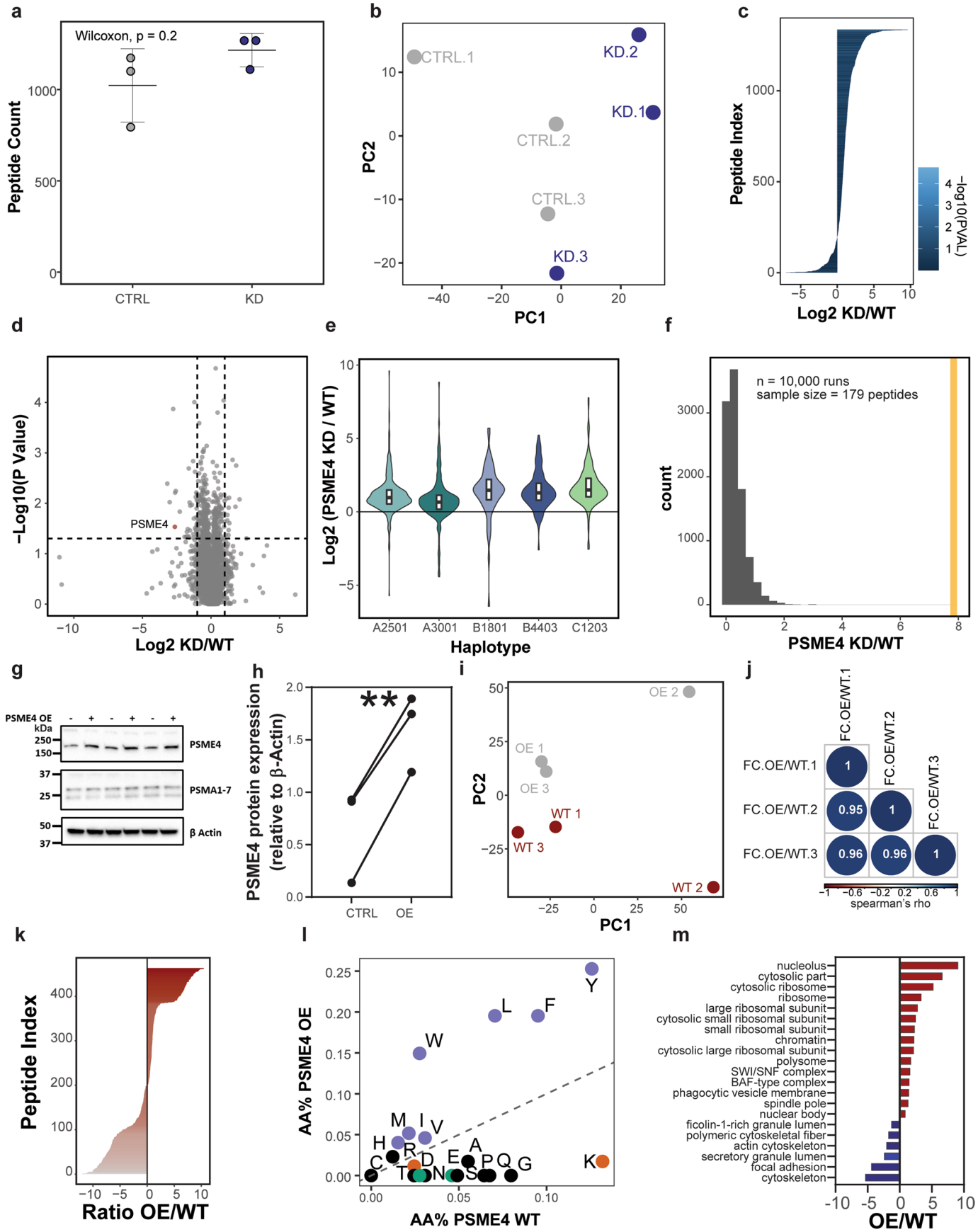

Extended Data Fig. 8 | See next page for caption.

https://doi.org/10.1038/s43018-023-00557-4

Extended Data Fig. 8 | The cellular immunopeptidome is altered by PSME4 modulation. a, The number of peptides identified in A549 cells 6 hours after acid stripping and stimulation with TNFα and IFNγ. Peptide count is shown both for cells depleted of PSME4 (KD) or control (Ctrl). Peptides were derived from n = 3 independent samples per treatment (Wilcoxon rank sum test; bars indicate mean ± s.d.). **b**, Principal component analysis (PCA) of the peptides identified and their abundances in the immunopeptidomics experiment (n = 3 independent samples). **c**, The mean fold change ratio between PSME4 depleted (KD) and control (WT) peptides is plotted for all the peptides identified. (One-sided T test of FC versus mu = 0) **d**, Whole cell proteomics was performed and a volcano plot for the change in protein abundance between the depleted (KD) and control (WT) conditions is shown (two-sided Student's T test). **e**, Peptides are divided based on predicted haplotype and the fold change between PSME4 depletion (KD) is shown for each group (n = 3 independent samples). Box plots span the first to third quartiles and whiskers show 1.5× interquartile range. **f**, The fold change between KD and WT for the 179 peptides which end in K (orange line) was compared to 179 peptides randomly selected from the immunopeptidome 10,000 times (grey). **g**, A549 cells transfected with a PSME4-expressing plasmid or empty vector as a control. Cell lysates were blotted for PSME4. β-Actin was blotted as a loading control. Experiment was repeated twice with similar results **h**, Quantification of PSME4 band intensity in A549 cell line with PSME4 OE or Ctrl across n = 3 independent samples normalized to actin as a loading control (two-sided paired student's t-test **P = 0.0045). **i**, Principal component analysis (PCA) of the peptides identified and their abundances in the immunopeptidomics experiment. **j**, Following ratio normalization to control for batch effect, the correlation between the ratios for the 463 altered peptides is shown across the replicates. **k**, The mean fold change ratio between overexpression (OE) and control peptides is plotted for the 463 peptides differentially presented upon PSME4 overexpression. **l**, The percentage of peptides with each indicated carboxy terminus is plotted for the peptides significantly increased in the PSME4 overexpression or empty vector control (denoted WT). **m**, The ratio between the enrichment score for the cellular component groups enriched in peptides increased in expression upon PSME4 overexpression (OE) over control (WT).

https://doi.org/10.1038/s43018-023-00557-4

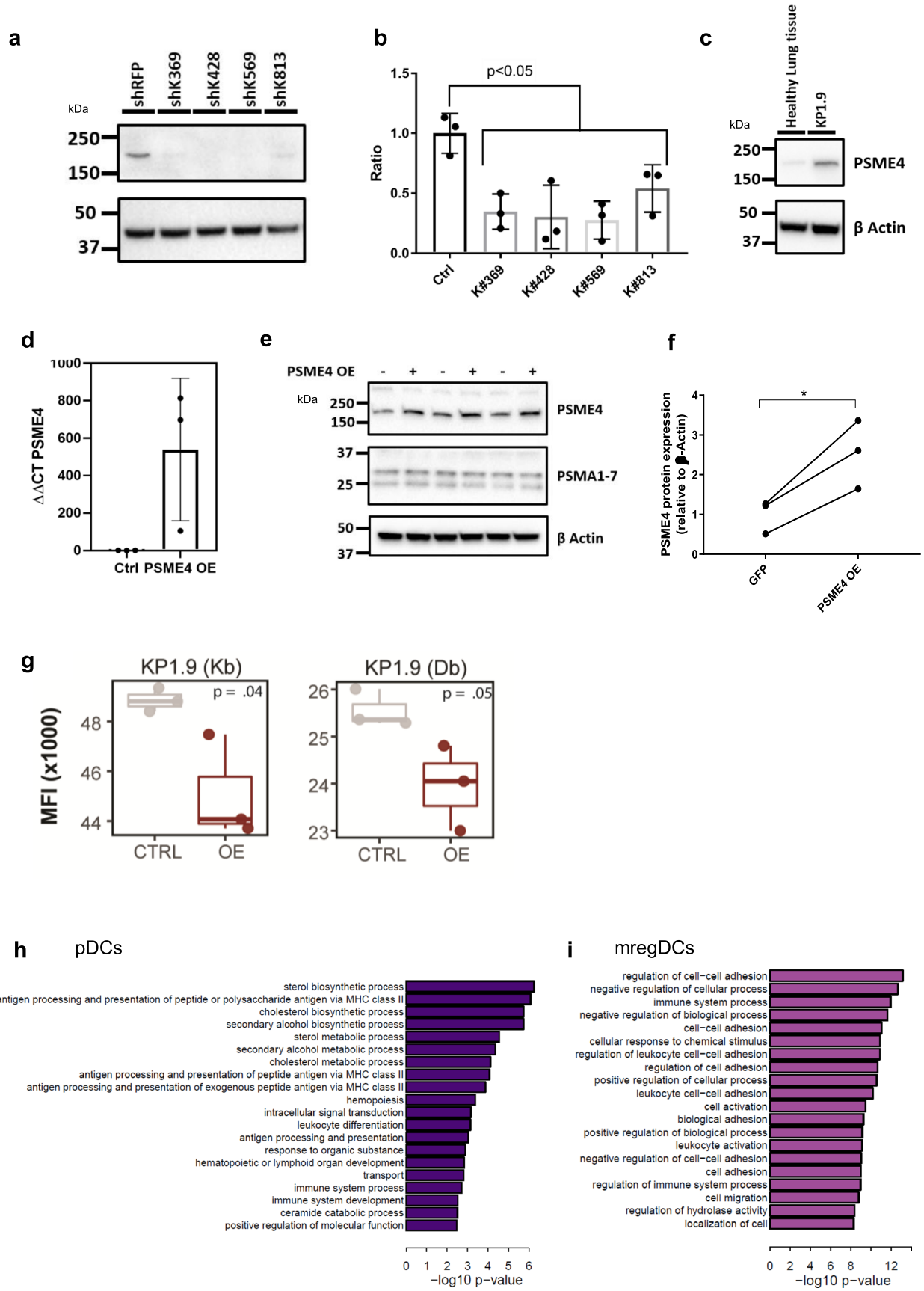

Extended Data Fig. 9 | See next page for caption.

https://doi.org/10.1038/s43018-023-00557-4

Extended Data Fig. 9 | PSME4 depletion in KP1.9 cells increases MHC levels. **a**, Lysates of KP1.9 cells with PSME4 knockdown (shK369 and shK428, shK569 or shK813) or control (shRFP) were blotted for PSME4 and β-Actin as a loading control. **b**, Quantification of PSME4 band intensity in KP1.9 cell line with PSME4 KD or Ctrl (shRFP) across independent samples per condition normalized to actin as a loading control and to shRFP (bars indicate mean ± s.d.; two-sided student's T test, shK428 P = 0.018, shK569 P = 0.0054 or shK813 P = 0.0368). **c**, KP1.9 cells and healthy mouse lung tissue were blotted for PSME4. β-Actin was blotted as a loading control. **d**, qPCR shows the expression of PSME4 in KP1.9 cells transfected with a PSME4 overexpression plasmid (n = 3 independent experiments; bars indicate mean ± s.d.). **e**, KP1.9 cells transfected with a PSME4 overexpression plasmid (+) or GFP (-) as a control. Cell lysates were blotted for PSME4 or PSMA1-7. β-Actin was blotted as a loading control. **f**, Band intensities of **e** were quantified for PSME4 and normalized to actin as a loading control (two-sided paired student's t-test *P = 0.0331; n = 3 independent samples). **g**, Median fluorescence intensity from flow cytometry analysis of MHC-I expression using a Kb or Db antibody on KP1.9 cells with PSME4 overexpression or control (n = 3 independent samples). Box plots span the first to third quartiles and whiskers show 1.5× interquartile range (Wilcox test). **h**,**i**, GO-term enrichment (of key markers from the plasmacytoid DC (**h**) or mature DCs enriched in immunoregulatory molecules (mregDCs; **i**) population. Significance determined by FDR corrected q-value.

https://doi.org/10.1038/s43018-023-00557-4

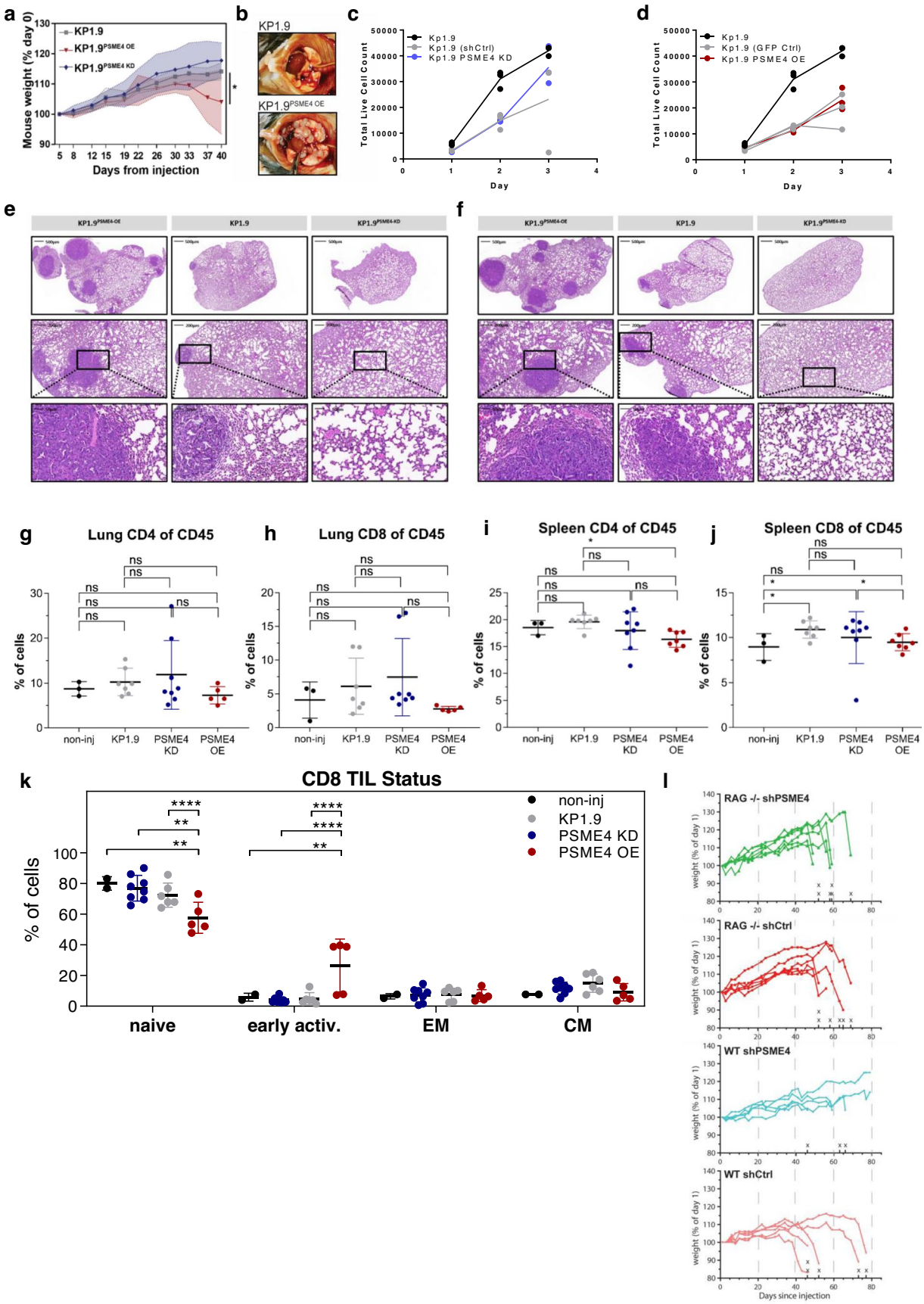

Extended Data Fig. 10 | See next page for caption.

https://doi.org/10.1038/s43018-023-00557-4

Extended Data Fig. 10 | PSME4 overexpression in KP1.9 cells increases tumor burden in an immune-dependent manner. a, Weights of C57/B6 mice bearing orthotopic wild type (KP1.9; n = 7), PSME4-overexpressing (OE; n = 7), or PSME4-deficient (KD; n = 8) KP1.9 tumors. Weights are normalized to the starting weight of each mouse. Overexpression shows significantly decreased weight as a proxy for increased disease severity (matched 2-way ANOVA *p = 0.0322). **b**, Mice bearing PSME4 overexpressing (OE) tumors showed increased tumor burden compared to the control KP1.9 tumors. **c**, Measurement of the cell growth of KP1.9, KP1.9 expressing shCtrl or shPSME4 (PSME4 KD) for 3 days (n = 3 independent experiments). **d**, Measurement of the cell growth of KP1.9, KP1.9 expressing GFP overexpression (GFP Ctrl) or PSME4 overexpression (OE) for 3 days (n = 3 independent experiments). **e**,**f**, Two representative images per condition in addition to Fig. 6c of H&E staining of lungs from mice bearing KP1.9, KP1.9$^{PSME4\ OE}$, or KP1.9$^{PSME4\ KD}$ tumors. **g**-**j**, The percentages of the CD45 positive population in the lung (**g** and **h**; n = 3 non-inj, 7 KP1.9, 8 KD, 7 OE mice) or spleen (**i** and **j**; n = 3 non-inj, 7 KP1.9, 8 KD, 5 OE mice) from the mice bearing KP1.9, KP1.9$^{PSME4\ OE}$, or KP1.9$^{PSME4\ KD}$ tumors or mice not injected (non-inj) with tumor cells that are CD4 (g, i) or CD8 (h, j) positive. One way ANOVA with post-hoc TUKEY analysis was used to compare populations (*P ≤ 0.05; bars indicate mean ± s.d.)). **k**, The percent of different subsets of CD8-positive lymphocytes (naïve, early activated, effector memory [EM] or central memory [CM], which are CD62L and/or CD44 positive, in the lung of mice bearing KP1.9$^{PSME4\ OE}$ (n = 5), KP1.9$^{PSME4\ KD}$ (n = 8) or KP1.9 (n = 6) tumors compared to mice not bearing tumors (non-inj; n = 2; two-way ANOVA with post-hoc Tukey – P values in Source Data). The portion of the figure marked in the box is reproduced in Fig. 4g (bars indicate mean ± s.d.). **l**, The body weight of wild-type or immunocompromised RAG1 -/- mice injected with KP1.9 lung tumors expressing either shPSME4 or Ctrl shRNA. The weight of each mouse is normalized to the starting weight at day 1. 'X' indicates death.

nature portfolio

Corresponding author(s): Yifat Merbl

Last updated by author(s): Mar 30, 2023

Reporting Summary

Nature Portfolio wishes to improve the reproducibility of the work that we publish. This form provides structure for consistency and transparency in reporting. For further information on Nature Portfolio policies, see our Editorial Policies and the Editorial Policy Checklist.

Statistics

For all statistical analyses, confirm that the following items are present in the figure legend, table legend, main text, or Methods section.

n/a	Confirmed
☐	☒ The exact sample size (*n*) for each experimental group/condition, given as a discrete number and unit of measurement
☐	☒ A statement on whether measurements were taken from distinct samples or whether the same sample was measured repeatedly
☐	☒ The statistical test(s) used AND whether they are one- or two-sided *Only common tests should be described solely by name; describe more complex techniques in the Methods section.*
☐	☒ A description of all covariates tested
☐	☒ A description of any assumptions or corrections, such as tests of normality and adjustment for multiple comparisons
☐	☒ A full description of the statistical parameters including central tendency (e.g. means) or other basic estimates (e.g. regression coefficient) AND variation (e.g. standard deviation) or associated estimates of uncertainty (e.g. confidence intervals)
☐	☒ For null hypothesis testing, the test statistic (e.g. *F*, *t*, *r*) with confidence intervals, effect sizes, degrees of freedom and *P* value noted *Give P values as exact values whenever suitable.*
☒	☐ For Bayesian analysis, information on the choice of priors and Markov chain Monte Carlo settings
☐	☒ For hierarchical and complex designs, identification of the appropriate level for tests and full reporting of outcomes
☐	☒ Estimates of effect sizes (e.g. Cohen's *d*, Pearson's *r*), indicating how they were calculated

Our web collection on statistics for biologists contains articles on many of the points above.

Software and code

Policy information about availability of computer code

Data collection	Commercial Software: Attune NxT Software V3.1.1243.0, Bio-Rad-Image-Lab-Software-6.1, StepOne Software v2.3, BioTek GenS, 3DHISTECH CaseViewer 2.4, BD FACSDiva software V8.0.1
Data analysis	Data in this study were analyzed by public softwares: MaxQuant vl.6.0.16, FlowJo vl0.7.1, R v3.4.2 GraphPad Prism v7.04, Python v3.7, GSEA 4.0.3, Excel v2020, ImageJ 1.8.0 , UTAP V1.10, Custom code can be found in : https://github.com/merbllab/PSME4_NatCancer

For manuscripts utilizing custom algorithms or software that are central to the research but not yet described in published literature, software must be made available to editors and reviewers. We strongly encourage code deposition in a community repository (e.g. GitHub). See the Nature Portfolio guidelines for submitting code & software for further information.

Data

Policy information about availability of data

All manuscripts must include a data availability statement. This statement should provide the following information, where applicable:

- Accession codes, unique identifiers, or web links for publicly available datasets
- A description of any restrictions on data availability
- For clinical datasets or third party data, please ensure that the statement adheres to our policy

The mass spectrometry proteomics data have been deposited to the ProteomeXchange Consortium via the PRIDE partner repository with the dataset identifiers PXD019573, PXD028364 and PXD037365.)

The single cell RNA-seq data have been deposited to ArrayExpress database at EMBL-EBI (www.ebi.ac.uk/arrayexpress) under accession no. E-MTAB-10745. Bulk RNAseq data have been deposited to GEO under accession no GSE201460

Human research participants

Policy information about studies involving human research participants and Sex and Gender in Research.

Reporting on sex and gender	Gender was defined based no a self-reported metric
Population characteristics	Identifiers MIDGAM code Collection Month Collection Year Age Gender Histology Pre-Op treatment Smoking Pl NSCLC_107 1 2016 64 M Adenocarcinoma No current P2 NSCLC_113 2 2016 53 M adenocarcinoma No current P3 NSCLC_140 9 2016 61 M Adenocarcinoma No current P4 NSCLC_22 11 2014 66 M adenocarcinoma No current P5 NSCLC_30 12 2014 64 M Adenocarcinoma No current P6 NSCLC_ 40 1 2015 58 M adenocarcinoma No current. Heavy smoker P7 NSCLC_ 44 2 2015 66 M adenocarcinoma No current P8 NSCLC_76 7 2015 54 M adenocarcinoma No current P9 NSCLC_81 8 2015 69 M Adenocarcinoma No current
Recruitment	This was a retrospective study and no participants were recruited specifically for this study.
Ethics oversight	Samples were obtained under the approval of the Ministry of Health (MOH) IRB approval for the Israel National Biobank for Research (MIDGAM), protocol no. 118-2018 or the ethics committee of the Ludwig-Maximilians University Munich according to national and international guidelines (project number 333-10).

Note that full information on the approval of the study protocol must also be provided in the manuscript.

Field-specific reporting

Please select the one below that is the best fit for your research. If you are not sure, read the appropriate sections before making your selection.

☒ Life sciences ☐ Behavioural & social sciences ☐ Ecological, evolutionary & environmental sciences

For a reference copy of the document with all sections, see nature.com/documents/nr-reporting-summary-flat.pdf

Life sciences study design

All studies must disclose on these points even when the disclosure is negative.

Sample size	Statistical methods were not used to predetermine sample size. Sample size for each experiment is stated in figure captions and data For scRNAseq, previous reports have indicated 2 mice per condition are sufficient (Zillionis et al. Immunity 2019) and we used 3 samples in each group to provide enough data to draw conclusions. For other in vivo experiments, based on Pfirscke et al. Immunity (2016) and a pilot experiment, we estimated that 6-10 mice per group will be sufficient to show differences.
Data exclusions	No data was excluded from the analysis with the exception of one sample from the proteasome profiling experiment which did not yield peptides (technical error and limited starting material) and therefore was not included in the analysis.
Replication	All experiments were performed in three individual replicates unless otherwise mentioned. For each experiment, all compared conditions were analyzed by MS at the same time. For the NSCLC degradome analysis nine samples from tumors and adjacent tissue were analyzed, one was excluded for poor technical quality. The samples were processed independently and analyzed by MS at the same time to maintain comparability across samples and decrease batch effects. When representative images are shown, at least two independent experiments were performed with similar results. In vivo and biochemistry experiments were repeated at least three times sucessully. In flow cytometry experiments, samples were excluded for low cell yield.
Randomization	Mice were randomly chosen on cage basis to receive either control or knockdown tumor cells; all mice shared the same age. Rag mice were injected both types of cells per cage, to match for age. Mouse weight were checked at the beginning and throughout the study. No obvious weight outliers were present at the start of experiments. In vivo experiments were not blinded as weight measures are not subject to experimentor bias. Flow cytometry analysis was discussed at least between 2 experienced flow cytometry users to ensure an unbiased gating. Gates were also not adjusted on a per sample basis but applied to all samples on an experiment level.
Blinding	We did not utilize blinding in our experimental design as those who were involved in data collection were also involved in experimental design. However, data collection and analysis was not performed manually or in a subjective manner and rigorous statistical analysis was used to prevented any bias in conclusions.

Reporting for specific materials, systems and methods

We require information from authors about some types of materials, experimental systems and methods used in many studies. Here, indicate whether each material, system or method listed is relevant to your study. If you are not sure if a list item applies to your research, read the appropriate section before selecting a response.

Materials & experimental systems

n/a	Involved in the study
☐	☒ Antibodies
☐	☒ Eukaryotic cell lines
☒	☐ Palaeontology and archaeology
☐	☒ Animals and other organisms
☒	☐ Clinical data
☒	☐ Dual use research of concern

Methods

n/a	Involved in the study
☒	☐ ChIP-seq
☐	☒ Flow cytometry
☒	☐ MRI-based neuroimaging

Antibodies

Antibodies used

1. Rabbit anti PSME4 Sigma HPA060922 R85463 1:1000 WB, 1:300 IF
2. Rabbit anti PSME4 Abcam ab5620 GR303025-15 1:50 IP
3. Rabbit anti PSMD11 Abcam ab99414 GR323502-2 1:1000 WB
4. Mouse anti proteasome 20s PSMA1-7 subunits Abcam ab22674 GR3284212-6 1:1000 WB
5. Rabbit anti PSMB10/MECL1 Abcam ab183506 GR153384-15 1:1000 WB
6. Mouse anti β Actin Abcam ab170325 GR3242604-12 1:5000 WB
7. Rabbit anti PA28alpha/PSME1 Cell Signaling 9643 1 1:1000 WB, 1:50 IP
8. Rabbit anti PSMB8/LMP7 Cell Signaling 13635 1 1:1000 WB
9. Rabbit anti PSMB9/LMP2 Abcam ab242061 GR3373421-4 1:1000 WB
10. Rabbit anti PSMB5 Abcam ab3330 GR3373900-1 1: 1000 WB
11. Mouse anti PSMB6 Santa Cruz sc-100455 A3014 1:1000 WB
12. Rabbit anti GAPDH Abcam ab181602 GR3316865 1:5000 WB
13. Rabbit anti Histone H3 LS Bio LS-C353149-100 N/A 1:1000 WB
14. Human HLA-A,B,C-PE Biolegend W6/32 311406 1:20 FC
15. Mouse CD45.2-PerCP/Cy5.5 eBioscience 104 45-0454-82 1:200 FC
16. Mouse CD3e-Super Bright 436 eBioscience 145-2C11 62-0031-82 1:100 FC
17. Mouse CD4-APC/Cy7 Biolegend GK1.5 100414 1:200 FC
18. Mouse CD8a-Super Bright 702 Biolegend 53-6.7 100748 1:200 FC
19. Mouse CD279 (PD-1)-PE eBioscience RPM1-30 12-9981-81 1:100 FC
20. Mouse IFNg-APC eBioscience XMG1.2 17-7311-82 1:160 FC
21. Mouse/human CD44-FITC Biolegend IM7 103005 1:200 FC
22. Mouse CD62L-PE/Cy7 Biolegend MEL-14, 104418 1:6000 FC
23. Mouse FoxP3-Pe eBioscience FJK-16s 12-5773-82 1:200 FC
24. Mouse H-2Db-FITC Biolegend KH95 111505 1:200 FC
25. Mouse H-2kb-PE eBioscience AF6-88.5.5.3 12-5958-82 1:500 FC
26. Mouse anti alpha-6 produced from hybridoma was a kind gift from Keiji Tanaka MAPP, 1:1000 WB
27. IgG1 isotype antibody BioCell BE0083 647018F1 MAPP
28. Goat anti Mouse 488 Invitrogen A11029 VA288487 1:400 IF
29. Goat anti mouse 647 Invitrogen A31571 53313A 1:400 IF
30. Donkey anti Rabbit 647 Abcam ab150075 GR3233351-3 1:400 IF
31. Goat anti mouse HRP Jackson labs 115-035-205 N/A 1:5000 WB
32. Goat anti Rabbit HRP Jackson labs 111-035-003 N/A 1:5000 WB

Validation

Validated for multiple commonly used applications such as IHC (Immunohistochemistry), IF (Immunofluorescence), and WB (Western Blot) by the Human Protein Atlas (HPA) project
2. Validated for WB, ICC/IF as indicated in https://www.abcam.com/products/primary-antibodies/proteasome-activator-subunit-4psme4-antibody-ab5620.html
3. Validated for WB, IP as indicated in https://www.abcam.com/psmd11-antibody-ab99414.html
4. Validated for FC and ICC/IF as indicated in https://www.abcam.com/proteasome-20s-alpha-123567-antibody-mcp231-ab22674.html
5. Validated for WB, IHC-P, FC as indicated in https://www.abcam.com/psmb10mecl1-antibody-epr14902-ab183506.html
6. Validated for WB as indicated in https://www.abcam.com/beta-actin-antibody-8f10-g10-ab170325.html
7. Validated for WB, IP as indicated in https://www.cellsignal.com/products/primary-antibodies/pa28a-d1c10-rabbit-mab/9643
8. Validated for WB as indicated in https://www.cellsignal.com/products/primary-antibodies/psmb8-lmp7-d1k7x-rabbit-mab/13635
9. Validated for WB, IP, FC and ICC/IF as indicated in https://www.abcam.com/products/primary-antibodies/proteasome-20s-lmp2-antibody-epr22042-ab242061.html
10. Validated for WB and ICC/IF as indicated in https://www.abcam.com/products/primary-antibodies/psmb5mb1-antibody-ab3330.html
11. Validated for WB, IP, IF, IHC and ELISA as indicated in https://www.scbt.com/p/psmb6-antibody-jq-3
12. Validated for WB, IP, FC and ICC/IF as indicated in https://www.abcam.com/products/primary-antibodies/gapdh-antibody-epr16891-loading-control-ab181602.html
13. Validated for WB, IHC and ICC/IF as indicated in https://www.lsbio.com/antibodies/histone-h3-antibody-phospho-ser10-icc-if-immunofluorescence-ihc-wb-western-ls-c353149/364270
14. Validated for FC as indicated in https://www.biolegend.com/en-us/products/pe-anti-human-hla-a-b-c-antibody-1872
15. Validated for FC as indicated in https://www.thermofisher.com/antibody/product/CD45-2-Antibody-clone-104-

Monoclonal/45-0454-82
16. Validated for FC as indicated in https://www.thermofisher.com/antibody/product/CD3e-Antibody-clone-145-2C11-Monoclonal/62-0031-82
17. Validated for FC as indicated in https://www.biolegend.com/en-us/products/apc-cy7-anti-mouse-cd4-antibody-1964
18. Validated for FC as indicated in https://www.biolegend.com/de-de/products/brilliant-violet-711-anti-mouse-cd8a-antibody-7926
19. Validated for FC as indicated in https://www.thermofisher.com/antibody/product/CD279-PD-1-Antibody-clone-RMP1-30-Monoclonal/12-9981-81
20. Validated for FC as indicated in https://www.thermofisher.com/antibody/product/IFN-gamma-Antibody-clone-XMG1-2-Monoclonal/17-7311-82
21. Validated for FC as indicated in https://www.biolegend.com/en-us/products/fitc-anti-mouse-human-cd44-antibody-314
22. Validated for FC as indicated in https://www.biolegend.com/en-us/products/pe-cy7-anti-mouse-cd62l-antibody-1922
23. Validated for FC as indicated in https://www.thermofisher.com/antibody/product/FOXP3-Antibody-clone-FJK-16s-Monoclonal/12-5773-82
24. Validated for FC as indicated in https://www.biolegend.com/en-us/products/fitc-anti-mouse-h-2d-b-antibody-325
25. Validated for FC as indicated in https://www.thermofisher.com/antibody/product/MHC-Class-I-H-2Kb-Antibody-clone-AF6-88-5-5-3-Monoclonal/12-5958-82
26. Validated for IP as reported by Stanhill et al. (2006) and Berko et al. (2014)
27. Non-reactive isotype-matched control for mouse IgG1 antibodies in most in vivo and in vitro applications as indicated in https://bioxcell.com/invivomab-mouse-igg1-isotype-control-unknown-specificity-be0083
28. Validated for ICC/IF, IHC and FC as indicated in https://www.thermofisher.com/order/genome-database/dataSheetPdf?producttype=antibody&productsubtype=antibody_secondary&productId=A-11029&version=292
29. Validated for ICC/IF, IHC, ELISA and FC as indicated in https://www.abcam.com/products/secondary-antibodies/donkey-rabbit-igg-hl-alexa-fluor-647-ab150075.html
30. Validated for WB, ELISA and IHC as indicated in https://www.jacksonimmuno.com/catalog/products/115-035-205
31. Validated for WB, ELISA and IHC as indicated in https://www.jacksonimmuno.com/catalog/products/111-035-003

Eukaryotic cell lines

Policy information about cell lines and Sex and Gender in Research

Cell line source(s)	A549 (ATCC CCL-185), KP1.9 (Kind gift of A. Zippelius), H460 (ATCC HTB-177).
Authentication	None of the cell lines used have been authenticated.
Mycoplasma contamination	All cell lines were tested negative for mycoplasma contamination.
Commonly misidentified lines (See ICLAC register)	No commonly misidentified cell lines were used.

Animals and other research organisms

Policy information about studies involving animals; ARRIVE guidelines recommended for reporting animal research, and Sex and Gender in Research

Laboratory animals	Male C57Bl/6 mice (Envigo, Israel) and RAG1 -/- (Jackson Laboratory) at the age of 8-10 weeks.Mice are house in individually ventilated cages, with up to 5 animals per cage, at 12 hours dark/12 hours light cycle, with an average room temperature of 21 C and humidity around 50%.
Wild animals	The study did not involve wild animals
Reporting on sex	only male mice were used in our in vivo studies, as the KP1.9 cells were initially isolated from a male C57BL/6 KrasLSL-G12D/WT;p53Flox/Flox mouse. Female mice rejected engraftment. However, the reprospective analysis on the human clinical cohort contained samples from males and females.
Field-collected samples	The study did not involve field collected samples
Ethics oversight	Animal experiments were conducted according to approved protocols by the Institutional Animal Care and Use Committee (IACUC) of the Weizmann Institute of Science (#04400520-2, #04990620-1). As tumors were in the lung and not subcutaneous, tumor burden was monitored through proxies of weight loss and breathing. Early withdrawal criteria for mice experiments were either weight loss of more than 20% body weight or laborious/heavy breathing due to lung tumor expansion. Mice were removed from the study by reaching either criterion.

Note that full information on the approval of the study protocol must also be provided in the manuscript.

Flow Cytometry

Plots

Confirm that:

☒ The axis labels state the marker and fluorochrome used (e.g. CD4-FITC).

☒ The axis scales are clearly visible. Include numbers along axes only for bottom left plot of group (a 'group' is an analysis of identical markers).

☒ All plots are contour plots with outliers or pseudocolor plots.

☒ A numerical value for number of cells or percentage (with statistics) is provided.

Methodology

Sample preparation	Peripheral blood was washed and red blood cells removed by ACK lysis buffer (150 mM NH4CI, 10 mM KHC03, 0.1 mM EDTA in O.lx PBS-/-) and washed in flow cytometry buffer (PBS-/-, 0.5% BSA, 2mM EDTA). Spleens and lungs were weighted before further processing. The left lung lobe was used for histological analysis of tumor development (hematoxylin and eosin) after fixation in 4% formaldehyde (Biolabs, Israel). Right lung lobes were minced and digested with 5 ml digestion buffer: Collagenase 4 (200U/mL, Worthington Biochemicals), DNase 100) ı ug/mL, Sigma Aldrich) in PBS++ supplemented with 2 mM CaCl2 for 20 minutes at 37"C under shaking. Single cell suspensions of spleen and lungs were obtained by straining cells through 100 um strainers and washed in cold flow cytometry buffer. Red blood cells were removed by ACK lysis buffer, washed with flow cytometry buffer and strained again. scRNA Seq: C57Bl/6J mice were injected with KP1.9 shCtrl or shPSME4 cells (0.25x10^6 cells, i.v.). After 21 days, lungs were perfused manually with 3 mL cold PBS w/o Mg/Ca through the right ventricle of the heart and harvested (4x shCtrl, 4x shPSME4) into cold PBS. The lung tissue was cut into pieces and processed using a GentleMACS Octo Dissociator (program 37C_m_LDK_1, Miltenyi Biotec) with the mouse lung dissociation kit (130-095-927, Miltenyi Biotec) according to the manufacturer's protocol. After the run, cells were strained through a 70 um mesh and washed with FACS buffer (0.5% BSA, 2 mM EDTA in PBS without Mg/Ca). Red blood cells were lysed with ACK buffer for 4 minutes, the reaction stopped by addition of cold FACS buffer. Finally, cells were resuspended in FACS buffer with FC block (anti-CD16/CD32, 1:500, Biolegend 101330) and incubated for 5 minutes. Lung cells from shCtrl or shPSME4 were stained with four differently labeled CD45 antibodies (APC, Pe/C7, FITC, violetFluor 450) for 30 minutes at 4C. Cells were washed with FACS buffer twice, and the shCtrl or shPSME4 samples unified for parallel sorting of the four lung populations. Propidium iodide was added fresh (1 ug/mL) to exclude dead cells, and cells were sorted on BD FACSAria III and BD SORP FACSAria II sorters running on BD FACSDiva software (V8.0.1) using a 85 um nozzle.
Instrument	Attune Nxt with Autosampler , BD FACSAria III and BD SORP FACSAria II sorters
Software	FlowJo (Vl0.7.1, Becton, Dickinson and Company), BD FACSDiva software (V8.0.1)
Cell population abundance	In the scRNA sorting around 40% of the unified sample were Cd45.2 positive and sorted to separate populations. No further post-sort examination was performed.
Gating strategy	Gating strategy: scRNA Seq sort: Cells were gated for single cells by FSC-W vs FSC-H, live as negative for Propidium iodide, and then positive for CD45.2 by one of the 4 colors. A gating strategy is provided in the supplementary materials.

☒ Tick this box to confirm that a figure exemplifying the gating strategy is provided in the Supplementary Information.